DEPARTMENT OF PHYSICS
UNIVERSITY OF JYVÄSKYLÄ
RESEARCH REPORT No. 3/2003

PENNING TRAP FOR ISOBARIC PURIFICATION OF RADIOACTIVE BEAMS AT IGISOL

BY VELI KOLHINEN

Academic Dissertation
For the Degree of
Doctor of Philosophy

To be presented, by permission of the
Faculty of Mathematics and Science
of the University of Jyväskylä,
for public examination in Auditorium FYS-1 of the
University of Jyvväskylä on June 25, 2003
at 12 o'clock noon.

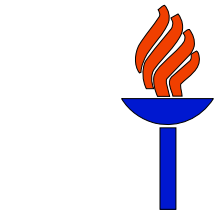

UNIVERSITY OF JYVÄSKYLÄ

Jyväskylä, Finland June, 2003

ISBN 978-951-39-3141-4

URN:ISBN:978-951-39-3141-4

Preface

The work reviewed in this thesis has been carried out at the Department of Physics, University of Jyväskylä during the years 1998-2003. Now at the end of my Ph.D. project the time has come to express my gratitude to the people who have been heavily involved in it.

First of all, I would like to thank my supervisors Professor Juha Äystö for the opportunity to work in such an inspiring and challenging project and his guidance with the help of Dr. Jerzy Szerypo and Dr. Stefan Kopecky. Their help has been essential for the success of my work. I would also like to thank all the members of the IGISOL group especially Mr. Jani Hakala, Mr. Jussi Huikari, Dr. Ari Jokinen, Dr. Arto Nieminen, Mr. Sami Rinta-Antila and Mr. Kari Salomäki without their efforts the Penning trap system would not be operational now.

I would like to thank the staff of the mechanical and electrical workshop of JYFL for providing the necessary help for building the parts for the trap system. Collaboration with the SHIPTRAP group from the GSI Darmstadt has saved a lot of our time in designing and construction.

I would like to express my gratitude also for all the old and present members of the ISOLTRAP collaboration especially Dr. Alban Kellerbauer, Dr. Frank Herfurth, Dr. Markku Oinonen and Mr. Daniel Rodriques. Collaboration with them has been a pleasant and educative experience.

The financial support from the Graduate School of Particle and Nuclear Physics and from the Finnish Science Academy; Vilho, Yrjö and Kalle Väisalä Foundation is gratefully acknowledged.

This work was supported by the Academy of Finland under the Finnish Centre of Excellence Program 2000-2005 (Project No. 44875, Nuclear and Condensed Matter Program at JYFL) and by the EXOTRAPS project in the EU LSF-RTD program under the contract no. ERBFMGECT980099.

I also wish to thank my parents, two brothers and sister for all the encouragement and support.

Jyväskylä, June 2003
Veli Kolhinen

Abstract

A cylindrical Penning trap has been built and tested at the ion guide separator facility IGISOL at the Department of Physics in the University of Jyväskylä. The main goal of the Penning trap application: to purify low-energy radioactive ion beams by mass has been reached. Technical descriptions are presented as well as the results of the first test experiments with stable and radioactive beams. In addition the results of the ^{72}Kr mass measurement at the ISOLTRAP mass spectrometer are given and discussed.

Contents

Chapter 1

Introduction

1.1 General Physics Background

An atom consist of protons, neutrons and electrons. The first two form the core of the atom, a nucleus, while the latter are orbiting around the core as an electron cloud. Nuclei that have a different combinations of N and Z are called isotopes. Here Z is the number of protons and N is the number of neutrons. Nowadays about 2300 different isotopes are known and about 230 of them exist in nature. A nucleus is bound together with the strong interaction due to the nuclear force while the electrons are bound to atom by the electric force. Part of the mass of individual protons and neutrons is transformed to the binding energy of the nucleus according to $\Delta E = \Delta m c^2$ i.e. the mass of the nucleus is smaller than the mass of its individual components; thus the binding energy of a nucleus is defined to be

$$B = (Zm_p + Nm_n - [m(^A X) - Zm_e])c^2. \tag{1.1}$$

Here m_p is the mass of a proton, m_n is the mass of a neutron, m(^{A}X) is the mass of a nucleus and m_e is the mass of an electron.

Since the early days of nuclear physics theorists have been trying to build mass models describing masses of a large variety of isotopes. One of the oldest models is Weizsäcker's mass formula

$$B = a_v A - a_s A^{2/3} - a_c Z(Z-1)A^{-1/3} - a_{sym}\frac{(A-2Z)^2}{A} + \delta, \tag{1.2}$$

where the a_v, a_s, a_c and a_{sym} are constants that have to be adjusted experimentally and δ is a so called pairing force. If N and Z are even $\delta = +a_p A^{-3/4}$,

if N and Z are odd $\delta = -a_p A^{-3/4}$ otherwise δ=0. This binding energy formula has been illustrated in figure 1.1.

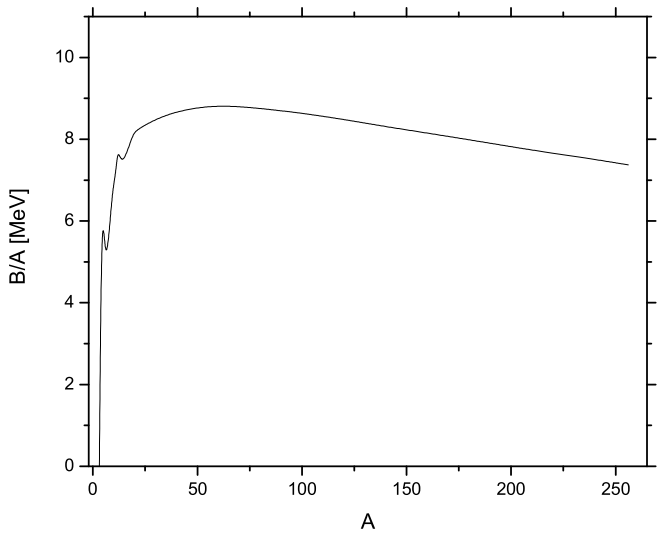

Figure 1.1: Plot of Weizsäcker's formula for binding energy per A in case of some stable isotopes as a function of A. One can easily see that this model has its limitations since for ^{2}H the formula gives a negative value. Values used a_v=15.5, a_s=16.8, a_c=0.72, a_{sym}=23 and a_p=34 in units of MeV/c^2.

However, there are effects in nuclei, like shell effects that have an influence on their mass. So, it requires delicate models to predict masses of real nuclei with relevant precision. On the other hand, this gives a tool to obtain information about nuclear structure by precise mass measurement even if the information about nuclear structure is mostly gained through nuclear reactions and spectroscopy.

Since the early days when research was done mostly close to the valley of beta stability (figure 1.2) one has gone considerably further and now the research tends to go closer and closer to the driplines. Unstable isotopes far from the valley of beta stability are more difficult to produce and it is even more difficult to measure some quantitative properties of these isotopes. This conquest of the unknown territory has given birth to new ways to produce rare isotope beams as well as the new beam manipulation techniques. Very

often methods that are used to produce radioactive ions produce several different isotopes at the same time. Due to this mass selective techniques to clean beams is needed. The ultimate aim is to have isobarically pure beams. This is important since otherwise the unwanted more abundant ions can easily disturb the measurement of rare ions.

1.2 Techniques for Mass Measurements

1.2.1 Decay and Reaction Measurements

In nuclear decay the released energy is used to determine the mass difference between initial and final particles. The Q value (or the energy that is released in a reaction) is $Q = (M_{initial} - M_{final})c^2$ where $M_{initial}$ is the mass of the initial atom and M_{final} is the mass of the final atoms i.e. masses of decay products.

When assuming that the decaying particle is at rest one obtains for the α and proton decay that $Q = T_\alpha(1 + m_\alpha/m_f)$ where T_α is the kinetic energy of α (proton), m_α is the mass of α (proton) and m_f is the mass of the recoil. This method is restricted to nuclei above A$\approx$100. Since the decay spectrum is discrete rather a good mass resolution is achieved ($\sim$ 10 keV i.e. $R = M/\Delta M \approx 10^7$) [Lép01].

For the β decay measurements one can obtain the Q value from the end-point of the continuous β spectra (this spectra is continuous since two particles are being emitted unlike in the α or p decays). The β end-point technique is very sensitive for measurement errors since the electron spectrum has to be measured in coincidence with gamma rays and the Q value has to be deduced from the feeding to the ground state and to the excited states. Limitations in this technique are the production rate, since the coincidence measurement and the end-point measurement needs good statistics as well as the fact that the knowledge of γ-ray energy levels must be adequate. Normally one can reach 100 keV precision (R$\approx 10^6$).

Similarly one can also use nuclear reaction Q values to deduce masses. In a two body reaction A(B,C)D, one can rather easily determine the Q value from the reaction kinematics. These experiments are based on the measurement of scattering angles of recoil and decay particles. This technique is rather precise ($\approx$ 1-20 keV) but it is applicable for the nuclei that are close to stability (Δ Z $\leq$ 1). For heavy ion reactions one can go farther from the

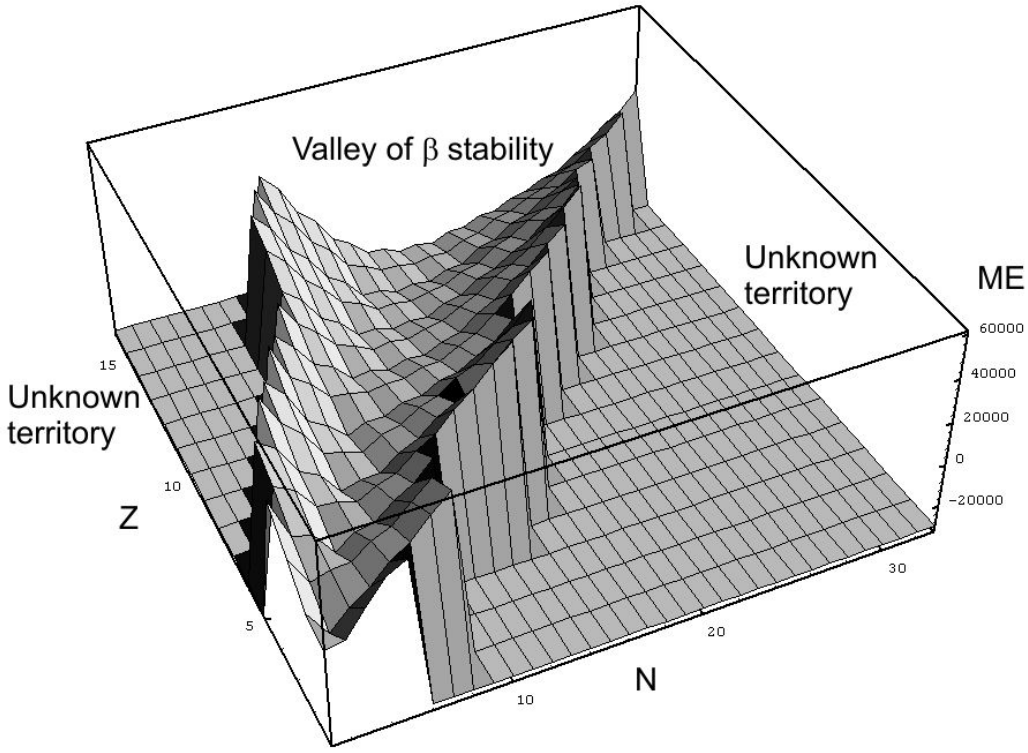

Figure 1.2: A small part of the nuclide chart. Mass excess (ME=m-A) in units of keV as a function of proton number Z and neutron number N. The valley of β stability is at the center of the picture. Flat areas are the unknown territory. Nuclides on the left of the valley decay by β^+ decay or by electron capture and nuclides on the right of the valley decay by β^- decay.

stability (Δ Z $\leq$ 2) with 20-50 keV precision [Lép01].

Also some more exotic reactions like pion double charge reactions have been used for mass measurements of light nuclei like ^{11}B$(\pi^-, \pi^+)^{11}$Li at Los Alamos [Kob92]. This technique has a moderate precision of 100 keV.

1.2.2 Direct Mass Measurements

The simplest direct method for mass measurements is to use a bending magnet to separate masses. Here a uniform magnetic field is used to bend the ion beam into a circular path, see figure 1.3. This kind of system is very fast

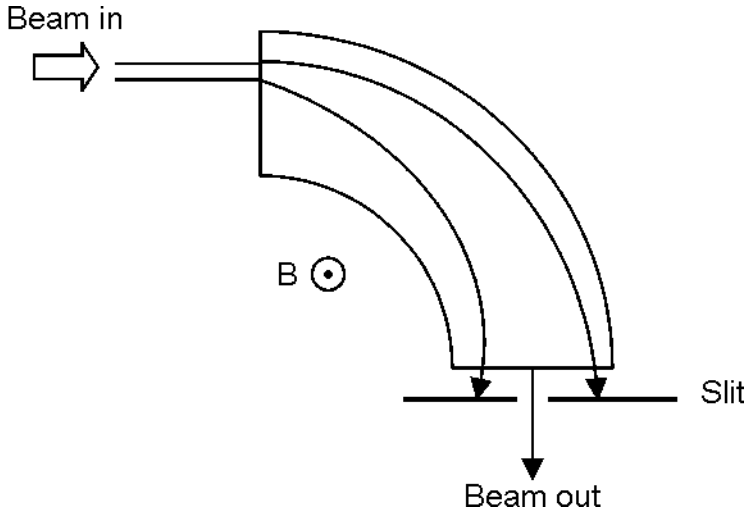

Figure 1.3: The schematic picture of the bending magnet.

and can handle intense beams; on the other hand the mass resolving power $R = M/\Delta M$ is rather modest, usually between 200-10 000. This technique is often combined with nuclear decay Q value measurements.

An improved idea of the bending magnet technique has been applied in the MISTRAL spectrometer [Lun98] at ISOLDE where the beam makes two full turns (diameter about 500 mm) inside a 0.8 T magnet before being ejected through a 0.4 mm wide and 5 mm high slit. At the end of the 1st and 3rd half-turns, ions pass through a 5 mm wide slit and an RF-modulation cavity where the kinetic energy of the ions change, i.e. the spread of the beam is increased so much that the ions cannot anymore pass through the exit slit. Since the cyclotron frequency $\omega_c = qB/m$ does not depend on the

velocity of an ion it is possible to tune the RF cavities in such a way that the second cavity cancels the effect of the first cavity. By measuring transmission count rate as a function of the frequency one can determine the ion masses. This method is very fast, the flight time through the device is 50 μs, and mass resolving power of 1×10^5 can be reached with it.

Time-of-flight method on a linear path has been used in mass measurements at GANIL where they have combined the TOF technique with the SPEG-spectrometer [H.Sav01]. The flight time along the 82 meter long path is of the order of 1 μs and for nuclei A$\approx$40 uncertainties from 100 keV (nuclei close to stability) to 1 MeV (exotic nuclei) has been reached with it. This corresponds resolving power of R=4×10^5-4×10^4.

The TOF technique can be used also in a cyclotron such as at GANIL [Aug94] where two identical isochronous cyclotrons are used. The first cyclotron accelerates the primary beam that hits the target and the secondary radioactive beam is re-accelerated in the second cyclotron. In case of the ions that have a same charge state but a slightly different mass $m + \Delta m$ the heavier ions will lag behind during the acceleration and the subsequent time difference is related to the mass difference in the following way

$$\frac{\Delta t}{t} = \frac{\Delta m}{m} \tag{1.3}$$

if Δm is small. The resolving power of R=2.5×10^5 has been reached with this technique and the transit time through the re-acceleration is 40-70 μs.

One way to carry out mass measurements is to use a storage ring such as the ESR in GSI Darmstadt [Fra87]. These mass measurements are based on the fact that the revolution frequency $f_{rev} = f/L$ and the mass of an ion are related by

$$\frac{\Delta f_{rev}}{f_{rev}} = -\gamma_t^{-2}\frac{\Delta(m/q)}{m/q} + (1 - \frac{\gamma^2}{\gamma_t^2})\frac{\Delta v}{v}, \tag{1.4}$$

where γ is the Lorenz factor and γ_t is a factor that depends on the ion optics. One can see that if the last term of the equation (1.4) is neglible the revolution frequency can be used in precise mass measurements. This can be done in two different ways either by decreasing the velocity distribution like it is done in Schottky mass spectrometry [Lit01] or to operate the ring in an isochronous mode [Hau00] in a condition where $\gamma_t = \gamma$. The former needs several seconds to decrease the velocity distribution and the resolving power of $R = 7 \times 10^5$ has been reached with it. The latter method is very

fast, within 50 μs time one can reach $R = 1.5 \times 10^5$. These are powerful methods to do mass measurements since they can be applied simultaneously to several isotopes.

A Penning trap [Deh67], [Deh69] provides an excellent tool to make mass measurements, especially when using time-of-flight method for mass determination [Gra80] such as at SMILETRAP at Stockholm [Car97], where the maximum mass resolving power reached is R=3×10^9 [Fri02]. However, this kind of resolving power is possible to achieve only for highly charged ions with long trapping times, which are not applicable for exotic radioactive nuclei. Thus for short lived ions one has to use short trapping times and singly charged ions as it is done in ISOLTRAP at CERN [Bol96] where resolving powers of 10^7-10^8 are reached within seconds.

1.2.3 Comparison

A short comparison between different mass measurement techniques is shown in table 1.1.

Technique	Typical R	$T_{1/2}$
α decay	1×10^7	1 μs
β decay	1×10^6	100 ms
Nuclear reaction	5×10^6	1 μs
Mass spectrometer	$200 - 1 \times 10^4$	1 μs
Linear TOF	$4 \times 10^4 - 4 \times 10^5$	1 μs
Cyclotron TOF	2×10^5	50 μs
MISTRAL	1×10^5	50 μs
Storage ring	1.5×10^5 or 7.5×10^5	50 μs or 10 s
Penning trap	$10^7 - 10^8$	100 ms

Table 1.1: A comparison between different mass measurement techniques, the technique, a typical resolving power, a typical half-life $T_{1/2}$ that can be measured with it.

It is obvious that a Penning trap is the superior technique in mass measurements when it comes to the resolving power. That explains why so many groups around the world are interested in this technique. However, one should not forget that Penning traps are also suitable devices to produce isobarically pure beams for further spectroscopy measurement as is done in

REXTRAP where the beam after being ejected from the purification Penning trap is injected into a charge breeder and further into a post acceleration system [Hab00].

In general one can say that ion traps will be used heavily in the future to create new physics. There are several trap projects where the construction is presently going on [Bol02]. They are SHIPTRAP at GSI, WITCH at ISOLDE, LPC Caen, RIKEN, KVI Groningen, ISAC/TRIUMF, MAFF at Garching and LEBIT at NSCL/MSU.

1.3 JYFLTRAP at IGISOL

The JYFLTRAP project was launched in 1997 [Jok97, Nie98] to enhance the quality of the radioactive beams produced at IGISOL [Äys01]. The aim was to reduce the energy spread below 1 eV and emittance below 1π mm mrad and increase the mass resolving power up to R=2×10^4-10^5. To reach this goal an RFQ cooler/buncher and a double Penning trap of a cylindrical type [Rai97] has been built.

The RFQ cooler/buncher cools and bunches the beam for the injection to the first Penning trap. (Note that term "cooling" in this thesis work means always the reduction of the 6 dimensional phase space volume $\Delta x \Delta y \Delta z \Delta p_x \Delta p_y \Delta p_z$ i.e. reduction of the emittances [Moo95].)

The first goal of the Penning trap is to purify the bunched beam coming from the RFQ. Later we also aim to perform accurate mass measurements. To achieve this a mass-selective buffer gas cooling [Ita95], [G.Sav91] is used. It has been demonstrated that this device is capable of making isobaric mass purification and to reach a resolving power R=2×10^4-10^5 in 100-500 ms.

Ions of exotic isotopes for JYFLTRAP are produced by the on-line isotope separator IGISOL developed at Jyväskyla during early '80s [Ärj81], [Ärj85]. In this technique a primary beam from the K=130 MeV cyclotron hits a thin target and reaction products recoiling out of the target are stopped in a gas cell where they are thermalized in He gas remaining mostly in a charge state of +1 [Ärj86].

Thermalized ions are guided by a helium jet out of the gas cell and gas is directed through a skimmer hole to the differential pumping section where ions are accelerated to 38 keV energy. This process is chemically non selective and furthermore very fast. Technical advantage of this system is its durability and simplicity. However, due to a large energy spread of the beam (several

10 keV), the mass resolving power remains rather modest ($M/\delta M \leq 300$). These qualities also couple with the intensity of the beam in such a way that the increasing intensity leads to a worsened beam quality.

The ions from IGISOL are injected into a buffer-gas filled radio-frequency quadrupole trap (RFQ). This RFQ cooler/buncher [Nie01], a 2 dimensional Paul trap [Pau53], [Daw76] is behind the separator focal plane (see figure 1.4) and it is situated on the left beam line. The RFQ device is placed on the HV platform which allows to slow down the 38 keV ion beam from IGISOL to about 100 eV suitable for injection into the cooler. The purpose of this device is to decrease the energy spread and emittance of the original IGISOL beam. The RFQ consists of four cylindrical segmented rods with a length of 40 cm and a diameter of 23 mm. The vacuum between the rods is filled with He gas at pressure of around 1×10^{-1} mbar which is enough to stop ions inside the quadrupole. Collisions with the buffer gas atoms reduce the transverse and axial energy, meanwhile the oscillating RF field keeps the ions on the optical axis. These ions are guided through the RFQ rods by a weak axial electric field to the trapping region where the ions are stored until the bunch is released and re-accelerated (figure 1.5).

The bunch length is measured to be 10-20 μs long and the overall transmission efficiency is 60 %. The other significant quantities that describe the cooler performance are shown in table 1.2. Small energy spread, emittance and short pulse length are necessary conditions to be able to inject a beam into a Penning trap system.

	Before	After
Energy spread	50-150 eV	1 eV
Emittance	10π-15π mm mrad	3π mm mrad

Table 1.2: Cooler performance [Nie01], [Nie02b].

The main goal of the Penning trap application is to purify the radioactive beam by mass. The high mass resolving power of the order of R=2×10^4-10^5 permits to reject even the isobaric contaminants. This is particularly important for the experimental program at IGISOL, which is centered on exotic neutron-rich nuclei, produced in fission. The isobaric purification will allow for rejecting all unwanted members of the isobaric chain, leaving only species of interest left. This will significantly improve the signal-to-background ra-

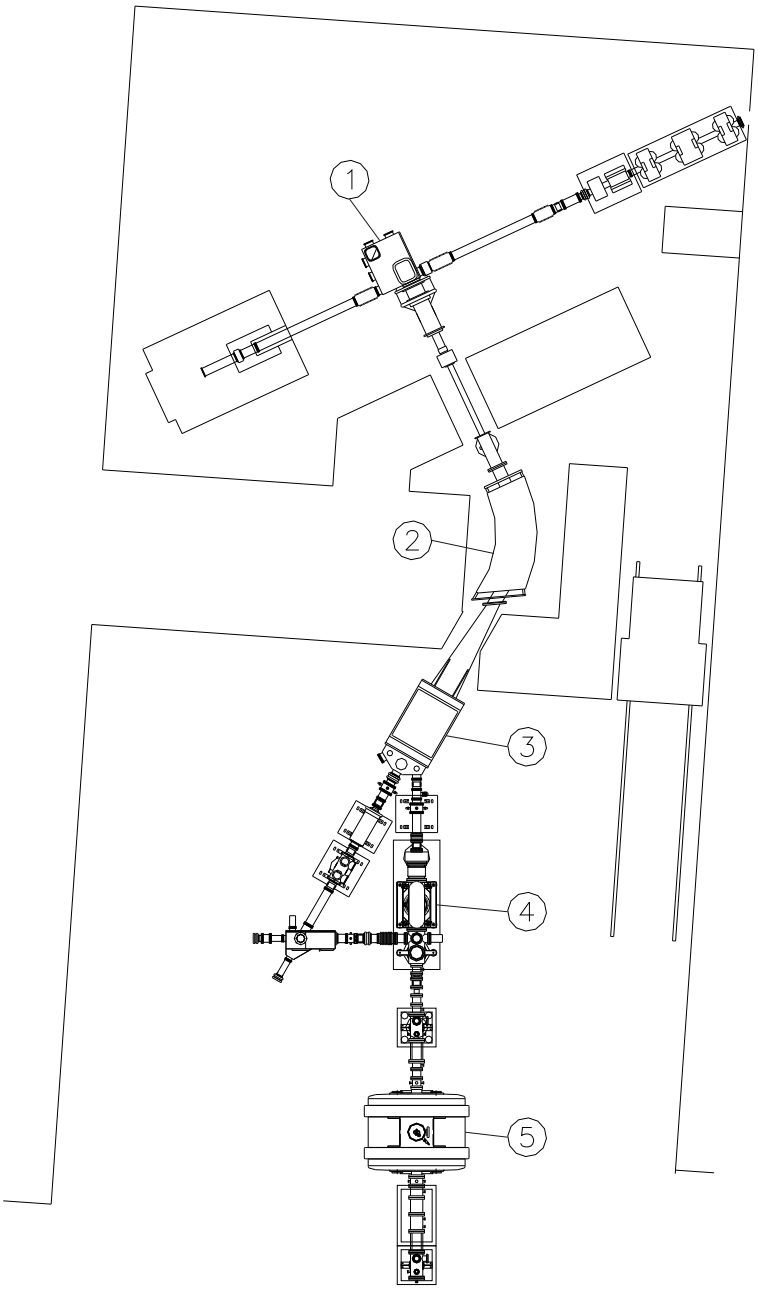

Figure 1.4: Layout of the IGISOL area. 1. Target and ionguide, 2. Bending magnet, 3. Switchyard, 4. RFQ cooler/buncher, 5. Penning trap.

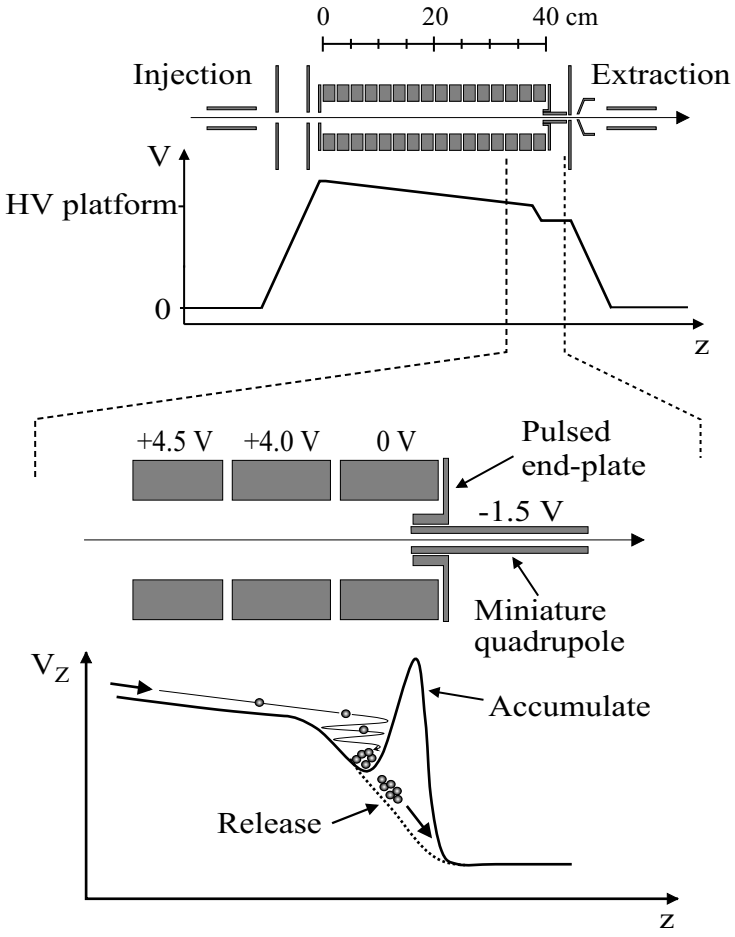

Figure 1.5: Principle of the the RFQ cooler/buncher [Nie02].

tio, sensitivity and the precision of the experiments, and will extend the the range of isotopes investigated.

Within this thesis a Penning trap system has been implemented at IGISOL at the University of Jyväskylä and the first Penning trap, the purification trap, has been commissioned to perform isobaric mass purification of radioactive beams. The report starts by a chapter that introduces the theory of operation of a Penning trap and goes on with a technical description of the Penning trap at JYFL. Experimental results with stable and radioactive beams are given. The results from the ^{72}Kr run at ISOLTRTAP/CERN are shown. New developments for the Penning trap system at JYFL are discussed.

The author of this thesis has been the main contributor to the ion optical design, construction, testing and operation of the JYFLTRAP Penning trap system. The author has also performed the data analysis for ^{72}Kr results with Mr. Daniel Rodriques.

Chapter 2

Theory of Operation

2.1 Introduction to Trapping and Purification

This section introduces briefly the idea of operation of the purification Penning trap before going to the more detailed theoretical description of Penning traps. There are five steps in the isobaric mass purification with a buffer-gas filled Penning trap: trapping an ion bunch, axial cooling, magnetron excitation, cyclotron excitation and ejection of the ion bunch.

The first step is to trap an ion bunch delivered by the RFQ cooler/buncher in the Penning trap. This is achieved by appropriately switching the electric potential of the Penning trap.

A waiting time is applied during which the ions cooled to the potential minimum of the trap by collisions with the buffer-gas. This is important in order to allow the ions to see the radio-frequency fields which are only applied in the center of the trap where the electric and magnetic field imperfections are minimized.

The next step is to drive all ions to a radius larger than the exit hole of the trap. This can be achieved with an excitation of the ion motion at the so-called magnetron frequency which does not depend on the mass of the ions.

After all ions have been moved to large orbits, the desired species are re-centered by another radio-frequency excitation at the cyclotron fre-

quency of the ion.

In the last step the ions are ejected. In this process all ions with radii larger than the exit hole of the trap will lost on the trap walls and only the desired species leaves the trap for further use.

The following chapters 2.2 through 2.7 provide a more detailed description of the theory of a Penning trap. This formulation provides the understanding of the basic motions and excitations in Penning traps. Later on (chapter 3.10) a more detailed technical description of the purification trap of the JYFLTRAP device is given.

2.2 Principle of a Penning trap

A Penning trap is an electromagnetic trap where ions are confined in three dimensions by the superposition of a static quadrupole potential and homogenous magnetic field [Deh67], [Deh69].

In the radial direction the ions are confined by the axial magnetic field

$$\vec{B} = B\hat{e}_z. \tag{2.1}$$

Since a strong magnetic field is required for the mass separation, it is created by means of a superconducting magnet. A confinement in the third, magnetic field direction (parallel to the trap axis, z-axis in this thesis) is done by a static quadrupole electric field. This potential has the form

$$\phi(z,r) = \frac{U_0}{4d^2}(2z^2 - \rho^2). \tag{2.2}$$

Where the parameter d

$$d = \sqrt{\frac{1}{2}(z_0^2 - \frac{\rho_0^2}{2})} \tag{2.3}$$

is called a characteristic trap parameter. This quadrupole electric field can be produced in two different ways. A Penning trap can be made of three hyperboloidal electrodes described by:

$$z^2 = z_0^2 + \frac{1}{2}\rho^2 \tag{2.4}$$

$$z^2 = \frac{1}{2}(\rho^2 - \rho_0^2) \tag{2.5}$$

that describe the endcaps and the ring electrode between them. Normally extra electrodes, correction electrodes, are still needed to make fine adjustment to the electrical potential. Another way to create a quadrupole electric field is to use a set of cylindrical (ring) electrodes (three or more), see figure 2.1. The number and the length of the electrodes depend in particular on the size of the region in which one wants to minimize higher order multipole contributions. For example, dimensions and voltages that have been used in the purification Penning trap at ISOLTRAP are shown in table 2.1 [Rai97]. Dimensions used in the Penning traps at JYFL are scaled from these values. In this case the characteristic trap parameter has no specific meaning and

Electrode	U_i/U_0	l_i/ρ_0
Endcap	0.00	4.00
Correction 2	0.34	0.45
Correction 1	0.83	0.83
Ring	1.00	1.19
Correction 1	0.83	0.83
Correction 2	0.34	0.45
Endcap	0.00	4.00

Table 2.1: Voltage ratios and the length-to-inner radius ratios l_i/ρ_0 for a cylindrical trap used at ISOLTRAP where ρ_0=20 mm .

the ratio U_0/d describes only the depth of the potential well. This well is created in such a way that the central electrode is set to a negative potential whereas the outer electrodes are at positive potentials. In this way an axial potential well for the ions with a minimum at the trap center is formed for positively charged species. This electrode structure gives the name for a cylindrical Penning trap.

2.3 Equation of Motion

Motion of a particle that has a mass m and a charge q in combined electric and magnetic fields is described by the Lorenz force

$$m\ddot{\vec{r}} = q(\dot{\vec{r}} \times \vec{B} + \vec{\nabla}\phi). \tag{2.6}$$

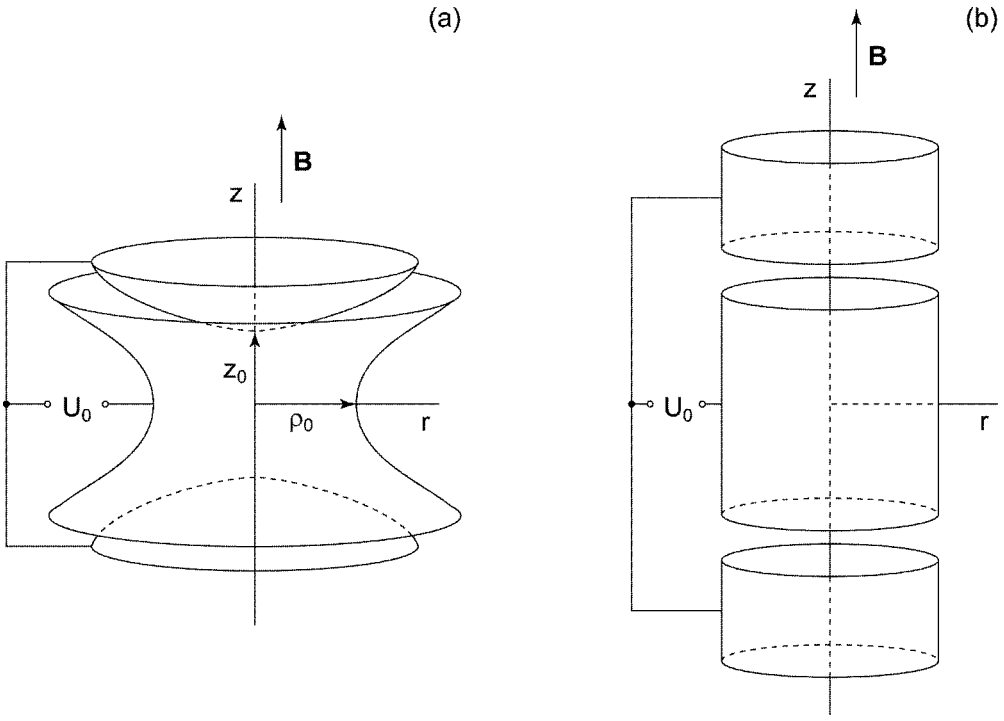

Figure 2.1: Two different types of electrode configurations for Penning traps: (a) hyperbolic trap, (b) cylindrical trap. Correction electrodes are neglected in this picture for the simplicity.

Using the definition (2.1) and

$$\omega_z = \sqrt{\frac{qU_0}{md^2}} \tag{2.7}$$

and

$$\omega_c = \frac{q}{m}B \tag{2.8}$$

and since the electric potential has a quadrupole shape

$$\vec{E} = -\vec{\nabla}\phi = \frac{U_0}{2d^2}\begin{pmatrix} x \\ y \\ -2z \end{pmatrix} \tag{2.9}$$

the equation of motion (2.6) can be written as

$$\begin{pmatrix} \ddot{x} \\ \ddot{y} \\ \ddot{z} \end{pmatrix} - \omega_c \begin{pmatrix} \dot{y} \\ -\dot{x} \\ 0 \end{pmatrix} - \frac{\omega_z^2}{2} \begin{pmatrix} x \\ y \\ -2z \end{pmatrix} = 0. \tag{2.10}$$

Here one can see that the radial motion is coupled and the axial motion $\ddot{z} + \omega_z^2 z = 0$ is only a harmonic oscillation with a frequency ω_z i.e.

$$z = A_z \sin(\omega_z t + \phi_z) \tag{2.11}$$

where the amplitude and the phase depend on the initial conditions. Now the radial part of the equation (2.10) can be written in the following way by multiplying y-direction equation by complex i and using transformation $u = x + iy$

$$\ddot{u} + i\omega_c \dot{u} - \frac{\omega_c^2}{2} u = 0. \tag{2.12}$$

This homogenous differential equation is solved by using the ansatz $u = e^{-i\omega t}$. The solution for equation (2.12) is

$$u = Ae^{-i\omega_+ t} + Be^{-i\omega_- t} \tag{2.13}$$

with

$$\omega_\pm = \frac{1}{2}(\omega_c \pm \sqrt{\omega_c^2 - 2\omega_z^2}). \tag{2.14}$$

This can be written again in normal rectangular Cartesian coordinates as

$$\begin{pmatrix} x \\ y \end{pmatrix} = \rho^- \begin{pmatrix} \cos(\omega_- t + \phi_-) \\ -\sin(\omega_- t + \phi_-) \end{pmatrix} + \rho^+ \begin{pmatrix} \cos(\omega_+ t + \phi_+) \\ -\sin(\omega_+ t + \phi_+) \end{pmatrix}. \tag{2.15}$$

Thus the radial motion is a superposition of two coupled circular motions. They are called reduced cyclotron motion and magnetron motion and denoted ω_+ and ω_-, respectively. Motions are shown in figure 2.2. The following frequency relations are valid:

$$\begin{gathered} \omega_+ + \omega_- = \omega_c \\ \omega_+^2 + \omega_-^2 + \omega_z^2 = \omega_c^2 \\ 2\omega_+\omega_- = \omega_z^2 \\ \omega - < \omega_z < \omega_+ < \omega_c. \end{gathered} \tag{2.16}$$

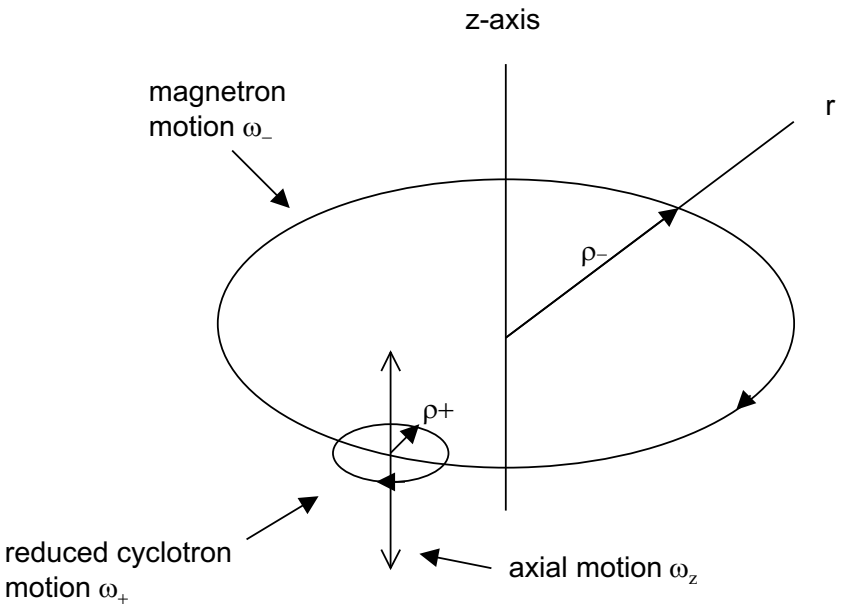

Figure 2.2: Motion of a positively charged particle in a Penning trap. The motion in z-direction is a harmonic oscillation with a frequency ω_z and in the radial direction motion is a superposition of two circular radial motions, the magnetron motion with a frequency ω_- and the reduced cyclotron motion with a frequency ω_+.

2.4 Frictional Damping – Buffer Gas Cooling

In a buffer gas cooling ion motion is damped by the collisions with the buffer gas molecules. For ions that move at low velocities the average damping force is [McD73] proportional to the velocity of an ion

$$\vec{F}_{damping} = -\sigma m \dot{\vec{r}} \tag{2.17}$$

and the equation of motion becomes

$$\begin{pmatrix} \ddot{x} \\ \ddot{y} \\ \ddot{z} \end{pmatrix} - \begin{pmatrix} \omega_c \dot{y} - \sigma \dot{x} \\ -\omega_c \dot{x} - \sigma \dot{y} \\ -\sigma \dot{z} \end{pmatrix} - \frac{\omega_z^2}{2} \begin{pmatrix} x \\ y \\ -2z \end{pmatrix} = 0. \tag{2.18}$$

In the axial case the solution is

$$z(t) = A'_z e^{-\frac{\sigma}{2}t} \sin(\omega'_z t + \phi'_z) \tag{2.19}$$

with

$$\omega'_z = \sqrt{\omega_z^2 - \frac{1}{4}\sigma^2}. \tag{2.20}$$

And the radial part has a solution:

$$\begin{pmatrix} x \\ y \end{pmatrix} = \rho^- e^{\alpha_- t} \begin{pmatrix} \cos(\omega'_- t + \phi_-) \\ -\sin(\omega'_- t + \phi_-) \end{pmatrix} + \rho^+ e^{\alpha_+ t} \begin{pmatrix} \cos(\omega'_+ t + \phi_+) \\ -\sin(\omega'_+ t + \phi_+) \end{pmatrix} \tag{2.21}$$

with

$$\omega'_\pm = \omega_\pm \pm \Delta\omega, \ \Delta\omega = \frac{\sigma^2}{16} \frac{8\omega_z^2 + \sigma^2}{(\omega_c^2 - 2\omega_z^2)^{\frac{3}{2}}} \tag{2.22}$$

and

$$\alpha_\pm = -\frac{\sigma}{2} \left(1 \pm \left[1 + \frac{1}{8} \frac{8\omega_z^2 + \sigma^2}{\omega_c^2 - 2\omega_z^2} \right] \right). \tag{2.23}$$

Therefore the radial motion is still a superposition of two circular motions with frequencies ω'_+ and ω'_-. However, these frequencies are shifted by $\Delta\omega$ compared to the undamped case. However, in the regime of real working parameters for the trap this shift is neglibly small. It is good to notice that $\omega_+ + \omega_- = \omega_c$ is still valid. From the equation (2.23) one can see that the radius of the reduced cyclotron motion decays exponentially with $\alpha_+ \approx -\sigma$ and the radius of the magnetron motion increases with a smaller time constant $\alpha_- \approx \frac{\sigma}{2}\frac{\omega_z^2}{\omega_c^2}$. Due to continuous increase of the magnetron radius a particle will be eventually lost.

2.5 Cooling and Excitation

In order to be able to manipulate ion motion in gas in a Penning trap and remove the unwanted isobars azimuthal dipole and quadrupole radio-frequency fields are used. These fields are created by using a segmented central electrode, see figure 2.3.

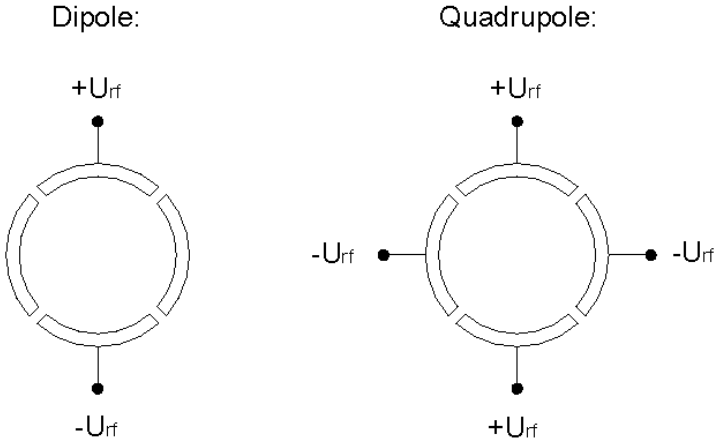

Figure 2.3: Generation of the oscillating azimuthal electric dipole field (left) and the quadrupole field (right) in Penning trap using four split segmented ring electrode.

These excited motions are solved by introducing new parameters [Bro86]

$$\dot{\vec{V}}^{\pm} = \dot{\vec{\rho}} - \omega_{\mp}\vec{\rho} \times \hat{e}_z, \tag{2.24}$$

where $\vec{V}^{+}$ and $\vec{V}^{-}$ are the velocities in the coordinate systems that are moving with the velocities $\omega_{-}\vec{\rho} \times \vec{e}_z$ and $\omega_{+}\vec{\rho} \times \vec{e}_z$. Now using this new notation the radial part of the equation (2.10) can be written

$$\dot{\vec{V}}^{\pm} = \omega_{\pm}\vec{V}^{\pm} \times \hat{e}_z \;\Leftrightarrow\; \begin{pmatrix} \dot{V}_x^{\pm} \\ \dot{V}_y^{\pm} \end{pmatrix} = \begin{pmatrix} \omega_{\pm}V_y^{\pm} \\ -\omega_{\pm}V_x^{\pm} \end{pmatrix}. \tag{2.25}$$

Inverse transformation into Cartesian coordinates is done via

$$x = -\frac{V_y^{+} - V_y^{-}}{\omega_{+} - \omega_{-}} \text{ and } y = \frac{V_x^{+} - V_x^{-}}{\omega_{+} - \omega_{-}}. \tag{2.26}$$

Since the axial movement is not affected by the radio-frequency excitation, it is not discussed at all in dipole or quadrupole excitations.

2.5.1 Dipole Excitation

A dipole field is created when the oscillating voltage is connected to the opposite half electrodes in such a way that voltages are 180° phase shifted compared to each other. Now the equation of motion that includes damping and the dipole field will be

$$\begin{array}{l} \dot{V}_x^{\pm} = \omega_{\pm} V_y^{\pm} - \gamma(\omega_+ V_x^+ - \omega_- V_x^-) \\ \dot{V}_y^{\pm} = -\omega_{\pm} V_x^{\pm} - \gamma(\omega_+ V_y^+ - \omega_- V_y^-) + k_0 \cos(\omega_{rf} t + \phi_{rf}) \end{array} \tag{2.27}$$

with

$$k_0 = a\frac{qU}{m\rho_0} \text{ and } \gamma = \frac{\sigma}{\omega_+ - \omega_-}. \tag{2.28}$$

The parameter a is a geometry factor that describes deviations from the ideal electrical potential and the U is the maximum value of U_{rf} at radius ρ_0. These equations can be solved by setting $\vec{V}^{\pm}(t) = \vec{A}^{\pm}(t)e^{\pm i(\omega_{\pm} t + \phi_{\pm})}$. Expressing the cosine in exponential functions and neglecting the high-frequency terms [Bol90], i.e. $e^{\pm i(\omega_+ + \omega_-)}$, $e^{i(\omega_{rf} + \omega_{\pm})}$ and in the case of an excitation also all terms with $(\omega_+ - \omega_-)$, and using the assumption of circular motion [Kön95] $A_y^{\pm} = \pm i A_x^{\pm} = \pm i A^{\pm}$ one obtains

$$\omega_{rf} \approx \omega_+ : \quad \begin{cases} \dot{A}^+ = & -\gamma\omega_+ A^+ - \frac{ik_0}{2} e^{-i[(\omega_{rf} - \omega_+)t + \phi_{rf} - \phi_+]} \\ \dot{A}^- = & \gamma\omega_- A^- \end{cases} \tag{2.29}$$

$$\omega_{rf} \approx \omega_- : \quad \begin{cases} \dot{A}^+ = & -\gamma\omega_+ A^+ \\ \dot{A}^- = & \gamma\omega_- A^- + \frac{ik_0}{2} e^{-i[(\omega_{rf} - \omega_-)t + \phi_{rf} - \phi_-]}. \end{cases} \tag{2.30}$$

Terms that contain the exponential function describe the excitation, the two other equations describe the behaviour of magnetron and reduced cyclotron motions without excitation, i.e. normal growth and decrease of the radius. Now concentrating on the excitation we can combine the previous result to

$$\dot{A}^{\pm} - \alpha_{\pm} A^{\pm} = \frac{ik^{\pm}}{2} e^{i\Delta\omega_{\pm} t} \tag{2.31}$$

with

$$\begin{aligned} \alpha_{\pm} &= \mp\gamma\omega_{\pm} \\ k^{\pm} &= \mp k_0 e^{\pm(\phi_{rf}-\phi_{\pm})} \\ \Delta\omega_{\pm} &= \pm(\omega_{rf}-\omega_{\pm}). \end{aligned} \tag{2.32}$$

This differential equation can be solved by using Laplace's transformation $L(p) = \int_0^{\infty} A(t)e^{-pt}dt$. One obtains

$$L^{\pm}(p) = \frac{A^{\pm}(0)}{p-\alpha_{\pm}} + \frac{ik^{\pm}}{2}\frac{1}{\alpha_{\pm}-i\Delta\omega_{\pm}}\left[\frac{1}{\alpha_{\pm}-p} + \frac{1}{p-i\Delta\omega_{\pm}}\right]. \tag{2.33}$$

Inverse transformation can be done by using calculus of residues. The solution is

$$A^{\pm}(t) = A^{\pm}(0)e^{\alpha_{\pm}t} + \frac{ik^{\pm}}{2}\left(\frac{e^{i\Delta\omega_{\pm}t}-e^{\alpha_{\pm}t}}{\alpha_{\pm}-i\Delta\omega_{\pm}}\right). \tag{2.34}$$

One can see that in the simplest case when $\alpha_{\pm} \neq 0$ and $k_0 = 0$, the equation (2.34) becomes

$$\rho^{\pm} = \rho^{\pm}(0)e^{\alpha_{\pm}t} \tag{2.35}$$

where $\rho = A/(\omega_+ - \omega_-)$. This describes how the radius of the magnetron motion increases and the reduced cyclotron motion decreases.

In case $\alpha_{\pm} = 0$ and $k_0 \neq 0$ one gets from equation (2.34) that

$$\begin{aligned} \rho^{\pm} = \frac{1}{\omega_+-\omega_-}\Bigg[&A^{\pm}(0)^2 + \frac{k_0^2}{\Delta\omega_{\pm}^2}\sin^4(\frac{\Delta\omega_{\pm}}{2}t) + \frac{1}{4}\frac{k_0^2}{\Delta\omega_{\pm}^2}\sin^2(\Delta\omega_{\pm}t) \\ &+ A^{\pm}(0)\frac{k_0}{\Delta\omega_{\pm}}\left(\mp 2\cos(\Delta\phi_{\pm})\sin^2(\frac{\Delta\omega_{\pm}}{2}t) - \sin(\Delta\phi_{\pm})\sin(\Delta\omega_{\pm}t)\right)\Bigg]^{\frac{1}{2}} \end{aligned} \tag{2.36}$$

where $\Delta\phi = \phi_{rf} - \phi_{\pm}$. From equation (2.36) one can see that the motion is just oscillation.

A third case, where $\alpha_{\pm} \neq 0$ and $k_0 \neq 0$, when assuming that $\Delta\phi_{\pm} = 0$ will result in

$$\rho^{\pm}(t) = \frac{1}{\omega_+-\omega_-}\left[\left(A^{\pm}(0)e^{\alpha_{\pm}t} + \frac{k_0}{2}\frac{\mu}{\lambda}\right)^2 + \left(\frac{k_0}{2}\frac{\nu}{\lambda}\right)^2\right]^{\frac{1}{2}} \tag{2.37}$$

with

$$\begin{aligned}\mu &= \pm\,\alpha_\pm \sin(\Delta\omega_\pm) \mp \Delta\omega_\pm \left[e^{\alpha_\pm t} - \cos(\Delta\omega_\pm t)\right] \\ \mu &= \pm\,\Delta\omega_\pm \sin(\Delta\omega_\pm) \pm \alpha_\pm \left[e^{\alpha_\pm t} - \cos(\Delta\omega_\pm t)\right] \\ \lambda &= \Delta\omega_\pm^2 + \alpha_\pm^2.\end{aligned} \tag{2.38}$$

When $t \to \infty$ one obtains from the equation (2.37) that the magnetron radius increases without limit (figure 2.4) and the reduced cyclotron radius approaches its maximium value (figure 2.5).

$$\rho^+(t \to \infty) = \frac{1}{2}\frac{k_0}{\sqrt{\Delta\omega_\pm^2 - \alpha_\pm^2}}\frac{1}{\omega_+ - \omega_-}. \tag{2.39}$$

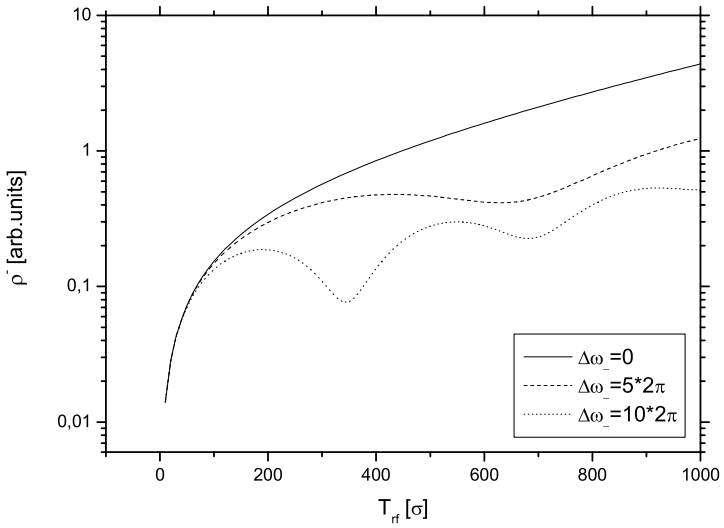

Figure 2.4: Radius of a magnetron motion ρ^- for ω_- dipole excitation as a function of excitation time in units of σ. Different lines in the figure correspond to different excitation frequency, i.e. detuning of ω_{rf}. Solid line: ω_{rf}=ω_-, dashed line: ω_{rf}=ω_-+5*2π and dotted line: ω_{rf}=ω_-+10*2π. Numbers used in figure: $\omega_c = 867266 \times 2\pi$ Hz, $\omega_+ = 865551 \times 2\pi$ Hz and $\omega_- = 1715 \times 2\pi$ Hz. These are the real frequencies for the $^{124}Xe^+$ ion in 7 Tesla magnetic field of JYFLTRAP. Other parameters $\rho^-(0)$=0 and $k_0 = \gamma\omega_c$.

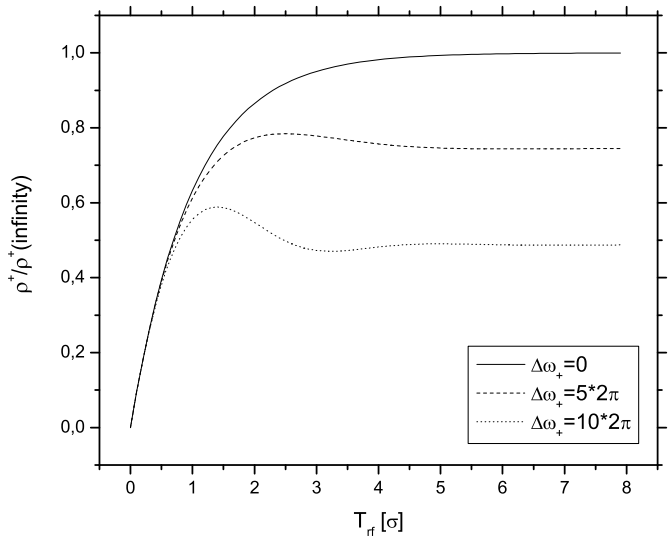

Figure 2.5: Radius of a reduced cyclotron motion ρ^+ for ω_+ dipole excitation as a function of excitation time in units of σ. Different lines in the figure correspond to different excitation frequency, i.e. detuning of ω_{rf}. Solid line: ω_{rf}=ω_+, dashed line: ω_{rf}=ω_++5*2π and dotted line: ω_{rf}=ω_++10*2π. Numbers used in figure: $\omega_c = 867266 \times 2\pi$ Hz, $\omega_+ = 865551 \times 2\pi$ Hz and $\omega_- = 1715 \times 2\pi$ Hz. These are the real frequencies for the $^{124}Xe^+$ ions in 7 Tesla magnetic field of JYFLTRAP. Other parameters $\rho^-(0)$=0 and $k_0 = \gamma\omega_c$.

2.5.2 Quadrupole Excitation

Now the equation of motion that includes damping and the quadrupole field will be

$$\begin{aligned} \dot{V}_x^{\pm} &= \omega_{\pm} V_y^{\pm} - \gamma(\omega_+ V_x^+ - \omega_- V_x^-) + k(V_x^+ - V_x^-) \\ \dot{V}_y^{\pm} &= -\omega_{\pm} V_x^{\pm} - \gamma(\omega_+ V_y^+ - \omega_- V_y^-) + k(V_y^- - V_y^+) \end{aligned} \tag{2.40}$$

with

$$k = k_0 \cos(\omega_{rf} t + \phi_{rf}) \text{ and } k_0 = \frac{U}{2\rho_0^2} \frac{q}{m} \frac{a}{\omega_+ - \omega_-}. \tag{2.41}$$

The equation 2.40 will be solved in a similar way as dipole excitation. One uses the ansatz

$$\vec{V}^{\pm}(t) = \vec{A}(t) e^{\pm i(\omega_{\pm} + \phi_{\pm})} \tag{2.42}$$

and the same approximation as introduced in the case of dipole excitation. According to [Kön95] one obtains

$$\begin{aligned}\rho^{\pm}(t) = \Big| e^{-\frac{\sigma}{2}t}\Big[\rho^{\pm}(0)\cosh(\omega_B e^{i\theta}t) \\ \mp \frac{\rho^{\pm}(0)[\gamma\omega_c + i(\omega_{rf}-\omega_c)] + \rho^{\mp}k_0^{\pm}}{\omega_B e^{i\theta}} \\ \times \sinh(\omega_B e^{i\theta}t)\Big] e^{i\frac{1}{2}(\omega_{rf}-\omega_c)t}\Big|\end{aligned} \tag{2.43}$$

where $\rho^{\pm}(0)$ are the initial radius for the reduced cyclotron motion and magnetron motion and

$$\omega_B = \sqrt{\omega_{B+}\omega_{B-}} \tag{2.44}$$

$$\omega_{B\pm} = \frac{1}{2}\sqrt{(\omega_{rf}-\omega_c)^2 + (\gamma\omega_c \mp k_0)^2} \tag{2.45}$$

$$\theta = \frac{1}{2}(\theta_+ + \theta_-) \tag{2.46}$$

$$\theta_{\pm} = \arctan\left(\frac{\omega_{rf}-\omega_c}{\gamma\omega_c \mp k_0}\right). \tag{2.47}$$

In the case of damping only $k_0 = 0$, i.e. without oscillating electric field. The equation (2.43) reduces to equation (2.35) as it should do. In case of no damping, i.e. $\sigma = 0$, one obtains

$$\rho^{\pm} = \left|\rho^{\pm}(0)\cos(\frac{k_0}{2}t) \mp \rho^{\mp}(0)e^{\pm i\Delta\phi}\sin(\frac{k_0}{2}t)\right| \tag{2.48}$$

which shows how the magnetron and reduced cyclotron motion are bound together and how one motion transforms to another periodically, see figures 2.6 and 2.7.

In the case of a resonance where $\omega_{rf} = \omega_c$ the equation (2.43) becomes

$$\begin{aligned}\rho^{\pm}(t) = \Big| e^{-\frac{\sigma}{2}t}\Big[\rho^{\pm}(0)\cosh(\omega_B e^{i\theta}t) \\ \mp \frac{\rho^{\pm}(0)\gamma\omega_c + \rho^{\mp}k_0^{\pm}}{\omega_B e^{i\theta}}\sinh(\omega_B e^{i\theta}t)\Big]\Big|\end{aligned} \tag{2.49}$$

where

$$\omega_B = \frac{1}{2}\sqrt{\gamma^2\omega_c^2 - k_0^2}. \tag{2.50}$$

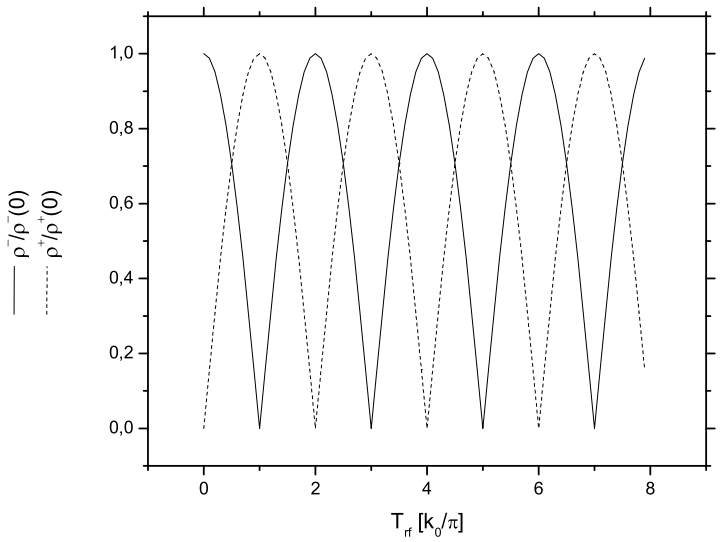

Figure 2.6: Development of the radius in the case of $\sigma = 0$ (no damping) for reduced cyclotron motion ρ^+ and magnetron motion ρ^- as a fuction of excitation time in units of k_0/π.

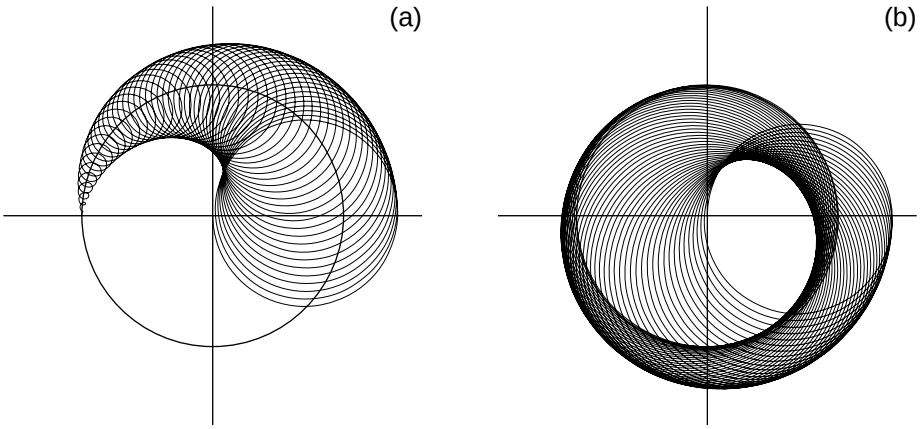

Figure 2.7: Conversion of magnetron motion into reduced cyclotron motion in a quadrupole excitation at the resonance frequency. The first half of the conversion is in a) and the second half of the conversion in b).

Now the size of $\gamma\omega_c$ compared to k_0 will describe how the damping behaves. In the first case $k_0 < \gamma\omega_c$. Now ω_B is real. The damping depends on the time constant $\alpha_\pm = -\frac{\sigma}{2} + \omega_B$. If $\sigma/2 < \omega_B$ the radius of both motions will increase in time. This is the case A in figures 2.8, 2.9 and 2.10 (however, this increase is so small that it is not well visible). When $\sigma/2 = \omega_B$, i.e. $k_0 = \sqrt{2}\gamma\omega_z$ the radius will remain constant (case B). If $\sigma/2 > \omega_B$ the time constant becomes negative and the radius of the motion will decrease (case C).

When $k_0 = \gamma\omega_c$, the time constant has a maximal negative value, which means that the decay of the amplitude will be maximal. This is referred as case D.

In the case of $k_0 > \gamma\omega_c$, ω_B will be complex (cases E and F). It is clear that the increase of the k_0 after the condition $k_0 = \gamma\omega_c$ will not make the decrease of the amplitudes faster. This means that there is an optimal value for U_{rf} for centering the ions.

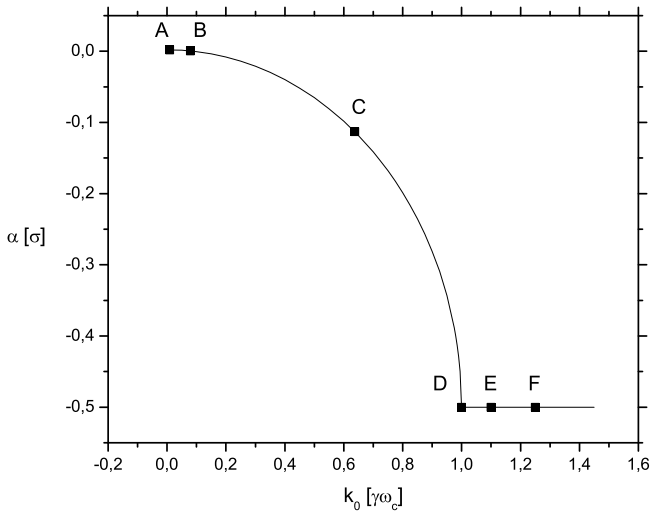

Figure 2.8: Time constant $\alpha_\pm$ in units of σ as a function of k_0 in units of $\gamma\omega_c$. Different k_0 values are A: $k_0 = \frac{1}{10}\sqrt{2}\gamma\omega_z$, B: $k_0 = \sqrt{2}\gamma\omega_z$, C: $k_0 = 8\sqrt{2}\gamma\omega_z$, D: $k_0 = \gamma\omega_c$, F: $k_0 = \frac{11}{10}\gamma\omega_c$, E: $k_0 = \frac{5}{4}\gamma\omega_c$. For all cases $\omega_c = 867266 \times 2\pi$ Hz, $\omega_+ = 865551 \times 2\pi$ Hz, $\omega_- = 1715 \times 2\pi$ Hz, $\omega_z = 54487 \times 2\pi$ Hz. These are the real frequencies for the $^{124}Xe^+$ ions in 7 Tesla magnetic field of JYFLTRAP.

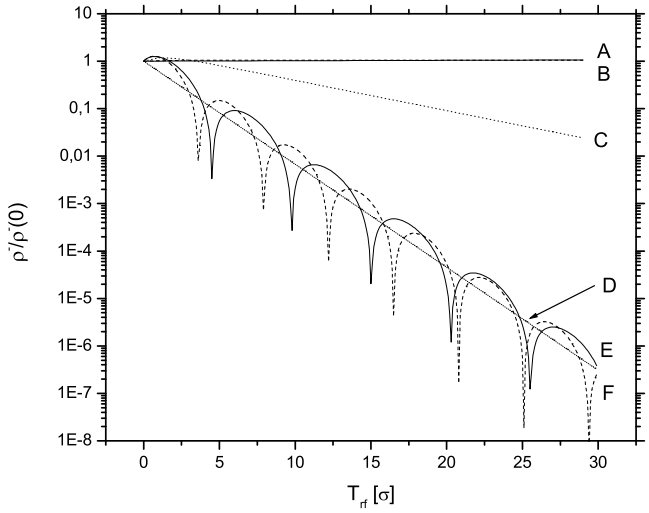

Figure 2.9: Development of the magnetron radius ρ^- with different k_0 values in quadrupole excitation as a function of excitation time in units of σ. A: $k_0 = \frac{1}{10}\sqrt{2}\gamma\omega_z$, B: $k_0 = \sqrt{2}\gamma\omega_z$, C: $k_0 = 8\sqrt{2}\gamma\omega_z$, D: $k_0 = \gamma\omega_c$, E: $k_0 = \frac{11}{10}\gamma\omega_c$, F: $k_0 = \frac{5}{4}\gamma\omega_c$. For all cases $\rho^+(0) = \rho^-(0)$, $\omega_c = 867266 \times 2\pi$ Hz, $\omega_+ = 865551 \times 2\pi$ Hz, $\omega_- = 1715 \times 2\pi$ Hz, $\omega_z = 54487 \times 2\pi$ Hz. These are the real frequencies for the $^{124}Xe^+$ ions in 7 Tesla magnetic field of JYFLTRAP.

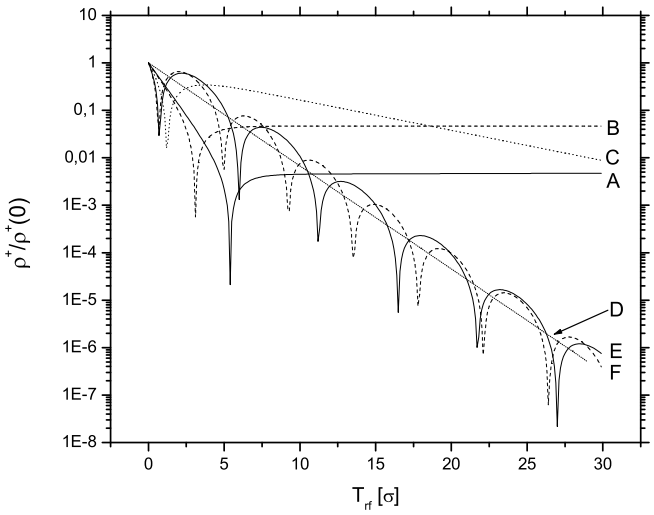

Figure 2.10: Development of the reduced cyclotron motion radius ρ^+ with different k_0 values in quadrupole excitation as a function of excitation time in units of σ. A: $k_0 = \frac{1}{10}\sqrt{2}\gamma\omega_z$, B: $k_0 = \sqrt{2}\gamma\omega_z$, C: $k_0 = 8\sqrt{2}\gamma\omega_z$, D: $k_0 = \gamma\omega_c$, E: $k_0 = \frac{11}{10}\gamma\omega_c$, F: $k_0 = \frac{5}{4}\gamma\omega_c$. For all cases $\rho^+(0) = \rho^-(0)$, $\omega_c = 867266 \times 2\pi$ Hz, $\omega_+ = 865551 \times 2\pi$ Hz, $\omega_- = 1715 \times 2\pi$ Hz, $\omega_z = 54487 \times 2\pi$ Hz. These are the real frequencies for the $^{124}Xe^+$ ions in 7 Tesla magnetic field of JYFLTRAP.

In figure 2.11 one can see the difference between no-excitation and quadrupole excitation at the cyclotron frequency ω_c of the motion of an ion in a buffer-gas filled Penning trap. No-excitation case is close to the case A in figures 2.8, 2.9 and 2.10 where the excitation was done with a too small amplitude. On the other hand, the excitation case corresponds to C or D.

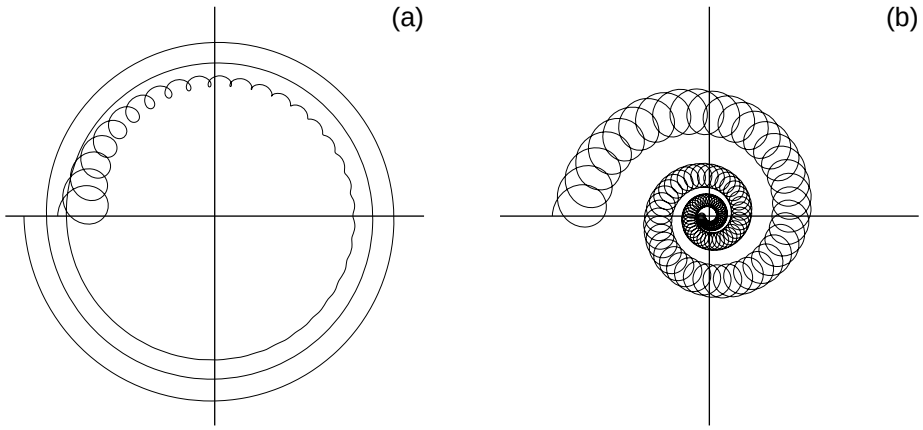

Figure 2.11: Ion motion in radial plane in a buffer gas filled Penning trap. (a) Without excitation, radius of the reduced cyclotron motion decreases and radius of the magnetron motion increases. (b) Quadrupole excitation at the resonance frequency ω_c. Due to the conversion of the magnetron motion into the reduced cyclotron motion radii of the both motions are decreasing.

2.6 Isobaric Mass Separation

Isobaric separation of ions in a Penning trap is based on the mass-selective excitations in a buffer gas. As shown earlier the two dipole excitations can be used to increase the radii of orbits of ions in the trap. Since the magnetron excitation is mass independent (the reduced cyclotron excitation is mass dependent) it is used to increase the radius of ion motion. After the increase of magnetron radius the magnetron excitation is switched to a quadrupole excitation in cyclotron frequency. This mass dependent frequency will then re-center those ions that have this particular $\omega_c = qB/m$. When the ions are then ejected from the trap through a small hole the unwanted ions that have still larger magnetron radius are blocked and only centered ions are extracted out. This feature can be used in mass measurement by scanning

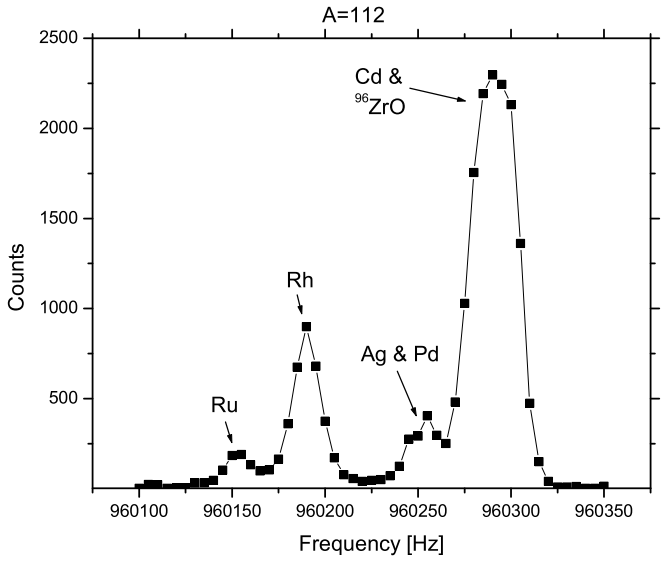

Figure 2.12: Count rate for A=112 as a function of the cyclotron frequency after the magnetron and cyclotron excitations. Spectrum is measured with an MCP detector at JYFLTRAP.

the transmission count rate as a function of cyclotron frequency. An example of a frequency scan is seen in figure 2.12 and later in the chapter 4 in several figures.

From the center frequency of the peak one can deduce the mass of the ion by using the relation $f_c = \frac{1}{2\pi} qB/m$. This is possible since the magnetic field is constant.

2.7 Time-of-Flight Method to Measure Masses

Time-of-flight method was introduced in 1953 [Blo53] and was used for the first time in 1980's for a direct determination of the proton-to-electron mass ratio [Gra80]. In this technique an isobarically pure small sample of ions or a single ion is injected into a Penning trap which is in as good vacuum as possible. Cold trapped ions are first excited with an azimuthal RF field in a dipole mode at magnetron frequency. This will increase the radius of the

orbit of the magnetron motion. After this the ions are excited in a quadrupole mode during the time $T_{rf} = \pi/k_0$. If the excitation frequency $\omega_{rf} = \omega_c$, this converts the magnetron motion to the reduced cyclotron motion as it is shown already in figure 2.6. Since the reduced cyclotron frequency is much higher than the magnetron frequency this conversion will increase drastically the radial energy of the ions. This change is approximately [Kön95]

$$\Delta E_\rho \approx \omega_+^2 \rho_0^2 \tag{2.51}$$

where ρ_0 is the radius after the magnetron excitation. For the off-resonance case the conversion will not happen completely and thus the increase of the radial energy is smaller. Therefore this feature can be used to determine the cyclotron frequency. In general the radial energy has the form

$$E_\rho \propto \frac{\sin^2(\omega_B T_{rf})}{\omega_B^2} \tag{2.52}$$

with

$$\omega_B = \frac{1}{2}\sqrt{(\omega_{rf} - \omega_c)^2 + (k_0)^2}. \tag{2.53}$$

An example of the shape of equation 2.52 is shown in figure 2.13. The theoretical width of the central peak for $T_{rf} = \pi/k_0$ according to [Kön95] is

$$\Delta f \approx \frac{0.8}{T_{rf}}. \tag{2.54}$$

One has to remember that the previous formulation is true only in the vacuum. In the real case there is always some rest gas present; thus one should use the equation 2.45 instead of 2.53. This will then cause widening of the peaks in figure 2.13, i.e. reduce the mass resolution. Another thing that causes distortions for the peak shape are the electrical field imperfections. These imperfections will not change the central frequency itself, but will cause asymmetric resonance curves [Bol96].

After the ejection of the ions they feel a force due to the gradient of the magnetic field when the radial motion interacts with the magnetic field

$$\vec{F} = -\vec{\mu}(\vec{\nabla} \cdot \vec{B}) = -\frac{E_\rho}{B}\frac{\partial B}{\partial z}\hat{e}_z. \tag{2.55}$$

This force will accelerate the ions and so reduce the time needed to fly from the trap to the detector. The time-of-flight can be obtained from the

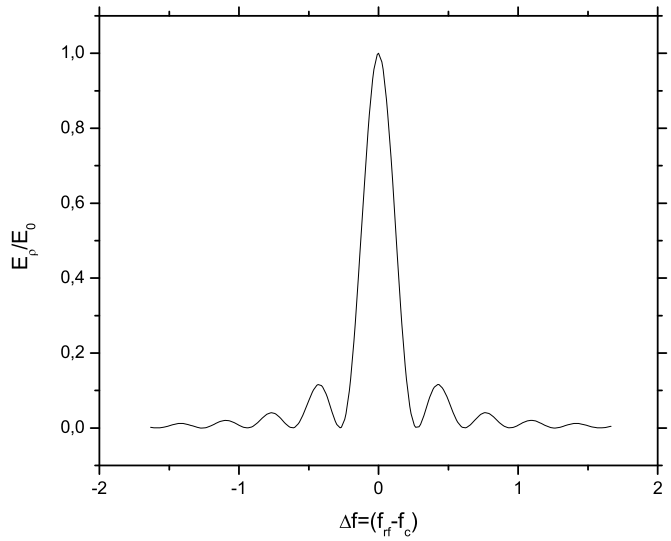

Figure 2.13: Radial energy E_ρ at the end of the quadrupole excitation as a function of detuning Δf for $T_{rf} = \pi/k_0$.

relation

$$T_{TOF} = \int_{z0}^{z1} dz \left[\frac{m}{2(E_0 - qU(z) - E_\rho(\omega_{rf})B(z)/B)} \right]^{1/2} \tag{2.56}$$

where E_0 is the initial axial kinetic energy of the ion, U(z) is the electrostatic potential, B(z) is the magnetic field along the flight path and B is the magnetic field in the trap at excitation region. An example of a TOF spectrum can be seen in figure 2.14.

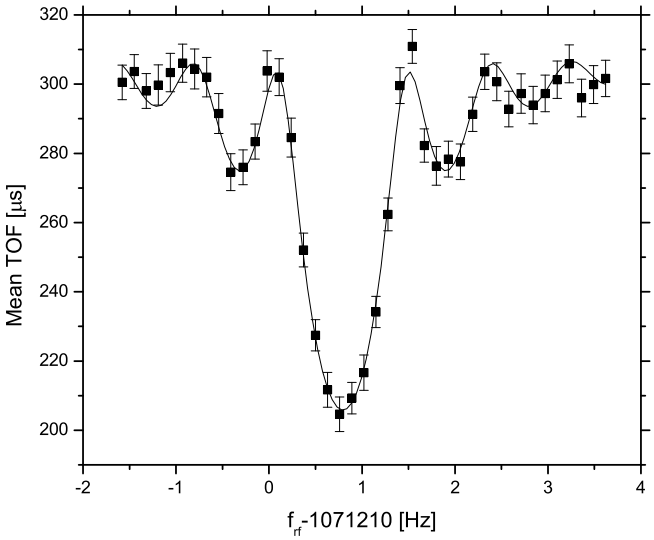

Figure 2.14: Example of a time-of-flight spectrum of $^{85}Rb^{+}$ measured at ISOLTRAP.

Chapter 3

Experimental set-up

The trap built for IGISOL is a double Penning trap that is designed to improve the purity and the quality of IGISOL beams as well as to do precision measurements of atomic masses of exotic isotopes. The first trap, the subject of this thesis, accepts bunched and cooled beam from the RFQ trap and makes the isobaric mass purification. These pure bunches of ions are then extracted and transported to the experimental set ups or to the second trap that will be used in mass measurements in the future. Overview picture of the beam line where RFQ and traps are situated is shown in figure 3.1.

3.1 Injection Beam Line

The beam line between the RFQ cooler/buncher and the Penning trap is shown in figure 3.2. In the injection line there is a double xy-deflector and an Einzel lens immediately after the ejection from the RFQ cooler/buncher, and another double xy-deflector and a special Einzel lens just before the injection to the trap. The idea is that with a double xy-electrodes one can shift the beam parallel to the optical axis and thus be able to enter the Einzel lens directly at the center of the electrode. This is important since due to a strong magnetic field the injection into the trap is difficult and the ion trajectories should be close to the magnetic field lines at the entrance. However, the special Einzel lens just before the first trap electrodes is not really operating as an Einzel lens but as a deceleration electrode that also steers the beam into the trap properly.

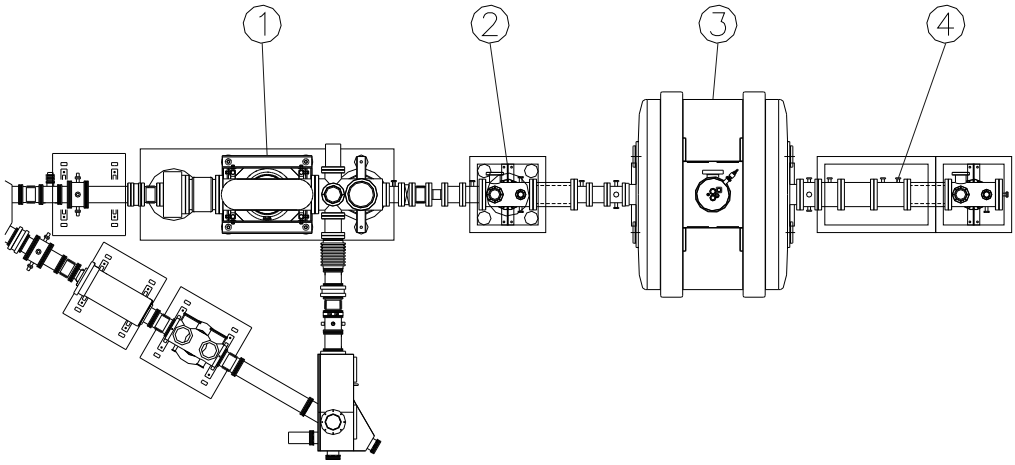

Figure 3.1: Top view of the RFQ and the Penning trap. 1. RFQ cooler/buncher, 2. Injection beam line to the trap , 3. Trap system, 4. Ejection beam line.

3.2 Test Ion Source

The test ion source is a commercial electron impact ion source made by Balzers. The ion source consists of a tungsten filament and an ionization chamber that are at different voltages (figure 3.3 and table 3.1). A current of 3-4 A is applied to the filament to heat electrons out. These electrons are then accelerated into the ionization chamber in which the gas is also fed in. This chamber has a positive voltage compared to the filament. The electron flux will ionize the gas atoms which then are accelerated by a set of acceleration and lens electrodes. The quality of the beam of this ion source is not very good. Therefore this source is only used in testing the ion optics. The main problem is that the cone angle of the beam that it creates is $\approx 3°$. The other problem is that the source needs a switch box of its own for its voltage on and off operation. Since no extra switch box was available the ion source was pulsed with the same box as the injection wall of the purification Penning trap. This meant that when the wall closes some of the ions still hit the wall creating electrons that were then trapped in the local potential maximum of the injection wall area. These electrons then ionized

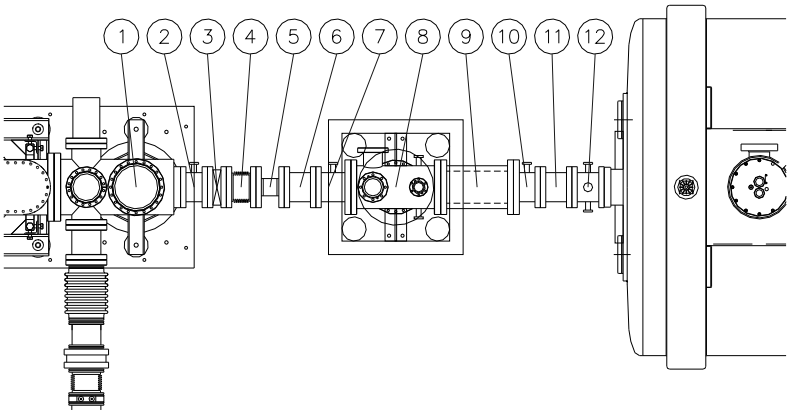

Figure 3.2: Top view of the connecting beam line between the RFQ and the Penning trap. 1. Double xy deflector, 2. Einzel lens, 3. Valve, 4. Bellows, 5. Insulator, 6. Test ion source, 7. Double xy-deflector, 8. Pumping chamber with MCP and FC, 9. Bellows, 10. Einzel lens, 11. Insulator, 12. Plug chamber.

gas molecules while circulating in the magnetic field. These new ions then disturbed the measurements. So that no reliable and stable trap operation could be reached. However, the source was successfully applied to the ω_- and ω_+ excitation of Xe ions, see figures 4.1 and 4.2.

Electrode	U[V]
Chamber	GND
Filament	-74
Extraction	-390
Lens el. 1 and 3	-140
Lens el. 2	-40

Table 3.1: Typical voltages applied to the test ion source.

3.3 Superconducting Magnet

The largest part of the JYFLTRAP is the superconducting magnet that is used to create the magnetic field for the Penning trap. This 7.0 T actively

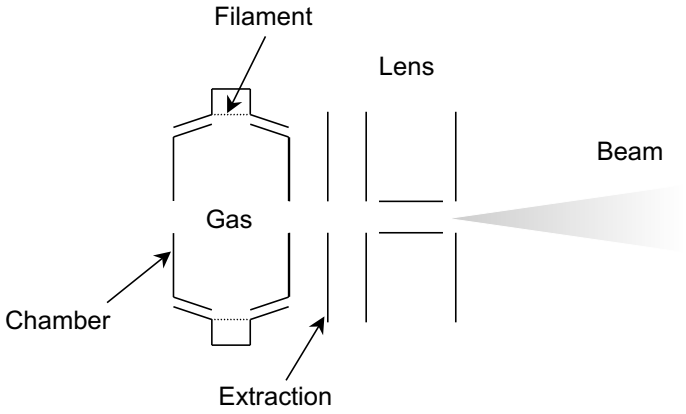

Figure 3.3: Schematic drawing of the test ion source.

screened magnet system is made by Magnex Scientific Ltd [Mag99]. It has a warm bore with a diameter D=160 mm and a length L=1012 mm. This magnet has two 1 cm^3 homogenous magnetic field regions at 10 cm distance to both directions from the magnet center. In these regions the homogeneity of the magnetic field is below 10^{-6} and 10^{-7}, respectively. The plot of the magnetic field is shown in figure 3.4.

The magnet coils must be cooled to liquid helium temperature to reach superconducting state. There are two separate cryostats one for liquid helium and another for liquid nitrogen. Their volumes are 420 liters and 200 liters, respectively. The liquid nitrogen is only used to cool the outside of the liquid helium cryostat to minimize the liquid helium consumption. This is done since 1 liter of liquid nitrogen costs the same as one liter of milk and liquid helium is 15 times more expensive. The magnet consumes about 1.2 liters of helium and 10 liters of nitrogen per day. Liquid helium cryostat must be filled about every 130-150 days to keep the magnet superconducting. Liquid nitrogen cryostat must be filled every two weeks (manufacturer gives guarantee for 100 days and 14 days, respectively).

3.4 High Voltage Platform

During normal operation, the HV platform, which accommodates the RFQ cooler/buncher and the Penning trap as well as the connecting beam line, is set to 30 kV. In addition, the potential of the connecting beam line is

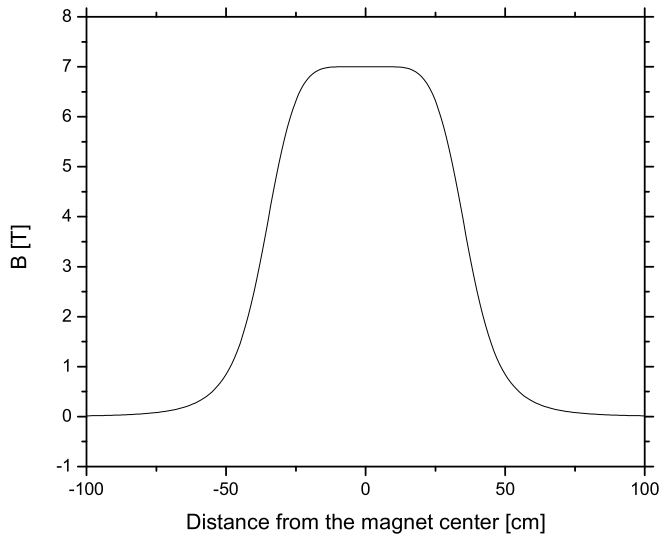

Figure 3.4: Field plot of the superconducting magnet used to create the magnetic field for the Penning tarp.

lowered by 900 V compared to the HV platform of the magnet itself. In off-line studies with a test ion source the HV platform can also be set to a lower potential. The original plan was to use 38 kV in the high voltage platform, but in that voltage region there were sparks every now and then and thus the HV had to be lowered to the level of 30 kV.

3.5 Electrode Structure and Vacuum

The vacuum tube inside the bore of the magnet is mounted with an adjustable support to allow the alignment of the tube along the magnetic field. This was done by using a special device inserted into the vacuum tube. In this device electrons were created by heating the filament at the magnet center and accelerated towards detection plates, see figure 3.5. These electrons had to travel along the magnetic field lines through a pin hole (diameter D=0.5 mm, at both sides, 5 cm distance from the center) to the segmented detector plates which also had pin holes at the center (D=0.2 mm, both sides at 50 cm distance from the magnet center). These segmented detector plates were at both ends of the vacuum tube. By comparing the electron current at the segments one could estimate the position of the tube inside the magnet.

Centering the tube required adjusting the ends in such a way that the current through both 0.2 mm pin holes of the segmented plates had its maximum.

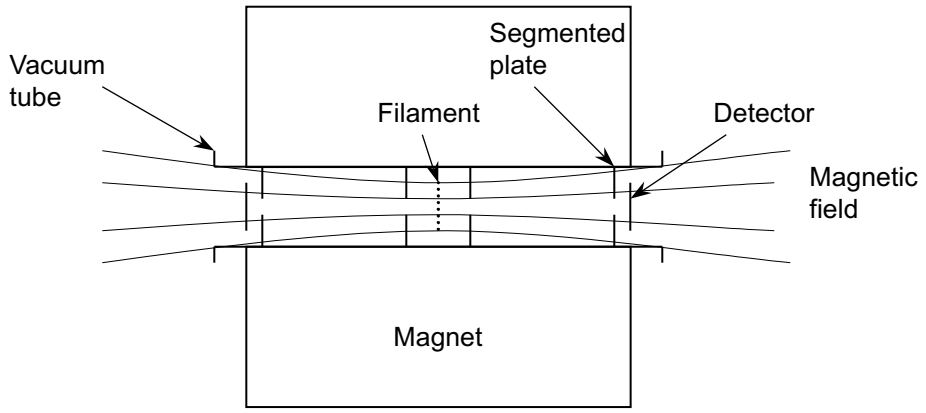

Figure 3.5: Schematic picture of the alignment device.

The electrode structure of the Penning trap is made of gold plated copper cylinders and aluminium oxide insulators between them. The structure consists of seven subsegments that are bound together with holders and bars made of aluminium. The whole trap structure stands on titanium wheels that are connected to the holders. The total length of the trap structure is 1046 mm. The trap structure is presented in figures 3.6, 3.7 and 3.8. Dimensions of the electrodes in the trapping region were obtained by scaling the dimensions of the purification trap at ISOLTRAP [Rai97]. The inner diameter of the trap at IGISOL is 32 mm and the lengths of the ring electrode, the first and the second correction electrodes are 18.5 mm, 12.8 mm and 6.7 mm, respectively. The distance between the electrodes is 0.5 mm. A photograph of the first trap is shown in figure 3.9.

Special holders that have three holes and Macor disks are mounted at both ends of the trap structure. Each Macor disk has 30 pins that are connected by silver wires to the trap electrodes for electrical connection. At both ends of the vacuum tube there are plug chambers. These chambers consist of 30 sockets and three rods that are the counterparts for the pins and the holes at the end of the trap.

Due to the plug chamber solution and the fact that the whole trap structure is on wheels, the system can be easily opened and closed. The trap can be rolled out or in by using an insertion stand outside the magnet.

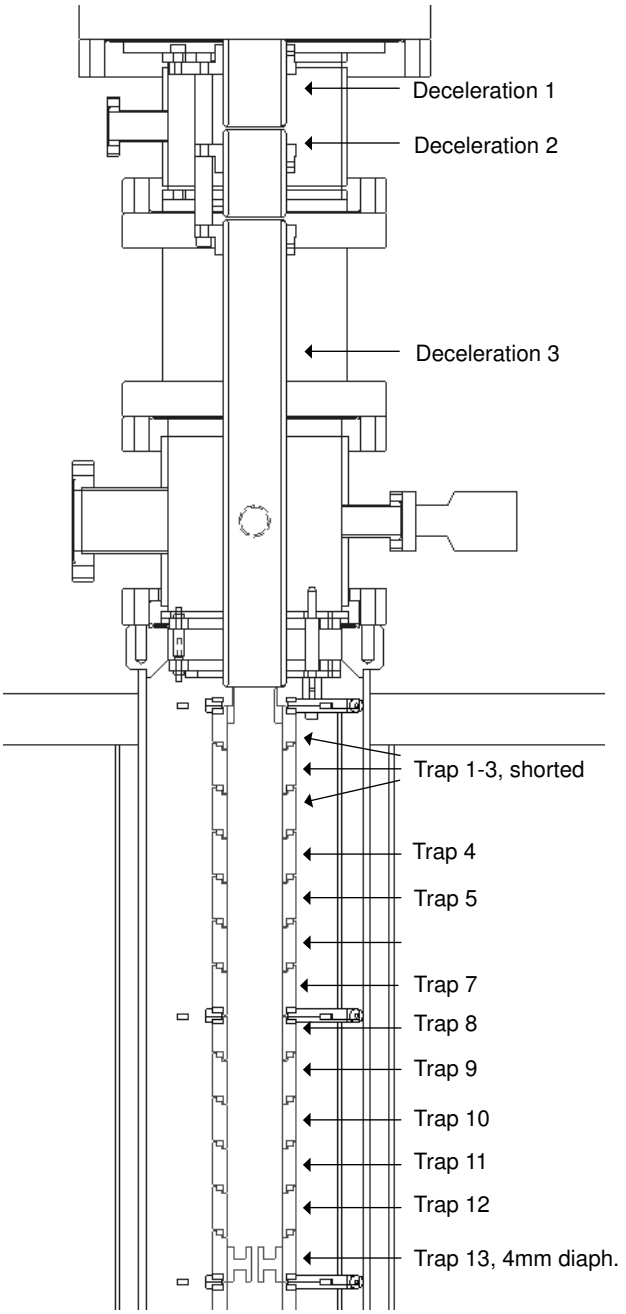

Figure 3.6: Electrode structure of JYFLTRAP part a.

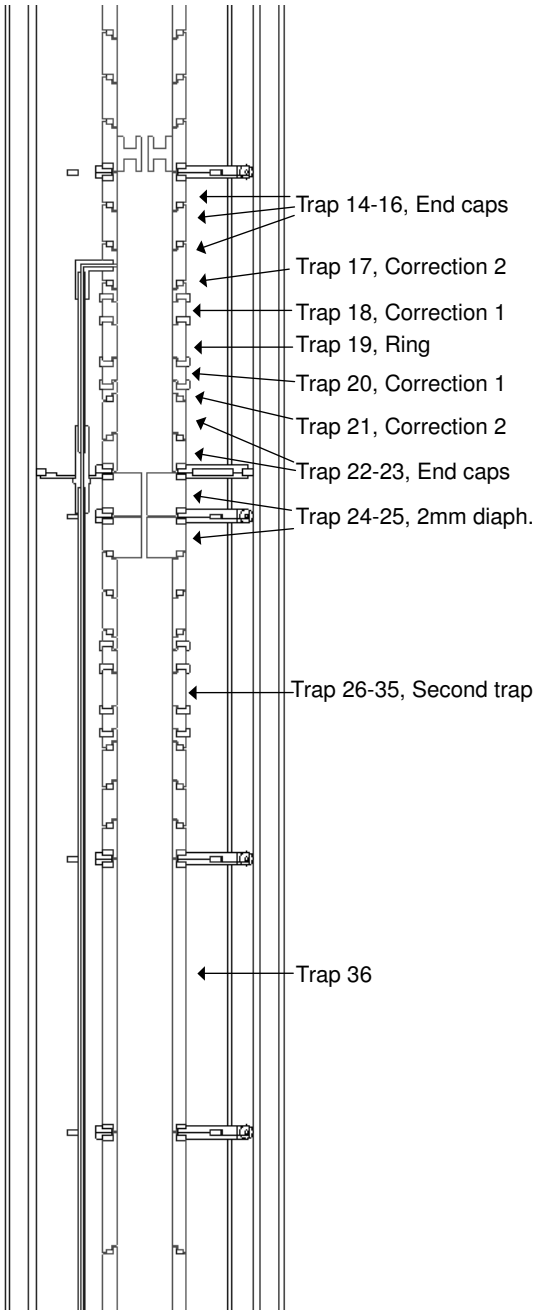

Figure 3.7: Electrode structure of JYFLTRAP part b.

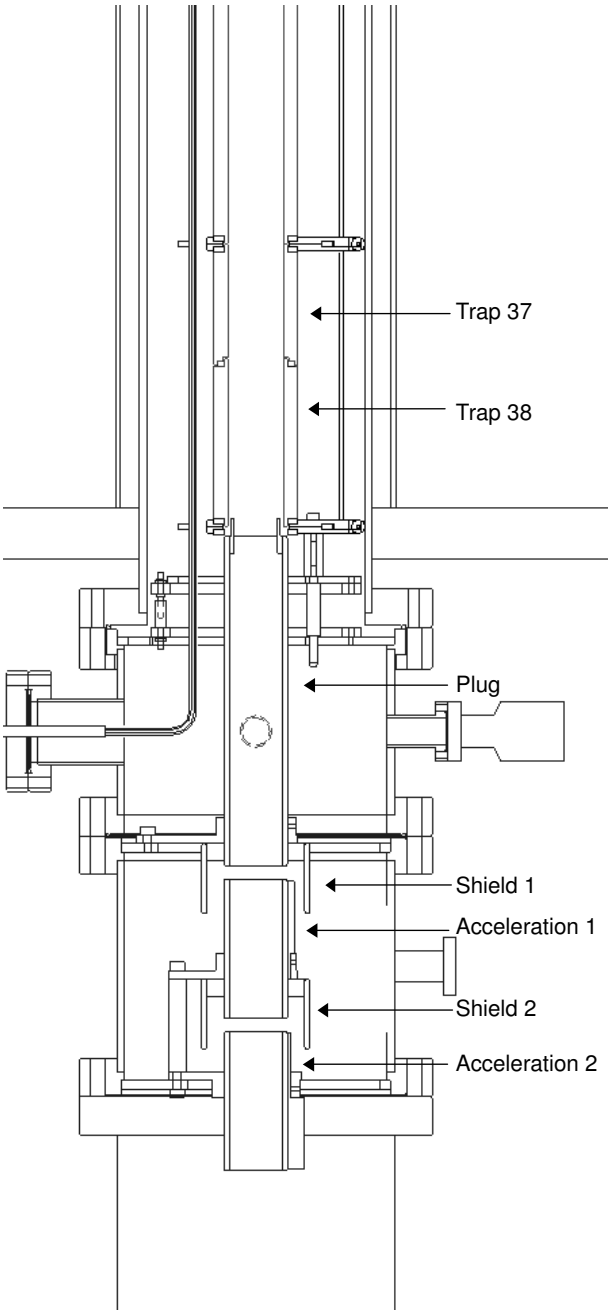

Figure 3.8: Electrode structure of JYFLTRAP part c.

All metallic vacuum parts, vacuum tube, pumping chambers etc., are made of acid proof steel. An ultra high vacuum $\sim 10^{-8}$ mbar is achieved with two turbomolecular pumps of 1000 l/s placed at both ends of the trap tube. The gas feeding system to the purification trap is shown in figure 3.10.

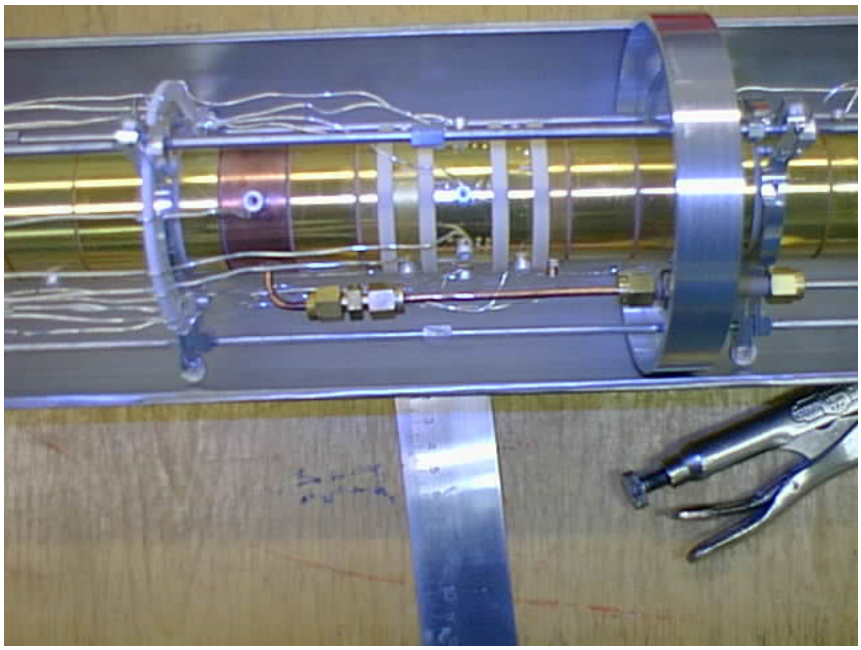

Figure 3.9: Photograph of the first trap.

3.6 Ejection Beam Line

Extraction beam line, see figure 3.11, from the trap consist of three acceleration electrodes that are called a plug electrode, acceleration 1 and acceleration 2 electrodes. These three electrodes are still on the high voltage platform, see figure 3.8. The purpose of these three electrodes is to re-accelerate the ion beam in such a way that no electron traps are created at any point. There is also two shield electrodes to prevent the creation of electron traps. After the second extraction electrode there is an insulator and all the beam tubes after it are on the ground potential. After the insulator there is a ground electrode and a grid. A negative voltage is applied to the grid to form a barrier for electrons. The purpose is to prevent electrons to fly from the ground to the

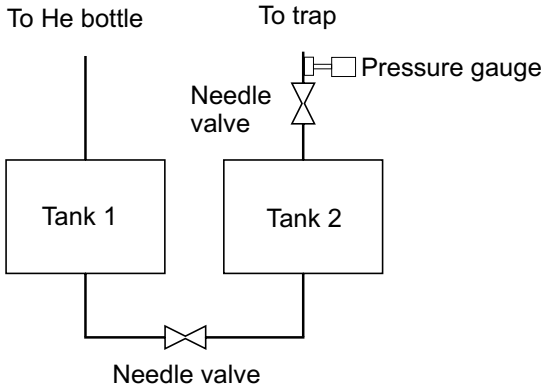

Figure 3.10: Schematic picture of the present gas feeding system. Volumes of the tanks are 0.8 liters each.

high voltage platform. Then there are a single xy-deflector and an Einzel lens which aim to focus the beam to the MCP detector or even further to a spectroscopy set up.

3.7 Beam Diagnostics and Ion Detection

In the injection line between the RFQ and the Penning trap there is a Faraday cup (FC) and an MCP detector, see figure 3.2. The Faraday cup is used when the line is tuned by using either the test ion source or with stable beams produced by IGISOL; usually xenon. The MCP detector can also be replaced with a silicon detector to detect radioactive decay of stopped ions.

At the ejection side of the trap there is a Faraday cup (FC), see figure 3.11 and table 3.2, and a double MCP detector, see figure 3.12. The Faraday cup is used in beam tuning and the MCP is used for low intensity beams ($< 10^5$ ions/s), typically in connection with mass measurements. There is also a possibility to set up a scintillator β detector or a Si-detector and a Ge-detector for radioactivity measurements at the end of the ejection line (figure 3.13).

3.8 Electronics and Control

Most of the trap electronics is placed in two racks on the high voltage platform. The main components are Spellman MP-series power supplies, which

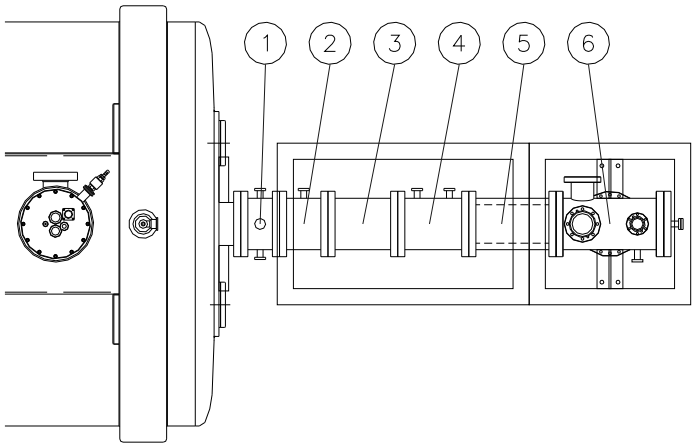

Figure 3.11: Extraction line of JYFLTRAP. 1. Plug chamber, 2. Extraction electrodes, 3. Insulator, 4. Ground electrode, xy-deflector and Einzel lens, 5. Bellows, 6. Pumping chamber with MCP and FC

provide power for the first double xy-deflectors, for the first Einzel lens in the injection line and the last acceleration electrode. ISEG power supplies provide voltages for all trap electrodes, the deceleration electrodes, the second double xy-deflector at the injection side and for the first two acceleration electrodes. There are also two Hewlett Packard 33210A function generators that provide the frequency and the amplitude for the magnetron and cyclotron excitations. These RF amplitudes are coupled via self-made coupling boxes to DC voltages before applied to the segmented ring electrode. The fourth important part in the high voltage platform composes of two switch boxes that are used to switch the trap electrode voltages between capturing and trapping settings at injection side and between trapping and ejection settings at the ejection side. These boxes are home made with commercial switch chips made by Super Tech.

There is also one rack on the ground level housing Spellman MP-series power supplies for ion optics and the necessary electronics for the MCP detector, a timer/counter and a constant fraction discriminator.

Electronic devices are controlled by using a normal PC. The communication with the electronics is done via a CAN-bus [CAN] and WAGO units [WAGO]. There is also a PPG-100 arbitrary pulse generator card [PPG] in

Object	D_{in} [mm]	D_{out} [mm]
Collimator	4	27
Suppression	6	27

Table 3.2: Dimensions of the Faraday cups used in the injection and ejection lines. D_{in} and D_{out} are inner and outer diameters, respectively. A negative voltage can be applied to the suppression electrode to prevent the escape of electrons from the cup.

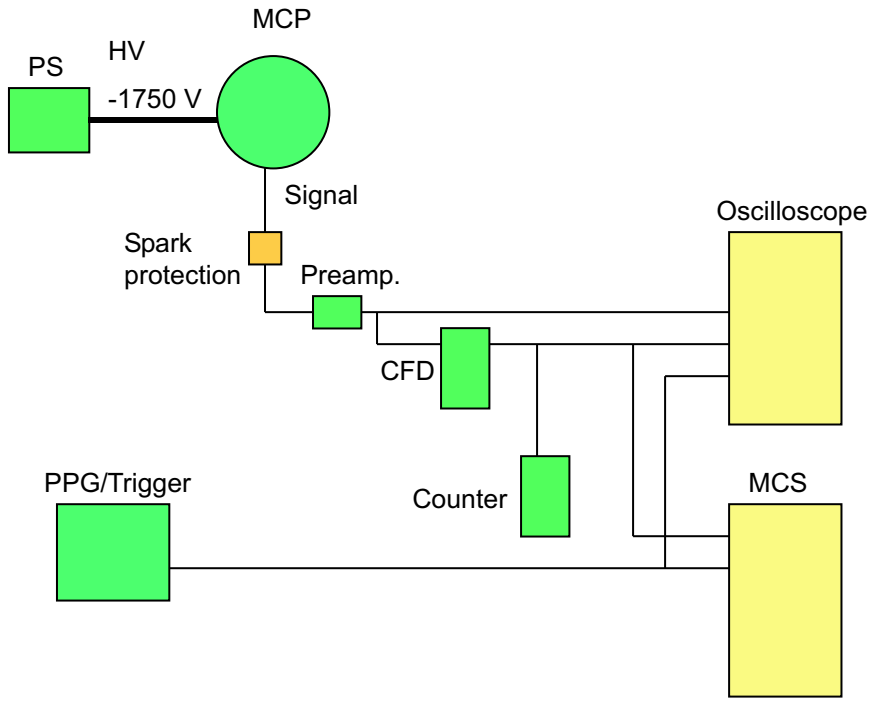

Figure 3.12: Schematic picture of the MCP set-up at the ejection side of the trap.

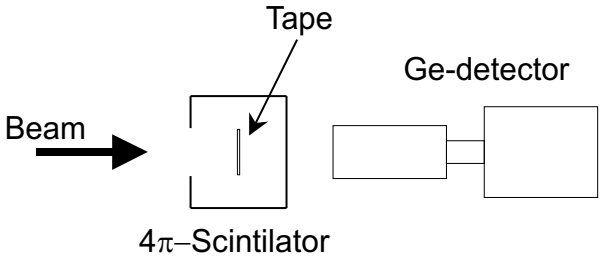

Figure 3.13: Schematic picture of the set up for radioactivity measurements.

the computer to provide all the timing signals for the trap. The user interface uses Lab-VIEW. An overview picture of the control system is shown in figure 3.14. More detailed description can be found in the reference [Hak03].

3.9 Simulations

All simulations were done by using a commercial SIMION program that is a good tool for calculation and visualisation of trajectories of particles in electromagnetic systems.

Since the program itself did not support the magnetic field, that had to be created by making magnetic potential points in such a way that inside a cylindrical tube the field B would be correct. The Magnex company provided the magnetic field plots which allowed the calculation of the values of the potential points in a following way

$$\phi(z + \Delta z, R_0) = \Delta z B(z, r = R_0) + \phi(z, R_0). \tag{3.1}$$

After scaling the magnetic field and the radius to the right units, i.e B in Gauss and r in mm, potential points were included in simulations by using a geometry file.

Buffer gas was added by a user program. Collision with buffer gas molecules were simulated with viscous damping force

$$\ddot{u} = -\frac{q}{m_{ion}}(\frac{\dot{u}}{K} - \frac{v_{th}}{K_{th}}) \tag{3.2}$$

where u stands for any of the coordinates x,y, or z and K is the mobility of the ion in a gas of particular density, v_{th} is thermal velocity and K_{th} is the corresponding mobility. The ion mobilities have been measured for several

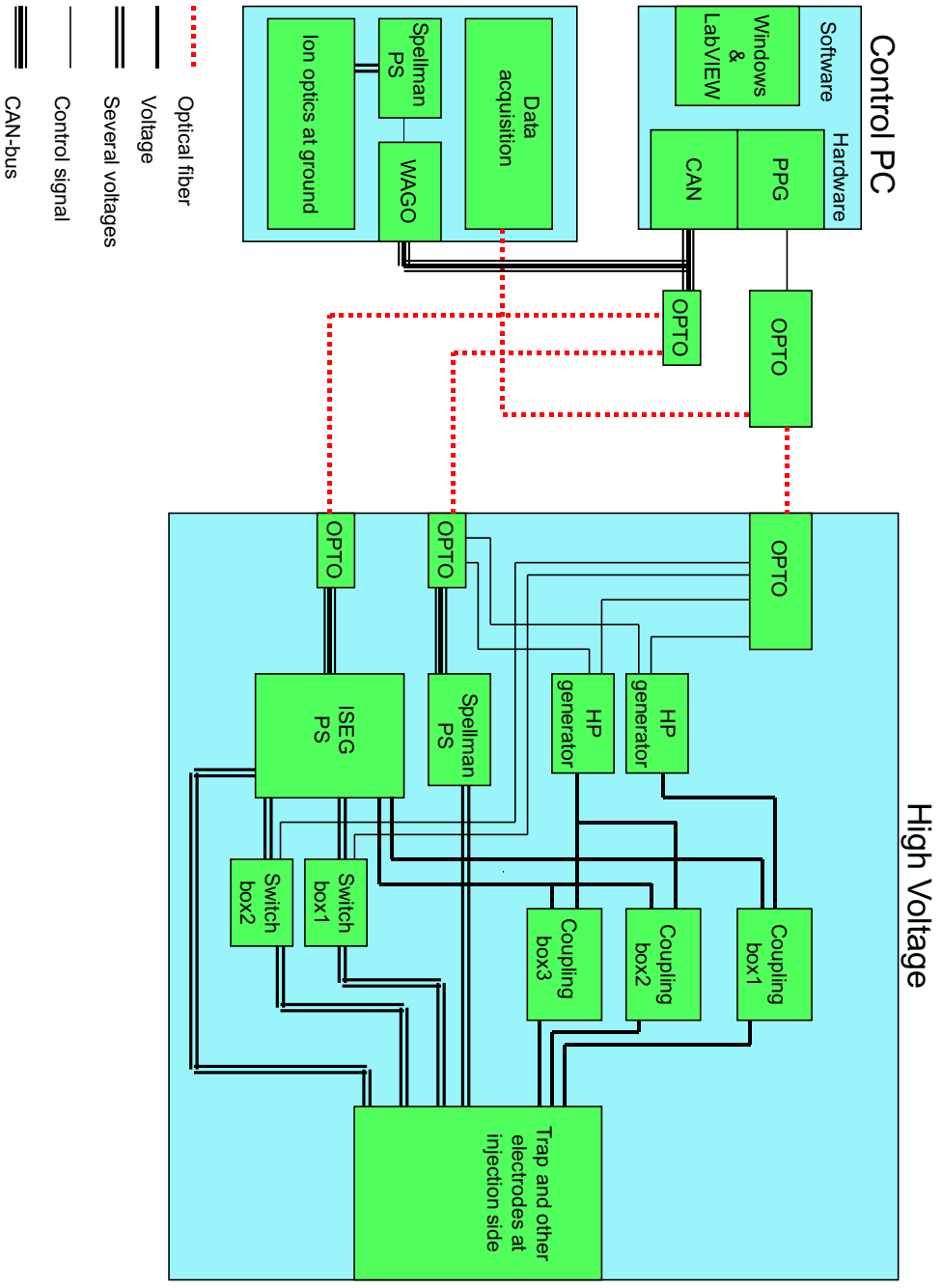

Figure 3.14: Schematic picture of electronics and the control system.

ions in various buffer gases [Ell76] and [Ell78]. These values are normalized to normal pressure p_0 and temperature T_0 in a following way

$$K = K_0 \frac{T}{T_0} \frac{p_0}{p}. \tag{3.3}$$

However, the experimental data is available only at low velocities and so the elastic collisions have been used for calculating the ion mobility at higher velocities.

$$K_{el} = \frac{q}{m_{ion}} \frac{(m_{ion} + M_{gas})^2}{m_{ion} M_{gas}} \frac{1}{n\sigma v_{ion}} \tag{3.4}$$

where n is the density of the buffer-gas, σ is the cross-section for elastic hard sphere collisions and v_{ion} is the velocity of the ion [Lun99].

The user program of SIMION uses a discrete model to calculate the effect of the viscous damping, i.e. after each (user defined) time step a new damping force is calculated that is then applied to the ion during the next step. This kind of model is not very realistic since it does not take into account scattering of the ions. However, in our case when helium is used as buffer gas and ions are much heavier this model can provide rather good approximation for motion of ions.

However, the most important things that have been simulated were the injection and ejection lines of the trap. For example, if one assumes that the 38 keV beam coming out from the RFQ has 1 eV energy spread and the emittance of 3 π mm mrad then corresponding emittance at 900 eV would be 20 π mm mrad. Assuming now that the diameter of the beam is 3 mm, i.e. the cone angle is 2.2 degrees this will give 100 % efficiency for the injection into the trap when using the same values for the electrodes as in the reality, see tables 3.3 and 3.4 describing the applied voltages to the electrodes.

Another important area where the simulations were useful was localizing the electron traps created in the injection and especially in the ejection areas. As a result of these simulations a new acceleration electrode structure was created. This was shown earlier in figure 3.8.

3.10 Operating Procedures and Parameters for JYFLTRAP

This chapter introduces the values of the operating parameters for JYFLTRAP.

Gas feeding for the helium buffer gas is done through a pressure regulation system (figure 3.10). Since we do not have a way to measure the pressure inside the trap it is measured in the gas feeding line into the trap. During normal operation the pressure is between $9 \times 10^{-3} - 9 \times 10^{-2}$ mbar, most commonly the pressure has been around 2.0×10^{-2} mbar. According to estimation this corresponds roughly to 1×10^{-4} mbar inside the first trap.

The high voltage of the cooler platform was set to 30 kV in all tests and the high voltage platform of the trap 90-99 V above that. The connecting beam line between the RFQ and the trap is normally set to 900 V lower than the high voltage platform of the trap. The outer shell of the RFQ is 800 V lower than the HV platform of the cooler. The voltages used can be found in tables 3.3, 3.4 and 3.5. An example of an often used timing scheme can be found in table 3.6.

	U [V]
RFQ X1 left	-790
RFQ Y1 down	-802
RFQ X2 left	-792
RFQ Y2 down	-798
RFQ Einzel	-410
Beam line	-900
Trap X1 left	-872
Trap Y1 down	-903
Trap X2 left	-862
Trap Y2 down	-900
Deceleration 1	-900
Deceleration 2	-590
Deceleration 3	-450

Table 3.3: Normal operating voltages for injection line ion optics. Other electrodes in xy-deflectors in RFQ are connected to the outer shell of RFQ i.e. to -800 V and in trap line to the line itself i.e. to -900 V.

It is worth remembering that the proper timing scheme and excitation amplitudes depend on the pressure in the trap as well as on the voltages applied to deceleration and trap electrodes.

The trapping is done by using a so called dynamic trapping mode, which

	Trap open U [V]	Trap closed U [V]
Trap 1-3, shorted	-310	-310
Trap 4-10	-310	-310
Trap 11	-110	-110
Trap 12	-110	-110
Trap 13, 4mm diaph.	-110	0
Trap 14, End cap	-110	-10
Trap 15, End cap	-110	-10
Trap 16, End cap	-110	-10
Trap 17, Correction 2	-110	-34.06
Trap 18, Correction 1	-110	-83.27
Trap 19, Segmented Ring	-100	-100
Trap 20, Correction 1	-130	-83.08
Trap 21, Correction 2	-130	-34.28
Trap 22, End cap	-130	0
Trap 23, End cap	-130	0
Trap 24, 2mm diaph.	-130	0
Trap 25, 2mm diaph.	-130	-130
Trap 26-35, second trap	-130	-130
Trap 36, long	-130	-130
Trap 37, long	-130	-130
Trap 38, long	-220	-220

Table 3.4: Typical operating voltages for the trap electrodes. See also figure 3.15. The voltages at the correction electrodes have to be set in such a way that the output voltage is 83.00 V in the case of correction 1 and 34.00 V in the case of correction 2. These voltages have to be checked if the shape of the resonance peak is not symmetric after the ω_c excitation.

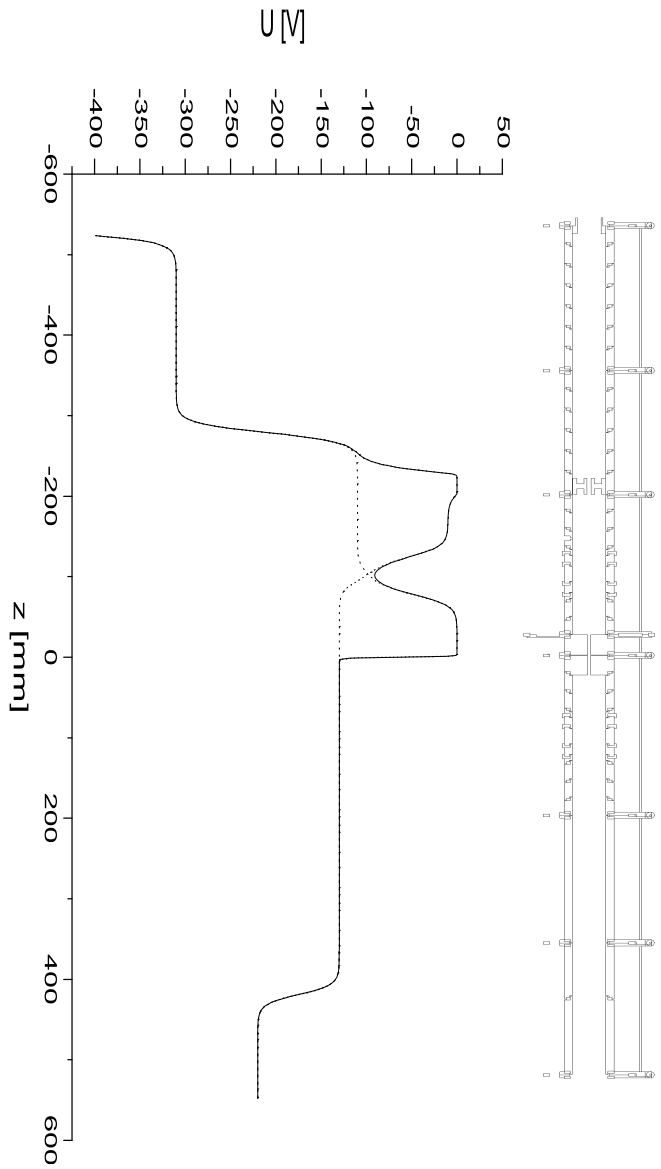

Figure 3.15: Potentials used in electrodes.

	U [V]
Plug	-220
Shield 1	-370
Acceleration 1	-530
Shield 2	-530
Acceleration 2	-1200
Grid	-1000
XY1	+220
XY2	+320
Einzel	+12000

Table 3.5: Typical operating voltages for extraction line optics.

	Time
Cooler ejection	0-17 μs
Trap wall 1 open	0-155 μs
Axial cooling	155 μs-330 ms
ω_- excitation	330-345 ms
ω_c excitation	345-445 ms
trigger for MCS	444 900-445 000 μs
Trap wall 2 open	445-450 ms

Table 3.6: Example of normal timing scheme used in test experiments. Cycle time in this example is 450 ms and pressure in gas line $p \approx 2 \times 10^{-2}$ mbar. The amplitudes for ω_- excitation $A(\omega_-)$=120 - 160 mV and for ω_c excitation $A(\omega_c)$=150 - 200 mV.

means that the injection into the trap is done in bunches. When the ion bunch is entering the trap the potential of the injection wall is lowered in such a way that the ions can enter the trap. Immediately after this the potential is raised again and the ions are trapped. This is illustrated in figure 3.16. The time

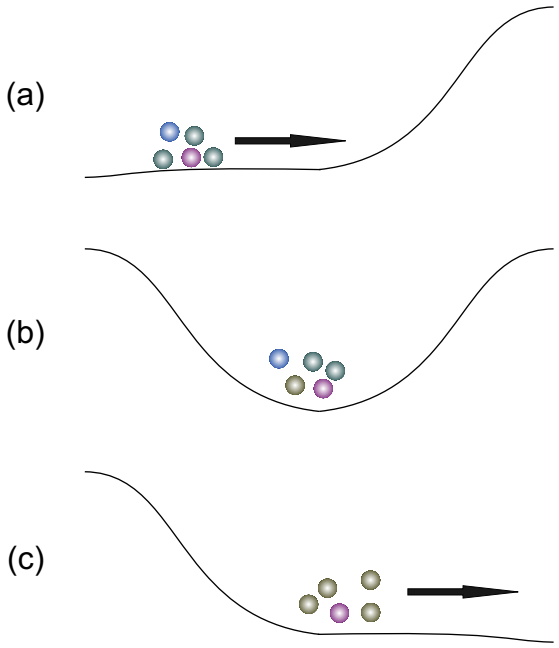

Figure 3.16: Dynamic trapping scheme: a) the ion bunch can enter the trap when the potential of injection wall is lowered, b) after this the potential is lift up and ions are trapped and c) ejection wall is lowered and the ions are ejected.

between closing the injection wall and the beginning of magnetron excitation is used in the axial cooling. It is necessary that the ions are at the bottom of the quadrupole potential, i.e. at the center of the ring electrode before the excitation can be done properly. The long time used in axial cooling in table 3.6 is due to the fact that some ions are lifted to higher potential when injection wall closes. This can be improved by changing the used potential scheme; however so far we have not got time to test this properly. Then during the magnetron excitation an oscillating electric field is connected to the azimuthally segmented ring electrode in a dipole mode. Actually, since we do not have a frequency inverter we have connected the RF field only to one quadrant and all the other quadrants are connected to DC voltages.

The frequency used in magnetron excitation has been f_- ≈1715 Hz and the amplitude $A(\omega_-)$=120 - 160 mV. During this magnetron excitation all ions are excited in orbits that have larger radius. After this the quadrupole RF field will be switched on. Also this is applied only on two opposite quadrants and the others remain at DC voltage, from the same reason as in the dipole excitation. Anyway, this excitation will recenter those ion species into the trap axis that have this particular cyclotron frequency $\omega_c = \frac{qB}{m}$ while the other ions, that have a different mass and thus a different cyclotron frequency will remain in larger orbits. Now ejection through a small diaphragm will allow only those ions that are close to the trap axis to be extracted.

Clean, monoisotopic bunched beams will then be transported to an MCP detector or to a spectroscopy set-up.

Chapter 4

Experimental Results

4.1 Tests with Electron Impact Ion Source

The first test with the trap was done with a commercial test ion source. Even if the quality of the beam of this source was poor it was necessary to have it since this made it possible to test the Penning trap independently of other IGISOL activity. These tests were done with several different high voltage settings between 3-40 kV. All the data shown in this chapter has been measured with an MCP detector unless something else is mentioned.

During the first tests it was found out that in the magnetic field region there were some places with a local maximum in electrostatic potential. Here electrons were trapped and during the circulation in the magnetic field electrons ionzied the residual gas causing ion spurts detected in an MCP detector. After several attempts all electron traps were finally localized. Most of them were at the injection or extraction areas. Their removal required a careful and detailed improvement of the deceleration and acceleration electrodes.

When working with the test ion source the functioning of the magnetron excitation ω_- and the reduced cyclotron excitation ω_+ both applied in a dipole mode was demonstrated. In this mode ions are excited by applying oscillating RF voltage to larger orbits and subsequently during the ejection through a 2 mm diameter exit hole the count rate reduces to its minimum value at the resonance frequency. In the case of the magnetron excitation all ions will attain a larger radius. An example of this is shown in figure 4.1. However, this very first successful magnetron excitation is not as good as it should be when it is done properly. Since the amplitude and the excitation

time have to be chosen so that the minimum value in the nuber of counts is at zero level. In the case of the reduced cyclotron excitation only those ions that have this particular reduced cyclotron frequency will move to larger orbits. An example of this is shown in figure 4.2. This reduced cyclotron excitation has been done at the frequency ω_+=3 357 850$\times 2\pi$ that is the reduced cyclotron frequency for O_2. From the spectra one can see how the O_2 peak disappears after the excitation.

The frequency-scan spectra were collected with the Standford SR430 multichannel scaler. Regardless several attempts to see a cyclotron resonance

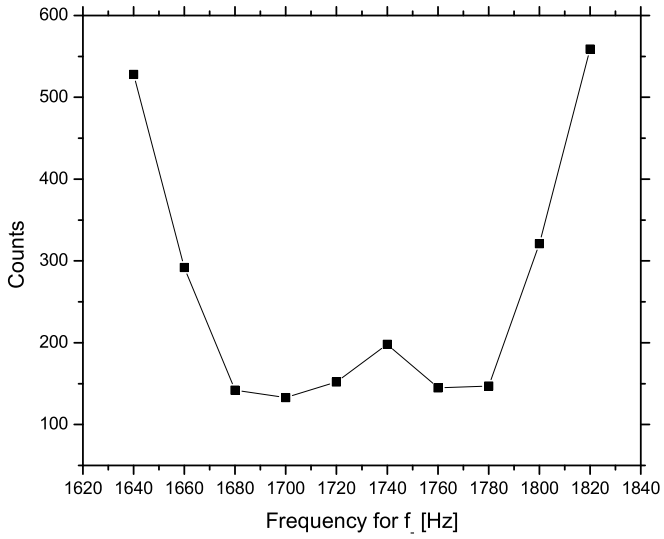

Figure 4.1: The first successful magnetron excitation (ω_-). (Performed 9th of September 2002). Counts in the MCP detector as a function of the magnetron excitation frequency. Other parameters in this case where: $T_{cooling}$=200 ms, $T_{excitation}$=50 ms, $p_{He} = 2.0 \times 10^{-2}$ mbar and A(ω_-)=300 mV. Test was done with ionized Xe gas.

it was not seen properly. The best result is shown in figure 4.3. Here the frequency step has been rather big, but nevertheless ^{129}Xe isotope is visible. The amplitude for the ω_c excitation has been exceptionally high, 1 V, and that might be the reason that the resonance was seen at all.

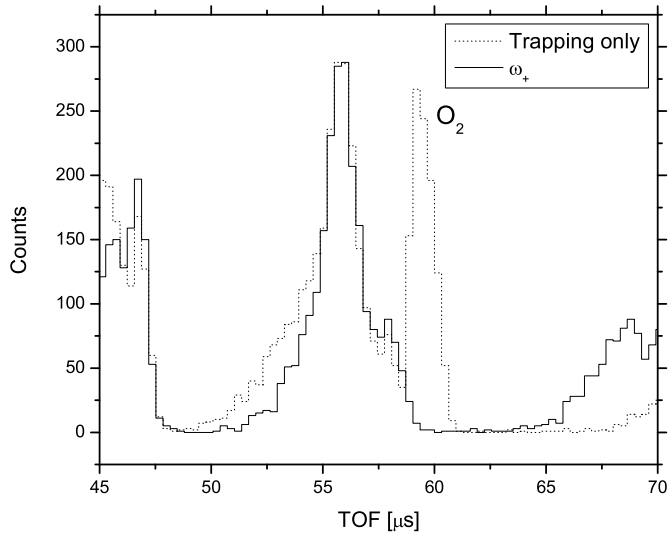

Figure 4.2: The first successful reduced cyclotron excitation (ω_+) for oxygen. (Performed 10th of September 2002). The spectra have been recorded with the multichannel scaler showing the counts in the MCP-detector as a function of TOF. Zero time corresponds to opening of the ejection wall of the Penning trap. Dotted line corresponds the spectrum with trapping only and the solid line after the reduced cyclotron excitation at frequency ω_+=3 357 850$\times 2\pi$ Other parameters in this case where: $T_{cooling}$=200 ms, $T_{excitation}$=100 ms, $p_{He} = 2.0 \times 10^{-2}$ mbar and A(ω_+)=2V.

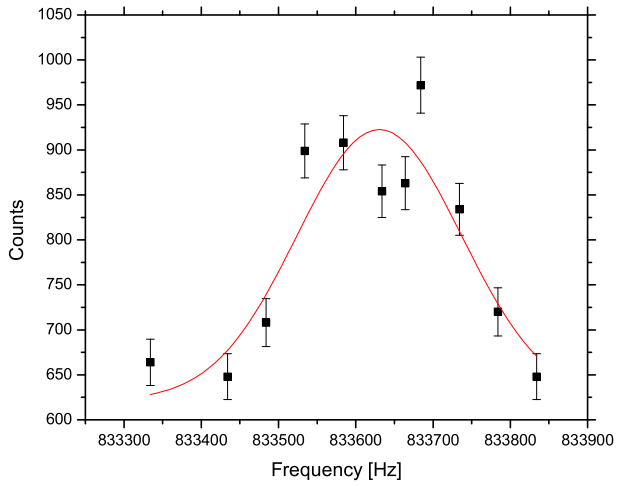

Figure 4.3: The first observation of the cyclotron excitation (ω_c). (Performed 10th of October 2002). Counts in the MCP-detector as a function of cyclotron excitation frequency for ^{129}Xe. Other parameters in this case where: $T_{cooling}$=450 ms, $T(\omega_-)$=50 ms with A(ω_-)=50 mV, $T(\omega_c)$=200 ms with A(ω_c)=1 V $p_{He} = 1.0 \times 10^{-3}$ mbar. Test was done with ionized Xe gas.

4.2 Off-Line Tests with Stable Beams from IGISOL

Further off-line tests were performed with ions produced with a spark ion source in the IGISOL chamber. The ions extracted from the gas cell were accelerated and separated by mass after which they were cooled and bunched in the RFQ trap. Thus, the beam conditions are almost identical to those with the ion guide beam produced on-line.

During the first tests we found out that there were sparks between the high voltage platform of the Penning trap and ground when running the IGISOL separator in the normal 37.5 kV HV value. These sparks caused severe damage to trap electronics especially for the TPG turbomolecular pump controller units and for the Super Tech high voltage switches used to control injection and ejection wall electrodes. Therefore IGISOL and the trap were run at lower 30 kV HV.

Due to a good quality of the beam coming out of the RFQ the first cyclotron resonance was done after 7 days of tuning and testing the trap. This

resonance is shown in figure 4.4. Regardless of the antisymmetric shape, the resonance is clearly visible since at off-resonance the number of the counts are close to zero as is should be when the magnetron exciation is done properly. The long cooling time is due to low buffer-gas pressure.

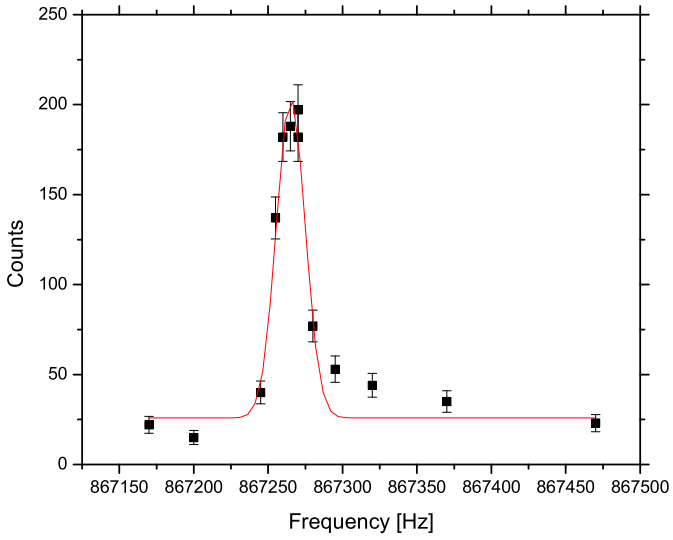

Figure 4.4: The first cyclotron excitation of $^{124}Xe^{+}$ ions produced off-line with IGISOL. (Performed 22nd of October 2002). Counts in the MCP-detector as a function of cyclotron excitation frequency. Other parameters in this case were: $T_{cooling}$=1100 ms, $T(\omega_-)$=35 ms with A(ω_-)=50 mV, f$_-$=1730 Hz, $T(\omega_c)$=300 ms with A(ω_c)=0.5 V, T(cycle)=1 550 ms, $p_{He} = 2.2 \times 10^{-3}$ mbar. Each data point includes the integral counts from 100 cycles.

Since then several resonances have been measured off-line. The shortest cycle used so far has been 120 ms, see figure 4.5. This gave the resolving power of R=$\omega_c/\Delta\omega_c$=25 000. The best mass resolution achieved so far was R=147 000 as shown in figure 4.6. The shorter the cooling time is the higher buffer-gas pressure is needed. This leads to worsened mass resolving power as seen in figures 4.5 and 4.6. Higher amliptudes can be used in shortening the excitation times, however this will also cause wider resonances.

These features, a short cycle time to make isobarically pure beams as well as the high resolving power with a longer cycle time, are essential in the real measurements. Since close to the valley of beta stability half-lifes are long but the mass difference between neighbouring nuclei are small and farther

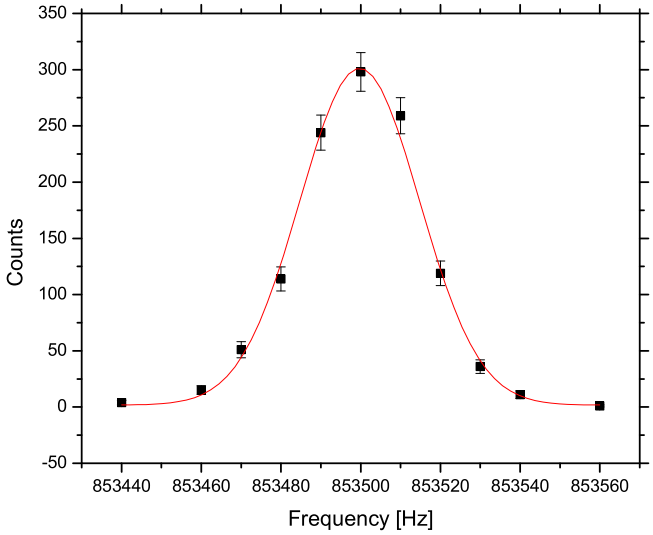

Figure 4.5: Counts in the MCP-detector as a function of cyclotron excitation frequency. The shortest cycle used so far to apply cyclotron excitation of $^{126}Xe^{+}$ ions produced off-line with IGISOL. (Performed 27th of October 2002). The mass resolving power is R=25 000. Other parameters in this case where: $T_{cooling}$=55.8 ms, $T(\omega_{-})$=5 ms with A(ω_{-})=300 mV, f$_{-}$=1718 Hz, T(ω_c)=54 ms with A(ω_c)=350 mV, T(cycle)=120 ms, $p_{He} = 9.9 \times 10^{-2}$ mbar, 100 cycles per data point.

from the stability half-lifes get shorter and the mass difference gets bigger.

We have also measured a so called "shoot-through" efficiency for the whole trap structure. This was done with two Faraday cups (table 3.2) by using a ^{129}Xe beam. The first cup is situated in the injection line where the beam has 800 eV energy and the second cup is in the ground potential where the beam has 30 keV energy, see figures 3.2 and 3.11. The Faraday cup that was placed on the ground was suppressed with a $U_{suppression} = -40$ V to prevent secondary electrons escaping from the cup. The obtained results were $I_1(cup)$=0.007 nA, $I_1(collimator)$=0.56 nA and $I_2(cup)$=0.165 nA (with -40 V suppression), $I_2(collimator)$=0.054 nA. Neglecting the collimator current of the second cup one obtains 29 % shoot-through efficiency.

The trapping efficiency was measured with the MCP detector by using $^{124}Xe^{+}$ ions. In this test the potential scheme shown earlier in figure 3.15 was used with 50 ms cycle and the integral of 1000 cycles was recorded per measurement. The result was $N_{shoot\_through}$=2.8×10^5, $N_{trapping}$=1.65×10^5, $N_{shoot\_through\_no\_beam} = 2500$. This leads to 58 % trapping efficiency.

There are several possible reasons why we loose part of the beam in the shoot-through mode. For example the injection into the trap is done at low energy through a 4 mm hole. This may amplify the effects of the emittance and the magnetic field, i.e. the velocity in the radial direction compared to axial velocity increases and due to the magnetic field the ions will have helix shaped trajectories. Another place where the losses might happen is the acceleration after the trap. Here the ions try follow the magnetic field lines and if the beam is not on the optical axis some losses will happen. However, we are not sure where the losses happen in reality.

In case of the trapping, part of the ions might be lost since when the first wall closes some ions are lifted into higher potential and some of these ions might come back through the injection wall or be lost in the trap walls.

4.3 On-line Tests with Radioactive ^{58}Cu Ions

The first test with radioactive ions was done by using the ^{58}Ni(p,n)^{58}Cu reaction with 30 MeV proton beam. This was chosen as the first test case since it would give a clean beam that contains only ^{58}Ni and ^{58}Cu ions produced in elastic collisions and in nuclear reactions, respectively. Moreover the mass difference is large enough so that it should not cause problems even if the peaks were broad. The measurement was done in such a way that each point

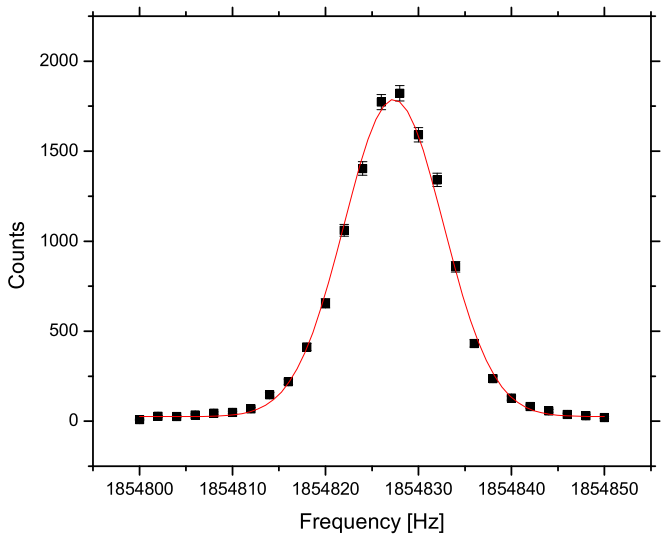

Figure 4.6: Counts in the MCP-detector as a function of cyclotron excitation frequency. The best mass resolution achieved so far with the first Penning trap has been R=147 000 as measured for $^{58}Ni^{+}$ ions. (Performed 12th of December 2002). Parameters: $T_{cooling}$=329.8 ms, $T(\omega_{-})$=15 ms with A(ω_{-})=135 mV, f$_{-}$=1725 Hz, T(ω_c)=150 ms with A(ω_c)=115 mV, T(cycle)=500 ms, $p_{He} = 1.5 \times 10^{-2}$ mbar. Each data point corresponds to 100 cycles of data taking. When the cooler was pulsed but the both walls of the Penning trap were open the observed intensity was N=5 500 in 100 cycles with CFD and N=31 000 in 100 cycles without CFD.

was measured during 100 cycles and after that the frequency was changed. The first isobaric mass purification with a radioactive beam, see figures 4.7 and 4.8 was performed on All Saints Day 2002 (1st of November 2002).

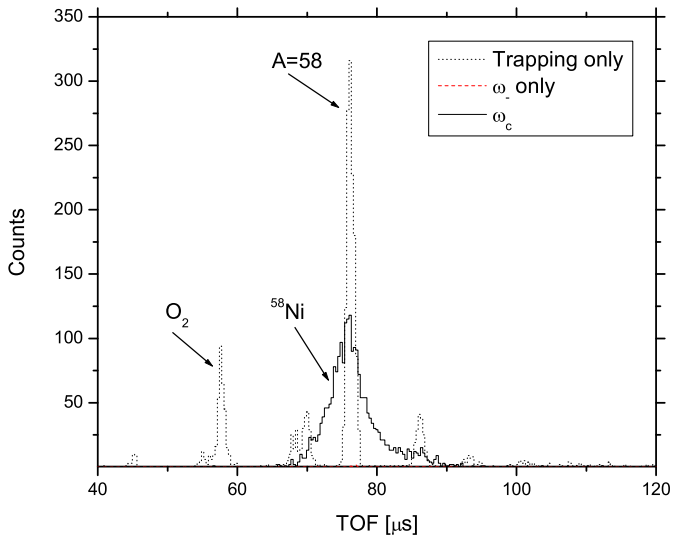

Figure 4.7: A sample spectrum recorded with the MCS for ^{58}Ni showing counts in the MCP as a function of TOF. Dotted line shows the spectrum without excitations, gray dashed line shows the spectrum after ω_- excitation (not seen properly since it is so close to zero), and solid line shows the spectrum after ω_c excitation at frequency f$_-$=1 854 825 Hz. Parameters: $T_{cooling}$=329.9 ms, $T(\omega_-)$=15 ms with A(ω_-)=130 mV, f$_-$=1718 Hz, T(ω_c)=90 ms with A(ω_c)=150 mV, T(cycle)=450 ms, $p_{He} = 4.5\times10^{-2}$ mbar, 100 cycles per data point.

Figure 4.7 shows the counts in the MCP-detector as a function of TOF. From this picture one can see how the spectrum looked with trapping only, different masses can be distinguished by the different TOF. It is also worth while to note that after the magnetron excitation the spectrum has practically no counts. The solid line shows the spectrum after the cyclotron excitation at the cyclotron frequency of ^{58}Ni and one can observe how ^{58}Ni ions are centered. This peak is broad since after the ω_c excitation ions have more energy and larger energy spread. By using extra cooling time after the

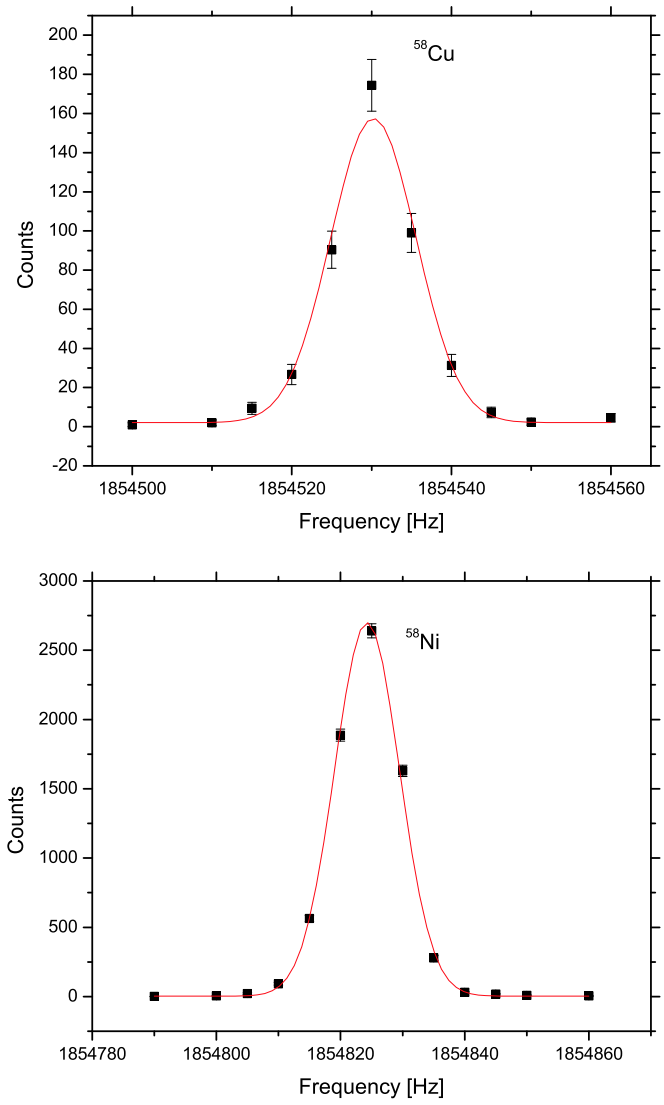

Figure 4.8: Counts in the MCP-detector as a function of cyclotron excitation frequency for ^{58}Cu and ^{58}Ni. The first successful trap test with radioactive ions (Performed 1st of November). Parameters: $T_{cooling}$=329.9 ms, $T(\omega_-)$=15 ms with A(ω_-)=130 mV, f$_-$=1718 Hz, T(ω_c)=90 ms with A(ω_c)=150 mV, T(cycle)=450 ms, $p_{He} = 4.5 \times 10^{-2}$ mbar, 100 cycles per data point. 1 Hz in this mass range corresponds to about 30 keV.

excitation this peak would become narrow again as it is in the spectrum that shows the trapping only. From the Gaussian fits in figure 4.8 one gets the information shown in table 4.1.

ΔM_{exp}	8555±8 keV
ΔM_{AME}	8563.9±1.9 keV

Table 4.1: The mass difference between ^{58}Cu and ^{58}Ni. Data from the Gaussian fits for the ^{58}Cu and ^{58}Ni resonance curves. The uncertainties shown are due to fit uncertainties.

One can see that the measured ΔM value differs by 9 keV from AME value [Aud03]. Since the masses of both isotopes ^{58}Cu and ^{58}Ni are very well known (ME is -60 227.7 (1.4) keV and -51 658.8 (2.4) keV, respectively) this deviation in ΔM values gives us a hint of the systematic uncertainty in our measurement. However, this error can also be due to beam intensity oscillation at IGISOL, since this method is dependent on the beam fluctuations. Nevertheless, this experiment proved that the first Penning trap in JYFLTRAP can do the isobaric mass purification according to the design specifications. Mass resolving power in this measurement was R$\approx 1.3 \times 10^5$. A shoot-through intensity was measured immediately after the tests: N=4000 ions in 1000 cycles of 100 ms with a 17 μs pulsing in the cooler. During the measurements count rate with trapping only was about 1600 counts per 100 cyles of 450 ms.

4.4 On-Line Experiments with Rh and Ru

The next step after the first isobaric mass separation for radioactive beams was to test the trap with fission products. In this test the first MCP detector was replaced by a thick silicon detector with a diameter d=2.5 cm. Another Si-detector with a diameter d=3.2 cm was placed at the ejection side after the pumping chamber, see figure 3.11. The first test was to measure the shoot-through efficiency with beta activity. This was done with A=112 beam. The result was 29 % (N_1=21 500 ions/10 s and N_2=6200 ions/10 s). This agrees well with the value that was measured with the suppressed Faraday cups using $^{129}Xe^+$ ions.

The trap was tested in three runs with fission products. (The first test

was performed on 16-17 of November 2002 and the others on 3-6 and 17-19 of January 2003). The aim was to produce further information of the trap functioning and possibly even new results on masses of some refractory fission products. Mass parabola for the A=112 isobar are shown in figure 4.9.

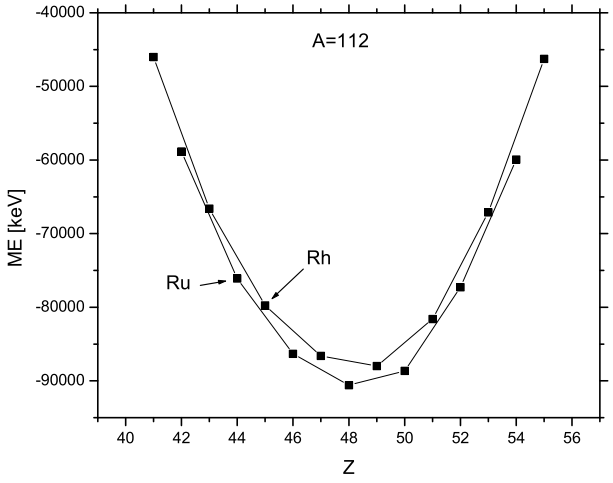

Figure 4.9: The mass parabola for A=112. Mass excess in units of keV as a function of the proton number Z. The upper curve is for the even-even nuclei and the lower one for the odd-odd nuclei.

4.4.1 Demonstration of Isobaric Purification

The first goal was to check if one can separate ^{112}Rh and ^{112}Ru isobars. This pair was chosen since one obtains good fission yields for these isotopes at the IGISOL mass separator. Normally, one uses ^{112}Rh to tune IGISOL when using a fission ion guide. Even the first test result was successful, see figure 4.10. The measurement was repeated twice during the second beam time. The results are shown in table 4.2. Later also a gamma-ray spectra were recorded, see figure 4.11. This is another way to show that isobaric purification works since after the cyclotron excitation at the cyclotron frequency of ^{112}Rh the 327 keV peak of ^{112}Ru is not visible.

Clearly, the measured mass-energy difference ΔM=3980 (30) keV differs radically from the AME value by 312 keV [Aud03] as well as by 538 keV from

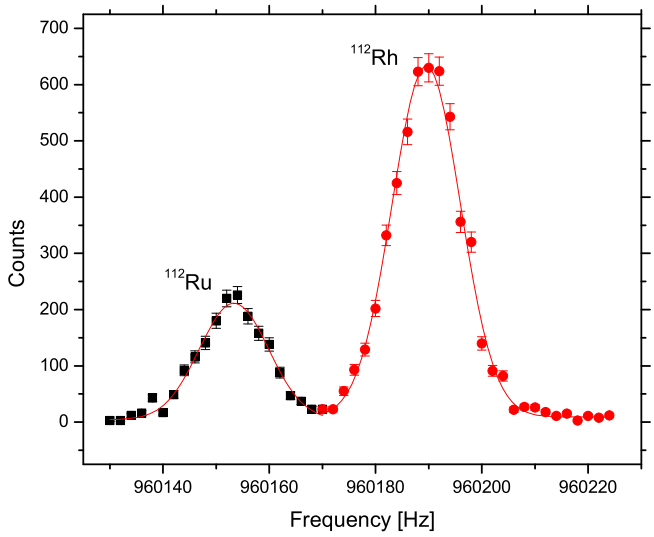

Figure 4.10: The first measurement with fission products on ^{112}Ru and ^{112}Rh. (Performed on 17th of November 2002). Showing counts in the MCP-detector as a function of cyclotron excitation frequency. Parameters: $T_{cooling}$=329.8 ms, $T(\omega_-)$=15 ms with A(ω_-)=115 mV, f$_-$=1718 Hz, T(ω_c)=90 ms with A(ω_c)=200 mV, T(cycle)=450 ms, $p_{He} = 4.5 \times 10^{-2}$ mbar, 100 cycles per data point.

	center
$\Delta M(measured\_fit)$	3979 ± 10 keV
$\Delta M(measured\_SDOM)$	3980 ± 30 keV
$\Delta M(AME)$	3670 ± 200 keV
Q_β([Jok91])	4520 ± 80 keV

Table 4.2: Results from the ^{112}Ru – ^{112}Rh measurements. The uncertainties have been obtained from the Gaussian fits and from a standard deviation of mean with an extra coefficient of 1.32 [Tay94].

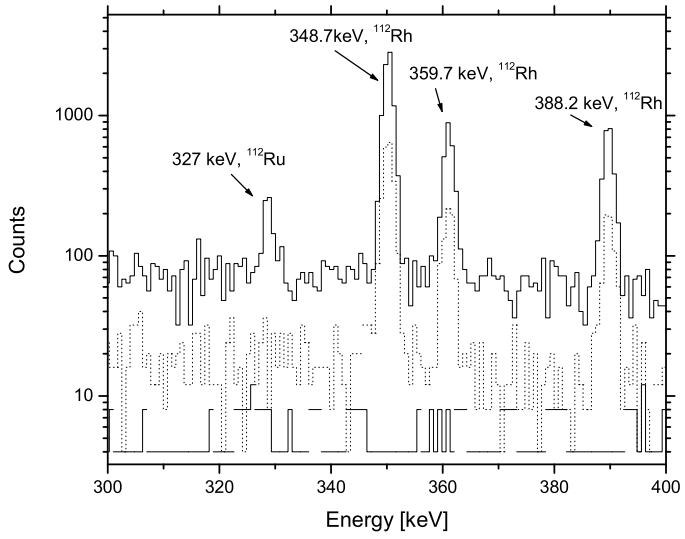

Figure 4.11: Gamma-ray spectra for ^{112}Rh. Counts as a function of gamma-ray energy in units of keV. This was measured ge-detector. Solid line: only trapping, dotted line: ω_c excitation at the cyclotron frequency of ^{112}Rh ω_c=960 189$\times 2\pi$ and lower solid line: ω_- excitation. The cycle time was 450 ms and the spectra were recorded for 60 minutes.

the β^- end-point value of [Jok91] measured earlier at IGISOL. However, the problem when comparing our value to the AME value is that due to the limited resolving power it is not known how much the ground state of ^{112}Rh and how much the isomeric state were produced.

4.4.2 Mass Measurements of Rh and Ru Isotopes

The next step was to test how stable the purification trap is, i.e. how the mass excess values vary between several measurements. This test was done with ^{112}Rh that was calibrated with ^{96}ZrO having a well-known mass. The measurement was done in two parts, the first part was performed during the night 5-6 January 2003 and took about 14 hours and the next part was performed during the night 17-18 January 2003 and took about 4 hours. The first run was done in such a way that ^{96}ZrO was measured in the beginnig as a calibration and then one of Rh or Ru isotopes followed by ^{112}Rh, and so on. At the end of the first run another calibration measurement with ^{96}ZrO was done. The second run consisted of one reference measurement with ^{96}ZrO and the measurements of ^{112}Rh, ^{114}Rh, ^{116}Rh and ^{112}Rh. The frequency scan was done in such a way that each data point was measured during several cycles before changing into the next frequency.

The results are shown in figures 4.12, 4.13 and 4.14. From nine experiments the mass excess value was calculated as a weighted mean value. Inverse squares of the uncertainties were used as weights. The procedure to calculate the mass excess values is described later in chapter 5. The result is ME(^{112}Rh)=-79480 $\pm$ 40 keV which differs 310 keV form the present AME value -79760 $\pm$ 60 keV [Aud03]. However, ^{112}Rh has an isomeric state at 360 $\pm$ 60 keV higher [Aud03], which suggests that the measured state is a combination of an isomeric and the ground state.

From figures 4.12, 4.13 one can state that the intensities have not been high in any of these measurements and since the shapes of the peaks are Gaussian the results that one obtains from the fits are considered to be reliable. The results in figure 4.14 are important since they show that the mass difference between the measured mass excess value and the AME value, or rather the frequency ratio $f_{c,ref}/f_c$, remains constant during the two runs. This implies that conditions during the measurements have been stable and no strong systematic errors have occurred during the runs.

The masses for several other rhodium an ruthenium isotopes were also measured, as shown in tables 4.3, 4.4 and 4.5 and in figures 4.15 and 4.16

they show the mass difference between the measured mass excess value and the AME value.

Nucl.	$T_{1/2}$	Scans	Cycles	N/cycle
^{110}Ru	11.6 s	1	200	702/50
^{111}Ru	2.12 s	1	150	771/50
^{112}Ru	1.75 s	2	100	1250/100
^{113}Ru	510 ms, 800ms	1	400	802/50
^{110}Rh	3.2 s, 28.5 s	1	200	702/50
^{111}Rh	11 s	1	150	771/50
^{112}Rh	6.8 s, 2.1 s	9	50, 100	-
^{113}Rh	2.80 s	1	100	802/50
^{114}Rh	1.85 s, 1.85 s	2	150	1590, 1350/100
^{115}Rh	990 ms	1	300	779/50)
^{116}Rh	570 ms, 680 ms	1	400	2200/150

Table 4.3: Results of rhodium and ruthenium test measurements. Showing the nuclide, the half life of the isomeric and the ground state, the number of scans, number of cycles per data point and counts with trapping only per cycles. The 450 ms cycle has been used in all measurements.

4.4.3 Discussion of Rhodium and Ruthenium Tests

It is important to discuss the experimental uncertainties of the current measurements. The uncertainty consists of several factors, the most important ones being the statistical uncertainty, the uncertainty due to calibration procedure as well as the systematic errors. The latter ones are not yet understood for our trap. Thus the problem has been how to make a reliable uncertainty analysis. Here all uncertainties are estimated in a conservative way, so that even if systematic uncertainties are neglected the final uncertainty should cover them.

The results were divided in two groups. The first group contains runs from 5-6 of January 2003 and the second group runs from 17-18 of January 2003. This was done to minimize the effects due to long-term changes in the magnetic field.

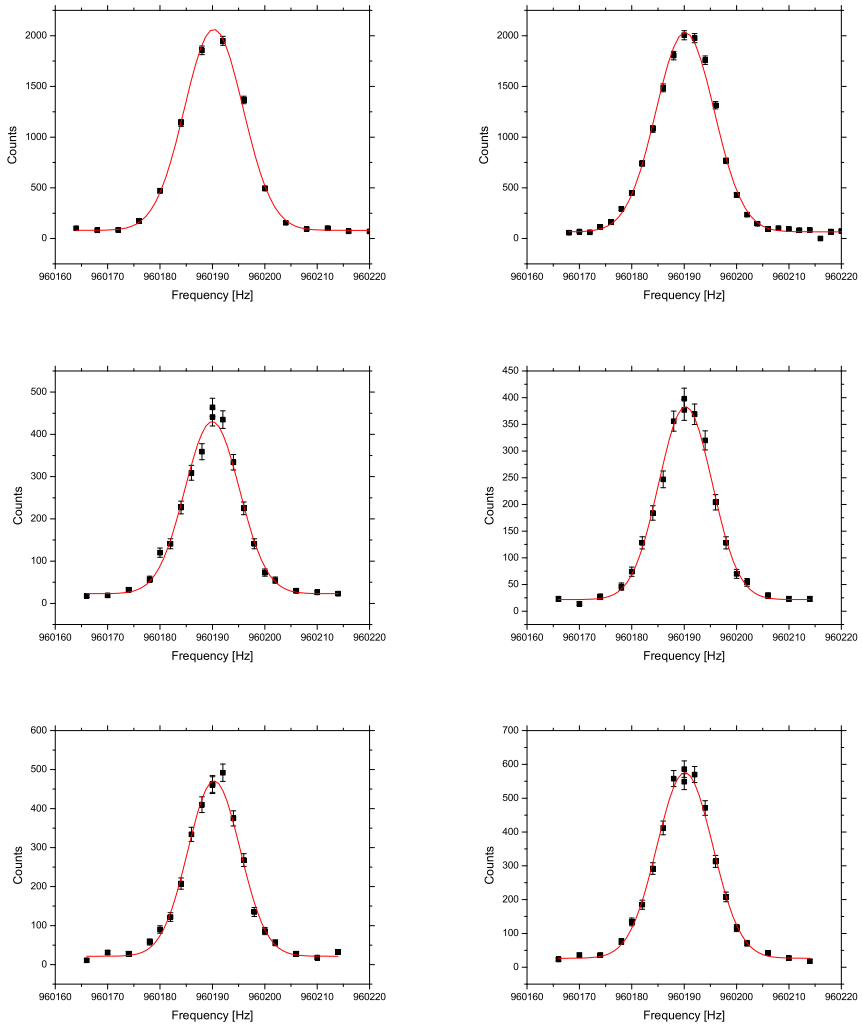

Figure 4.12: First six scans of $^{112}Rh^{+}$ of figure 4.14. Showing the counts in the MCP-detector as a function of the cyclotron excitation frequency. The 450 ms cycle has been used in all measurements. In the first two scans each data point corresponds to 100 cycles and in the scans 3-6 50 cycles. Intensities with trapping only (no excitations): 1) and 2) 1250 counts in 100 cycles, 3) 848 counts in 50 cycles, 4) 878 counts in 50 cycles, 5) 797 counts in 50 cycles and 6) 803 counts in 50 cycles.

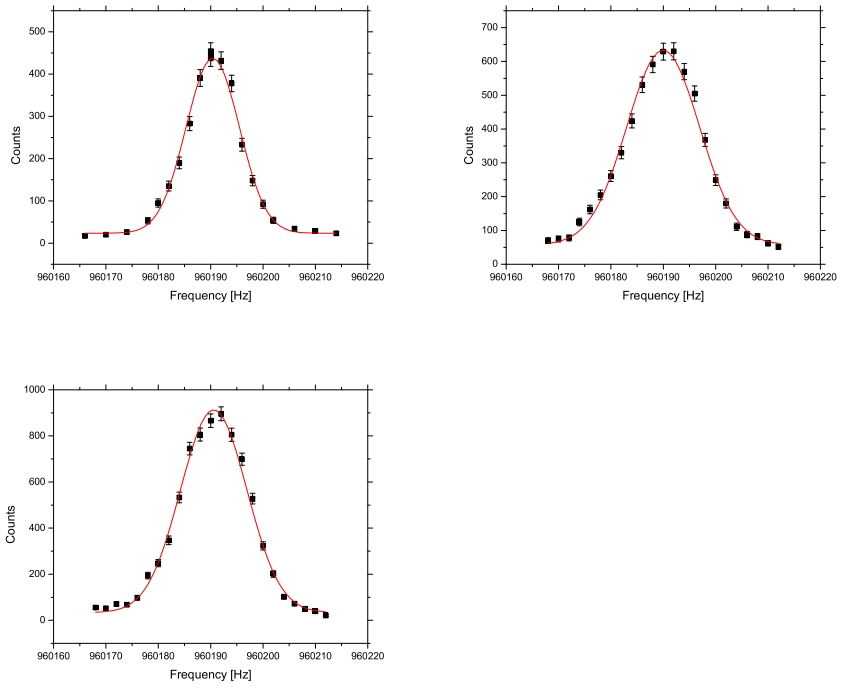

Figure 4.13: Three last scans of $^{112}Rh^{+}$ of figure 4.14. Showing the counts in the MCP-detector as a function of the cyclotron excitation frequency. The 450 ms cycle has been used in all measurements. In the first scan each data point corresponds to 50 cycles and in the two other scans each data point corresponds to 100 cycles. Intensities with trapping only (no excitations): 1) 769 counts in 50 cycles, 2) 590 counts in 50 cycles and 3) 600 counts in 50 cycles.

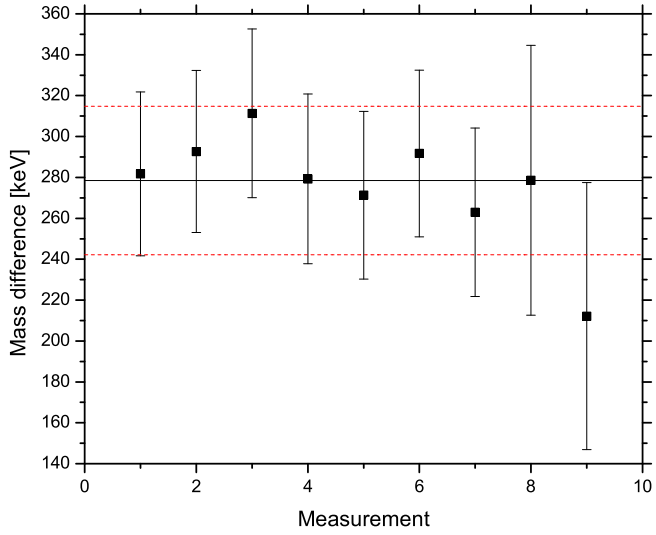

Figure 4.14: Summary of nine ^{112}Rh mass determinations. The y-axis shows the difference between the measured value and the mass excess value from AME [Aud03]. The x-axis is the number of the measurement. Solid line is the weighted average value of nine measurements and the two dashed lines show its uncertainty. The 450 ms cycle has been used in all measurements.

Nucl.	r	M (u)	u(M)/M
^{110}Ru	0.982 224 823 (702)	109.914 101 (77)	7.0×10^{-07}
^{111}Ru	0.991 193 292 (713)	110.917 696 (79)	7.1×10^{-07}
^{112}Ru	1.000 140 970 (704)	111.918 965 (79)	7.0×10^{-07}
^{113}Ru	1.009 113 696 (736)	112.923 036 (83)	7.4×10^{-07}
^{110}Rh	0.982 199 623 (702)	109.911 281 (77)	7.0×10^{-07}
^{111}Rh	0.991 139 856 (713)	110.911 717 (79)	7.1×10^{-07}
^{112}Rh part A	1.000 102 693 (378)	111.914 682 (42)	3.8×10^{-07}
^{112}Rh part B	1.000 102 188 (876)	111.914 625 (98)	8.8×10^{-07}
^{113}Rh	1.009 046 645 (736)	112.915 534 (83)	7.4×10^{-07}
^{114}Rh part A	1.018 013 157 (747)	113.918 910 (85)	7.5×10^{-07}
^{114}Rh part B	1.018 013 217 (900)	113.918 917(102)	9.0×10^{-07}
^{115}Rh	1.026 962 221 (759)	114.920 334 (87)	7.6×10^{-07}
^{116}Rh	1.035 932 829 (924)	115.924 169 (107)	9.2×10^{-07}

Table 4.4: Nuclide, the measured cyclotron resonance ratio r and its uncertainty in parenthesis, the mass value and its uncertainty in parenthesis, and the relative uncertainty.

Nucl.	ME_{exp} [keV]	ME_{AME} [keV]	ΔME [keV]
^{110}Ru	-80 010 (70)	-80 140 (110)	126
^{111}Ru	-76 670 (70)	-77 350 (70)	685
^{112}Ru	-75 480 (70)	-76 090# (210#)	607
^{113}Ru	-71 690 (80)	-72 200 (80), 130 (18)	509
^{110}Rh	-82 640 (70)	-82 950 (100), 110 (100)	309
^{111}Rh	-82 240 (70)	-82 380 (50)	145
^{112}Rh	-79 480 (40)	-79 760 (60), 360 (80)	278
^{113}Rh	-78 680 (80)	-78 680 (60)	0
^{114}Rh	-75 530 (60)	-76 100 (60), 200# (150#)	568
^{115}Rh	-74 210 (80	-73 840 (80)	-368
^{116}Rh	-70 640 (100)	-71 060# (500#), 200# (150#)	424

Table 4.5: Results of rhodium and ruthenium test measurements, showing the nuclide, the measured mass excess value, the recent AME mass excess value for the ground and the first isomeric state and the mass difference between the measured value and the AME value. The sign # means that there is no experimental data for this isotope. The AME mass excess values are taken from Nucleus 2003 [Aud03]. For some of the isotopes shown above the mass excess has been calculated by using the Q_β values measured earlier at IGISOL [Klö96] and at Mainz by using the SISAK technique [Klu93].

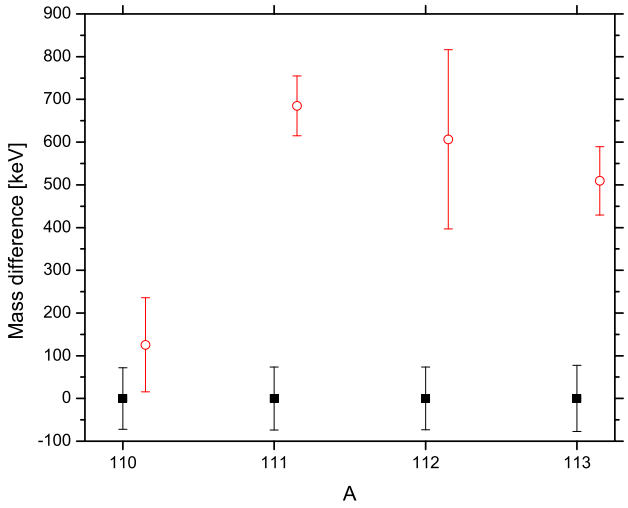

Figure 4.15: Ruthenium results of table 4.5. Mass difference M_{exp}-M_{AME} in units of keV as a function of A for Ru isotopes. The squares denote the measured values and the open circles the AME values for the ground states.

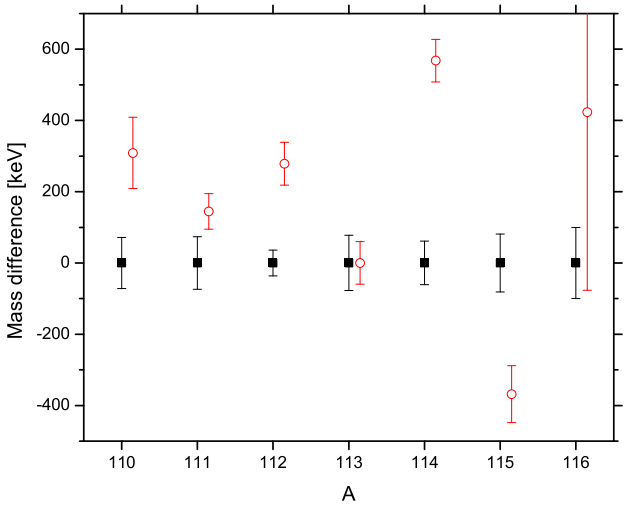

Figure 4.16: Rhodium results of table 4.5. Mass difference M_{exp}-M_{AME} in units of keV as a function of A for Rh isotopes. The squares denote the measured values and the open circles the AME values for the ground states.

In the first group the uncertainty for the frequency of ^{112}Rh (7 runs) derives directly from the standard deviation of mean (SDOM) calculation and the uncertainty for the second measurement (2 runs) comes from the SDOM multiplied by an extra coefficient of 1.84 [Tay94]. The uncertainty for ^{112}Ru and ^{114}Rh has been calculated similarly as well as that for ^{112}Rh measured in the second phase (2 runs). For all other single values we have used the uncertainty of the two ^{112}Rh measurements that were recorded during the second run. These estimations give a rather large uncertainties.

The results in figure 4.14 really demonstrate that uncertainty estimation is sufficiently coservative. There eight of nine measurements are within the uncertainty limits and only one is outside. Since normally one sigma limit means that 66 % of the results should be within the uncertainty, the uncertainty estimations used in the analysis are large enough to cover systematic uncertainties.

Later in the future after commissioning the second Penning trap, a precision trap, that is designed to do mass measurements with TOF-technique more detailed studies with systematic uncertainties can be done.

$^{110-112}$Ru

The measured mass excess -80 010 (70) keV for ^{110}Ru agrees within the uncertainties with the AME value of -80 140 (110). Instead, the mass exess value of ^{111}Ru differs by 685 keV and ^{112}Ru by 607 keV suggesting that the AME values are completely incorrect. Since these isotopes do not have known isomeric states the current measurement can be considered reliable. Instead of that isotope ^{113}Ru has an isomeric state and since we do not know which state we have been measuring we can only conclude, that the AME value is incorrect.

^{110}Rh

The measured mass of ^{110}Rh differs by 309 keV from the AME value for the ground state, i.e. -82 950 (100). Taking into account the uncertainty of our measured value ME=-82 640 (70) keV and the uncertainties of AME ground state and the isomeric state the obtained result differs by 2 to 3 times the uncertainty of the mass.

^{111}Rh

The measured mass excess of -82 240 (70) keV for ^{111}Rh differs from the AME value of -82 380 (50) by 145 keV; thus the results are rather close. Since ^{111}Rh and its parent ^{111}Ru do not have known isomeric states one can calculate the mass difference for ^{111}Ru by using the frequency ratio. The result is ΔM=5570 (90) keV while the AME value is ΔM=5040 (50) keV. the difference is huge, but that was expected since the ME value for ^{111}Ru was completely off due to the cumulative error in the decay chain.

^{112}Rh

^{112}Rh has a known isomeric state at 360 (80) keV. From the measured gamma-ray spectra, see figure 4.11, one can deduce abundances of the isomeric and the ground states. This gamma-ray spectra gives a second proof of the functionic of the purification Penning trap.

E [keV]	Area	factor	ε [%]	N(tot)
348.7	1863 (78)	638 (39)	0.84	35000 (3000)
359.7	491 (42)	222 (24)	0.82	27000 (4000)
388.2	570 (45)	214 (31)	0.76	35000 (6000)
534.6	344 (34)	209 (17)	0.57	29000 (4000)
560.5	503 (43)	357 (27)	0.54	26000 (4000)
748.1	200 (26)	201 (15)	0.42	24000 (5000)
1098.6	211 (26)	290 (15)	0.29	25000 (5000)

Table 4.6: Results of ^{112}Rh gamma-ray spectrum analysis. Energies and factors are from [Fir96].

From table 4.6 one can deduce the abundances of the ground and the isomeric state. The result is that 25 (14) % of the ^{112} Rh ions are in the ground state and 75 (13) % in the isomeric state. By using the AME values -79 760 (60) keV and -79400 (80) keV one gets that the weighted average mass excess is -79490 (70) keV. This value agrees very well with our measured value -79480 (40) keV.

This also allows us to determine the mass difference between ^{112}Ru and ^{112}Rh. In this calculation one has to use the AME mass excess value for

the ground state of ^{112}Rh and the experimental mass excess value for ^{112}Ru. Results are shown in table 4.7.

	center
^{112}Rh	-79 760 (60) keV
^{112}Ru	-75 480 (70) keV
ΔM	4280 $\pm$ 90 keV
ΔM(AME)	3670 $\pm$ 200 keV
Q_β([Jok91])	4520 $\pm$ 80 keV

Table 4.7: The mass difference between ^{112}Ru and ^{112}Rh.

$^{113-116}$Rh

The measured mass excess value of ^{113}Rh isotopes agrees well with the AME value.

Masses of ^{114}Rh disagree since even if one would sum the energy of the isomeric state and all uncertainties one would be off by 100 keV. Mass excess of ^{115}Rh disagrees clearly even if it does not have any known isomeric states. Concerning ^{116}Rh one can not make any statement due to the uncertainty in the AME ground state value and the unclear situation in case of the isomer.

Conclusions

Those isotopes that do not have known isomeric states seem to agree with our values only in the case of ^{113}Rh. In the case of ^{110}Ru and ^{111}Rh the values differ by a factor of 2 to 3 times the uncertainty and in other cases the difference is even larger. However, since in the case of ^{58}Cu and ^{58}Ni the agreement between our values and the well-known AME values was good we can state that AME masses along the decay chains containing isotopes like ^{115}Rh are most likely incorrect.

General conclusion is that AME mass excess values differ in most cases from our measured values. However, most of the AME mass values are derived form Q_β measurements and therefore they are subject to large systematic errors, due to either the incomplete knowledge of the decay scheme or the measurement technique itself.

Chapter 5

^{72}Kr Mass Measurement at ISOLTRAP

The original motivation for the mass measurement of ^{72}Kr came from the astrophysical rapid proton capture process [Oin01], [Wal81]. The rp-process takes place in explosive hydrogen burning at high temperatures $T \geq 3{\times}10^8 K$.

How far the rp-process can go depends on the temperature conditions. If the temperature $T \geq 1 \times 10^9 K$ and the density $\rho \geq 10^4\ g/cm^3$, rp-process can proceed up to Z=32 [Wor94] and beyond [Sch98]. Possible conditions exist in type I X-ray bursts [Wal81].

In the rp-process, proton capture reaction rates are orders of magnitude faster than β decay rates. Thus the reaction path follows a series of fast (p,γ) reactions until the further proton capture is inhibited. In such a situation the rapid proton capture process stops and it has to wait for the slow β decay. This kind of nucleus where the proton capture is inhibited is called a waiting point nucleus. ^{72}Kr is a waiting point nucleus since its one proton capture daughter ^{73}Rb is unbound [Moh91], [Jok96]. In this situation the process has to wait for the β decay or go further via a two proton capture [Sch98]. If this kind of two proton capture is possible, i.e. if the unbound daughter lives long enough to capture a second proton, the waiting time will be reduced significantly.

The proton capture rate is not only dependent on temperature and density conditions but also strongly on the proton capture Q value, i.e. the mass of the parent and daughter nuclei [Sch98]. Thus, it is clear that the reliability of the rp-process calculation depends on how accurately the masses along the rp-process path are known. A possible rp-process path in the vicinity of

^{72}Kr is shown in figure 5.1.

For improving the knowledge of the rp-process path in this particular area the step is to measure the mass of ^{72}Kr. The next step would be to measure the 2p-capture associated isotopes ^{73}Rb and ^{74}Sr. In the following the mass measurement of ^{72}Kr, performed at ISOLDE, CERN, is presented.

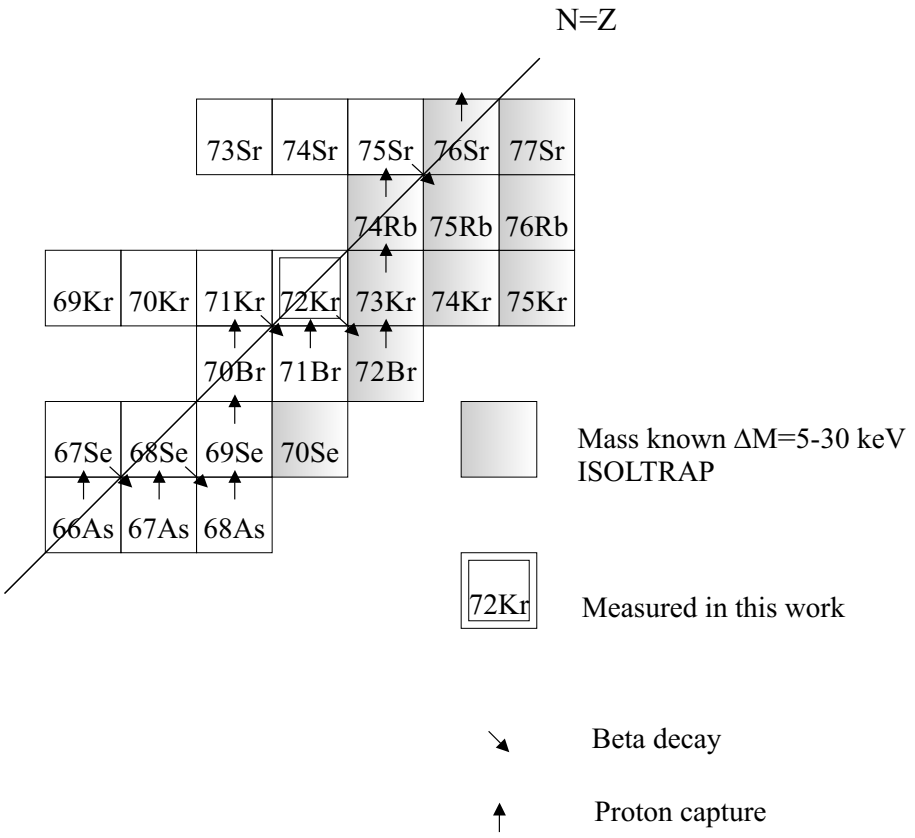

Figure 5.1: Part of the nuclide chart showing ^{72}Kr and a possible rp-path [Sch98]. Gray shaded squares show the nuclides whose masses have been measured earlier at ISOLTRAP [Her02].

5.1 ISOLDE

The ISOLTRAP mass spectrometer [Bol96] is located at the ISOLDE facility [Kug00] of CERN. The ISOL technique is used to produce low energy

radioactive beams by using spallation, fission and fragmentation reactions. At ISOLDE the primary beam is obtained from the Proton Synchrotron Booster (PSB in figure 5.2) that produces a pulsed 1.0 or 1.4 GeV proton beam at repetition rate of 1.2 s. This proton beam hits a thick target and the reaction products are stopped inside the target itself where they are extracted by heating the target to very high temperature. Diffusing radioactive atoms are then ionized by using laser ionization, by surface ionization, or by hot plasma ionization. The secondary beam is then accelerated to 60 kV and mass separated in one of two mass separators GPS or HRS that have mass resolving powers of R=2400 and R=7000-15000, respectively. These radioactive beams are then transported to several nuclear and material physics experiments.

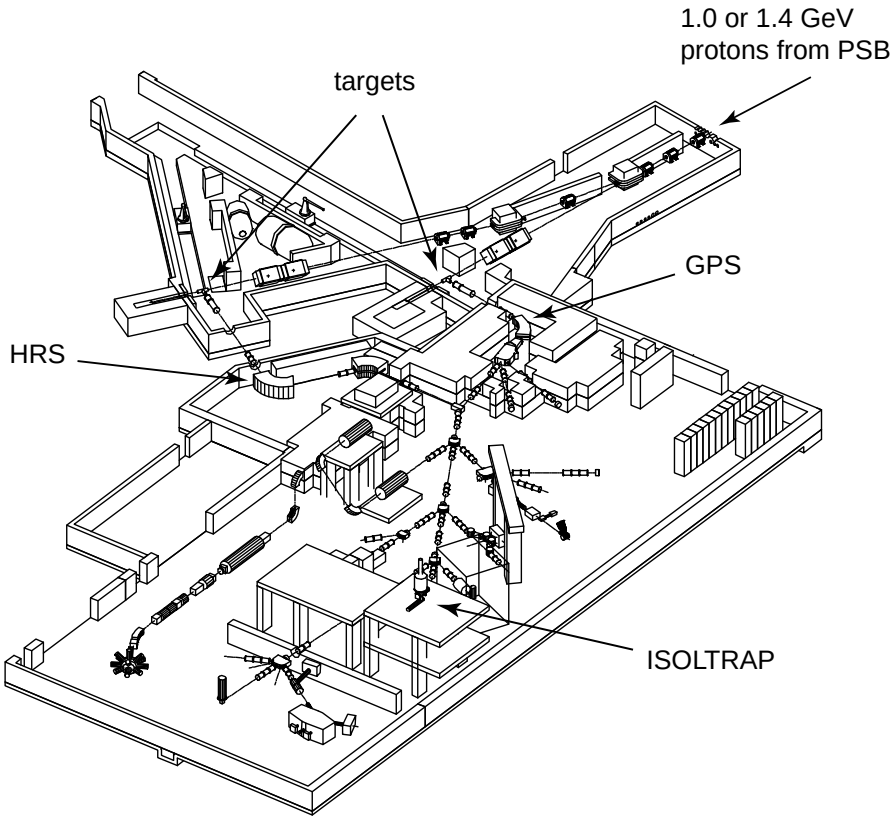

Figure 5.2: Overview of the ISOLDE hall at CERN.

5.2 ISOLTRAP Experiment

The ISOLTRAP system is a triple trap that consists of an RFQ cooler/buncher [Her01], a cylindrical purification trap [Rai97] and a hyperbolic precision trap [Bol96], see figure 5.3.

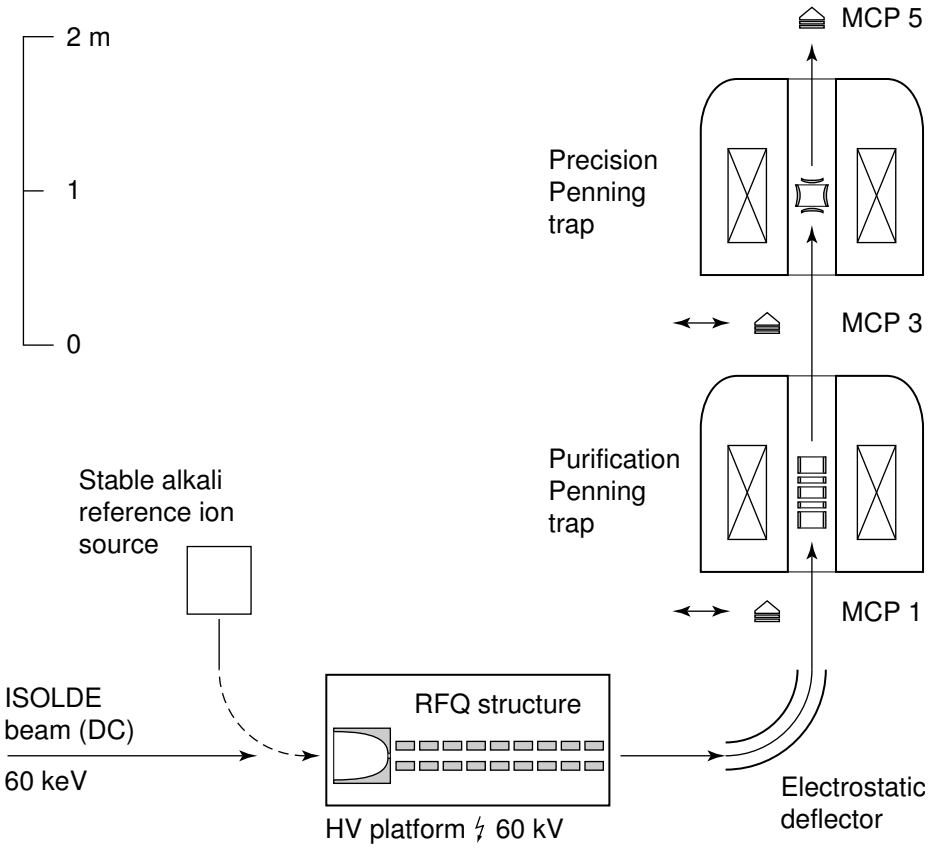

Figure 5.3: ISOLTRAP set up. The system consists of RFQ cooler/buncher, purification Penning trap and precision Penning trap. MCP5 is used to measure the TOF cyclotron resonance curve and the other MCPs are used in setting up and tuning the system. Off-line alkali ion source is used in reference measurements.

The 60 keV ISOLDE beam that has an energy spread of a few eV and an emittance of 35π mm mrad is decelerated to $E = 20$ eV and injected into the RFQ cooler/buncher where ions are cooled by collisions with the buffer gas atoms. Ions are extracted in bunches into a pulsed cavity that

is initially raised to 57.2 kV potential. While the ion bunch traverses the cavity its potential is switched to the ground level 0 V potential; thus the ions have 2.8 keV energy when coming out of the high voltage platform. The total efficiency for this device is 10-15 % , the length of the pulse is 10 μs and the estimated emittance is 10π mm mrad for the 2.8 keV beam. This corresponds to 2π mm mrad for the 60 keV beam [Her01].

The beam bunch coming out from the cavity is guided into the buffer gas filled cylindrical purification Penning trap that uses a dynamic trapping scheme. This trap has been placed in the 4.7 T superconducting magnet and the trap structure itself consists of 13 cylindrical segments. The buffer gas pressure for He is typically 1×10^{-5} mbar, trapping times are typically $\approx 200 - 500$ ms and the resolving power with long trapping times has been measured to be $R = 10^5$ [Rai97].

After the isobaric mass purification ejected ions are transferred to the precision trap placed inside a 5.9 T superconducting magnet. This trap is operated in vacuum at $p = 1 \times 10^{-8}$ mbar pressure and is used for mass measurements by using the time of flight technique as explained in the chapter 2.5.4.

5.3 Principle of Measurement

TOF method is based on the cyclotron excitation in the precision trap. However, even if the cyclotron resonance measurement combined with TOF technique is a direct way to measure masses, one needs to calibrate the mass frequency relation. This is done by making a reference measurement just before and after the measurement of ion species of interest. These reference measurements are done by using an isotope that has a well known mass; however even then the uncertainty of the reference mass will contribute to the uncertainty of the ion mass of interest. Thus, one always measures the ratio between the reference frequency $f_{ref,c}$ and the measured frequency f_c

$$r = \frac{f_{c,ref}}{f_c}. \tag{5.1}$$

From these relations one can calculate the atomic mass of interest m, by using the atomic mass of the reference ion m_{ref} and the electron mass m_e,

$$m = r(m_{ref} - m_e) + m_e. \tag{5.2}$$

In this run $^{85}Rb^{+}$ ions were used as a reference ion [Bra99]. The reference frequency is interpolated from the linear least-square fit of two data points as follows:

$$f_{c,ref}(t) = t\frac{f_2 - f_1}{t_2 - t_1} + \frac{t_2 f_1 - t_1 f_2}{t_2 - t_1}. \tag{5.3}$$

Its error can be derived by differentiating this formula,

$$\sigma(f_{c,ref}) = \sqrt{\frac{1}{(t_2 - t_1)^2}[t_1^2\sigma_2^2 + t_2^2\sigma_1^2 - 2t(t_1\sigma_2^2 + t_2\sigma_1^2) + t^2(\sigma_1^2 + \sigma_2^2)]} \tag{5.4}$$

where f_1 is the frequency of the reference measurement before and f_2 is the reference frequency after and σ_1 and σ_2 are the errors, respectively. Time t is the time when the measurement is done and t_1 time for the first reference measurement and t_2 time for the second reference measurement.

It is obvious [Kel02] that also the fluctuations in the magnetic field have to be taken into account in the error of the reference frequency:

$$\left(\frac{\sigma_{ref}(f_{c,ref})}{f_{c,ref}}\right)^2 = \left(\frac{\sigma(f_{c,ref})}{f_{c,ref}}\right)^2 + \left(\frac{\sigma_B(f_{c,ref})}{f_{c,ref}}\right)^2 \tag{5.5}$$

where

$$\frac{\sigma_B(f_{c,ref})}{f_{c,ref}} = 6.35 \times 10^{-11}\Delta T. \tag{5.6}$$

This is an empirical relation for ISOLTRAP. Here ΔT is time in minutes between (the centres of) the two reference measurements.

Now the error for the frequency ratio r is calculated in the following way

$$\left(\frac{\sigma_r}{r}\right)^2 = \left(\frac{\sigma_{ref}(f_{c,ref})}{r}\right)^2 + \left(\frac{\sigma(f_c)}{r}\right)^2. \tag{5.7}$$

Where $\sigma(f_c)$ is the uncertainty related to the measurement of the ion of interest. Since the measurement is normally repeated few times the weighted mean value for r and its uncertainty σ_r is calculated by using the inverse square of the uncertainty as a weight. Thus

$$\bar{r} = \frac{\sum_i r_i(1/\sigma_{ri})^2}{\sum_i(1/\sigma_{ri})^2} \tag{5.8}$$

and

$$\bar{\sigma} = \frac{1}{\sum_i(1/\sigma_{ri})^2}. \tag{5.9}$$

Finally, after calculating the mean value and its uncertainty, one still needs to take into account a mass-dependent devation σ_m [Bla02], [Kel01] and deviation due to unknown effects σ_u [Bec97], [Kel01]. Thus

$$\left(\frac{\bar{\sigma}_{final}}{\bar{r}}\right)^2 = \left(\frac{\bar{\sigma}}{\bar{r}}\right)^2 + \left(\frac{\sigma_m}{\bar{r}}\right)^2 + \left(\frac{\sigma_u}{\bar{r}}\right)^2 \tag{5.10}$$

where for ISOLTRAP,

$$\sigma_m/\bar{r} = 1.6 \times 10^{-10} \Delta M/u, \tag{5.11}$$

$$\sigma_u/\bar{r} = 8 \times 10^{-9}. \tag{5.12}$$

5.4 Results

The data analysed and presented here was taken in September 2001. In this run a 1.4 GeV proton beam and ZrO target were used in HRS. The reference measurements were done with stable $^{85}Rb^+$ ions produced by the ISOLTRAP reference ion source and they were done just before and after the measurement of the ion of interest (or every second measurement in case of short runs). The total efficiency for the ISOLTRAP system at the beginning of the run was 3×10^{-3}.

The aim was to measure the mass of ^{72}Kr and check the masses for some other Kr isotopes to be sure that we are measuring correctly. The results are shown in tables 5.1, 5.2 and 5.3 and in figures 5.4 and 5.5. These figures show the mass difference between the measured mass excess value and the AME value.

The values used in the analysis were m_e=510.998 902(21) keV [Moh99], 1 u=931 494.0090(71) keV [Aud01] and $M(^{85}Rb)$=84.911 798 738(12) u [Bra99] [Kel02].

The mass excess values given in table 5.3 are calculated by the relation:

$$ME = m - A \tag{5.13}$$

where m is the mass of an atom in atomic mass units and A is the atomic mass number. This value is then converted into units of keV.

Nucl.	$T_{1/2}$	Scans	N_{fits}
^{72}Kr	17.2 s	1	452
^{73}Kr	28.6 s	1	2857
^{74}Kr	11.5 min	1	21 616
^{78}Kr	stable	6	44 054
^{86}Kr	stable	3	12 759

Table 5.1: Nuclide, half life [Aud97], the number of scans and the total number of ions used in the fits.

Nucl.	r	M (u)	u(M)/M
^{72}Kr	0.847 255 826 (109)	71.942 092 32 (786)	1.1×10^{-07}
^{73}Kr	0.858 999 798 (131)	72.939 287 55 (955)	1.3×10^{-07}
^{74}Kr	0.870 703 6793 (512)	73.933 078 67 (379)	5.1×10^{-08}
^{78}Kr	0.917 661 9408 (298)	77.920 362 94 (232)	3.0×10^{-08}
^{86}Kr	1.011 763 1171 (275)	85.910 610 61 (275)	2.8×10^{-08}

Table 5.2: Nuclide, the measured cyclotron resonance ratio r and its uncertainty in parenthesis, the mass value and its uncertainty in parenthesis, and the relative uncertainty. All values have been calculated as shown in the previous section.

Nucl.	ME$_{exp}$ [keV]	ME$_{AME}$ [keV]	ME$_{exp}$-ME$_{AME}$ [keV]
^{72}Kr	-53940.7 (7.3)	-54100 (300)	159.3
^{73}Kr	-56553.3 (8.9)	-56550.8 (9.0)	-2.5
^{74}Kr	-62336.8 (3.5)	-62330.3 (2.4)	-6.5
^{78}Kr	-74181.4 (2.2)	-74178.1 (1.2)	-3.3
^{86}Kr	-83265.7 (2.2)	-83265.9 (1.1)	0.2

Table 5.3: Nuclide, the measured mass excess and its uncertainty, the mass excess from literature and its uncertainty, and the difference between the literature and the measured mass excess values. In the case of ^{72}Kr and ^{86}Kr the $ME(AME)$ values are from the AME95 Tables [Aud95] and in the case of ^{73}Kr, ^{74}Kr ^{78}Kr the values are from the later evaluation [Kel02].

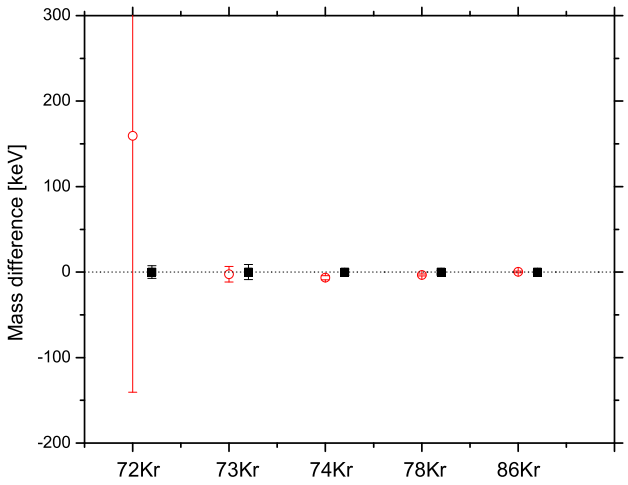

Figure 5.4: Data from Table 5.3. Mass difference M_{exp}-M_{AME} in units of keV as a function of A for Kr isotopes. The filled squares are the measured values and the open circles are the AME values.

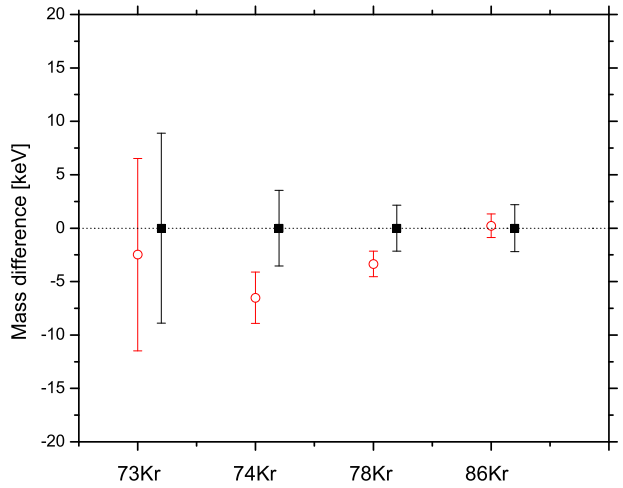

Figure 5.5: Data from Table 5.3. Mass difference M_{exp}-M_{AME} in units of keV as a function of A for Kr isotopes. The filled squares are the measured values and the open circles are the AME values.

5.4.1 Discussion of Results

^{86}Kr

The measured mass excess value for ^{86}Kr, -83265.7 (2.2) keV, agrees very well with the AME value -83265.9 (11) keV [Aud93], [Aud95] and with the more accurate SMILETRAP [Car97] value -83265.57 (1.1) [Fri02].

^{78}Kr

For ^{78}Kr the measured result ME_{exp}=-74181.4 (2.2) differs from the AME value -74178.1 (1.2) keV. This AME value has got 91 % of its value from the earlier ISOLTRAP measurements ME=-74179.2 (1.3) keV [Kel02]. This is already closer to the measured value, but still differs from that by one σ.

^{74}Kr

The difference in case of ^{74}Kr is 2 standard deviations. The measured mass excess is ME_{exp}=-62336.8 (3.5) keV and the AME value is ME_{AME}=-62330.3 (2.4) keV. The difference is 6.5 keV and is significant since the recent AME value is completely determined from previous ISOLTRAP measurements [Kel02].

^{73}Kr

The agreement between the measured mass excess value ME_{exp}=-56553.3 (8.9) keV and the ME_{AME}=-56550.8 (9.0) keV is good. This AME value is also completely determined by the previous ISOLTRAP measurements [Kel02].

^{72}Kr

The difference between the measured value ME_{exp}=-53940.7 (7.3) keV and the literature value ME_{AME}= -54100 (300) keV [Aud95] is rather big, 160 keV. However the new and the old value value agree taking into account the uncertainty of the old value.

Chapter 6

Summary and Conclusions

In this work a double cylindrical Penning trap system for low energy ion beams has been built and tested at IGISOL at the Department of Physics, University of Jyväskylä. The purpose of this trap system is to accept the bunched beam from the RFQ cooler/buncher and to purify it by mass and further deliver the beam to spectroscopy set-ups or to the second Penning trap that will be used in precise mass measurements. The advantage of isobarically pure beams will be determined when one carries out spectroscopy experiments far from stability. In these kind of experiments unwanted ions can be orders of more abundant than the wanted rare ions. Isobaric contaminants can be removed with the Penning trap and the wanted activity can be measured with high sensitivity since the peak to background ratio is improved.

During the test it was found out that the shoot-through efficiency for the double trap system is 29 % and the trapping efficiency is 58 % leading to 17 % total efficiency.

The capability to make isobaric mass purifications for radioactive beams has been demonstrated first with ^{58}Cu and ^{58}Ni and later with ^{112}Ru and ^{112}Rh ions and some other n-rich isotopes. Typically, the total cycle time for the trap was 450 ms. This includes time for the axial cooling, for the magnetron excitation in the dipole mode and for the cyclotron excitation in the quadrupole mode. The best resolving power R=147 000 was achieved with a ^{58}Ni beam and the shortest cycle used was 120 ms which lead to R=25 000 for ^{126}Xe ions.

It is clear that the implemented trap system will provide an excellent tool to make new physics in the near future. For example the accurate masses of

refractory elements like Ru and Rh, are poorly known. Already the present test experiments show that the recent AME values seem to deviate significantly from the directly measured mass values. The problem is that most of the mass values in this region are based on beta end-point measurements that may contain large systematic errors. It is clear that since IGISOL offers an excellent method to produce these refractory elements in fission several new mass measurements will be done in this region during next years after the precision Penning trap has been commissioned. The second region of interest might be the proton rich side of the nuclide chart in the vicinity of Zr and Y. These isotopes can be produced with heavy-ion fusion evaporation reactions [Den98]. Special interest in the mass measurements in this area lies in studying the rapid proton capture path.

In the near future several improvements and new developments are expected including putting the precision trap into operation, improving the gas feeding system of the purification trap, improving the ejection beam line and later building a carbon cluster reference ion source.

Appendix A

Cooling and Emittance

A.1 Cooling

An ion position and velocity are described according to Hamiltonian formalism in six dimensional (x, y, z, p_x, p_y, p_z)- phase space. According to the Liouvilles theorem the volume of $\Delta\Gamma = \Delta x\Delta y\Delta z\Delta p_x\Delta p_y\Delta p_z$ will remain constant in the presence of conservative forces [Mar88]. For a conservative force it is always possible to find a potential function like for the electric field or the magnetic field used in a Penning trap. The friction force created by the buffer gas molecules is a non-conservative force and thus the volume of phase space is no longer a constant. Cooling means decreasing of $\Delta x\Delta y\Delta z\Delta p_x\Delta p_y\Delta p_z$. Overview of other cooling methods can be found in the reference [Ita95].

A.2 Emittance

Cooling could be associated also to temperature by using statistical mechanics. However, this is not at all useful quantity for ion beams and thus a more suitable emittance quantity has to be taken into use. To understand the concept of emittance one must look at the two dimensional (u, p_u) projections of the phase space where u stands for any of the coordinates x,y or z. These kind of cuts are called action diagrams. The emittance of the beam is defined as the area of an action diagram divided by the central momentum p_0 of the reference particle travelling along the optical axis. According to figure A.1 emittance $\xi = \Delta x\Delta\theta$ where $\Delta\theta = \frac{\Delta p_x}{p_0}$ i.e. the divergence angle. Usually

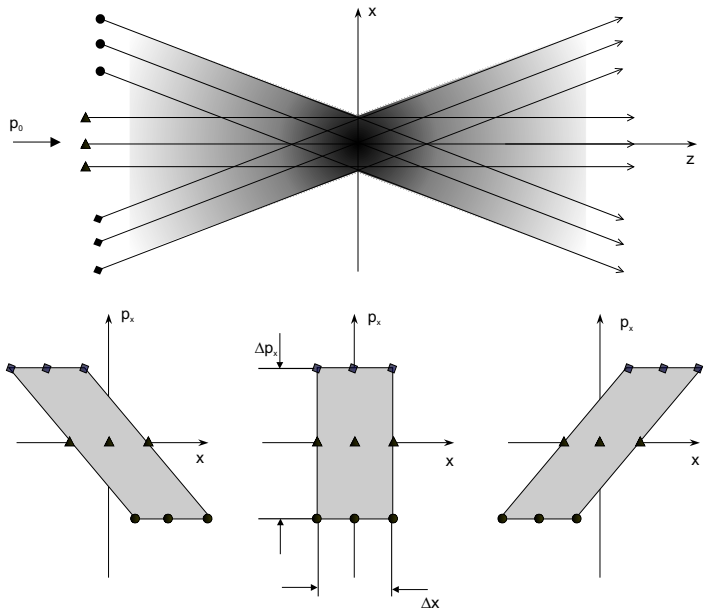

Figure A.1: Examples of action diagrams. Projection in x-z-plane. The optical axis for the beam is the z-axis. At left converging beam, at center beam at focus, at right diverging beam.

emittance is given in mm mrad units. However, normally an action diagram of the beam is not a square as in figure A.1 but an ellipse.

Appendix B

Cabling

All wires to trap electrodes inside the vacuum are connected via the plug chambers. The cables are connected according to the following tables.

Electrode	Pin	In controls
X1 left	B	1
X1 right	A	GND
Y1 up	E	GND
Y1 down	F	2
X2 left	D	3
X2 right	C	GND
Y2 up	G	GND
Y2 down	H	4

Table B.1: Cabling of the RFQ xy-deflector. Connections in the ten pin plug. The Einzel lens after the RFQ has been connected to a separate pin plug.

Electrode	Pin
Chamber	A
Lens	B
Extraction	C
Frame	I
Current1	D
Current2	J
Current common	E

Table B.2: Cabling of the test ion source. Connections in the ten pin plug.

Electrode	Pin	In controls
X1 left	F	1
X1 right	C	GND
Y1 up	E	GND
Y1 down	D	2
X2 left	G	3
X2 right	B	GND
Y2 up	A	GND
Y2 down	H	4

Table B.3: Cabling of the trap xy-deflector. Connections in the ten pin plug.

Electrode	Pin
Deceleration 1	D
Deceleration 2	B
Deceleration 3	A

Table B.4: Cabling of the deceleration electrodes. Connected into four pin plug.

Electrode	Plug
Trap 1-3, shorted	T2J
Trap 4	T2H
Trap 5	T2I
Trap 6	T2B
Trap 7	T2A
Trap 8	T1B
Trap 9	T1D
Trap 10	T1C
Trap 11	T2E
Trap 12	T3A
Trap 13,	T1E
Trap 14, End cap	TIJ
Trap 15, End cap	T2C
Trap 16, End cap	T3D
Trap 17, Correction 2	T1F
Trap 18 A, Correction 1	T3F
Trap 18 B, Correction 1	T1H
Trap 19 A, Segmented Ring	T2F
Trap 19 B, Segmented Ring	T2D
Trap 19 C, Segmented Ring	T3H
Trap 19 D, Segmented Ring	T3B
Trap 19 E, Segmented Ring	T3E
Trap 19 F, Segmented Ring	T1I
Trap 19 G, Segmented Ring	T1A
Trap 19 H, Segmented Ring	T2G
Trap 20 A, Correction 1	T3I
Trap 20 B, Correction 1	T1G
Trap 21, Correction 2	T3G
Trap 22, End cap	T3J
Trap 23, End cap	T3C

Table B.5: Electrical connections between the trap electrodes and the plugs at the injection side

Electrode	Plug
Trap 24, 2mm diaph.	T4F
Trap 25, 2mm diaph.	T5A
Trap 26, End cap,	T5B
Trap 27, End cap,	T5C
Trap 28 Correction 2	T5H
Trap 29 A, Correction 1	T6H
Trap 29 B, Correction 1	T4H
Trap 30 A, Segmented Ring	T5F
Trap 30 B, Segmented Ring	T6B
Trap 30 C, Segmented Ring	T6G
Trap 30 D, Segmented Ring	T6J
Trap 30 E, Segmented Ring	T4B
Trap 30 F, Segmented Ring	T4I
Trap 30 G, Segmented Ring	T5D
Trap 30 H, Segmented Ring	T5G
Trap 31 A, Correction 1	T6A
Trap 31 B, Correction 1	T4A
Trap 32, Correction 2	T4G
Trap 33, End cap	T5E
Trap 34, End cap	T6C
Trap 35, End cap	T4C
Trap 36,	T6E
Trap 37,	T4D
Trap 38,	T6F

Table B.6: Electrical connection between the trap electrodes and the plugs at the extraction side.

Electrode	Plug
Plug	T4E
Shield 1	T5J
Acceleration 1	T4J
Shield 2	T6D
Acceleration 2	not in the plug

Table B.7: Connection of the plug electrode and the acceleration electrodes.

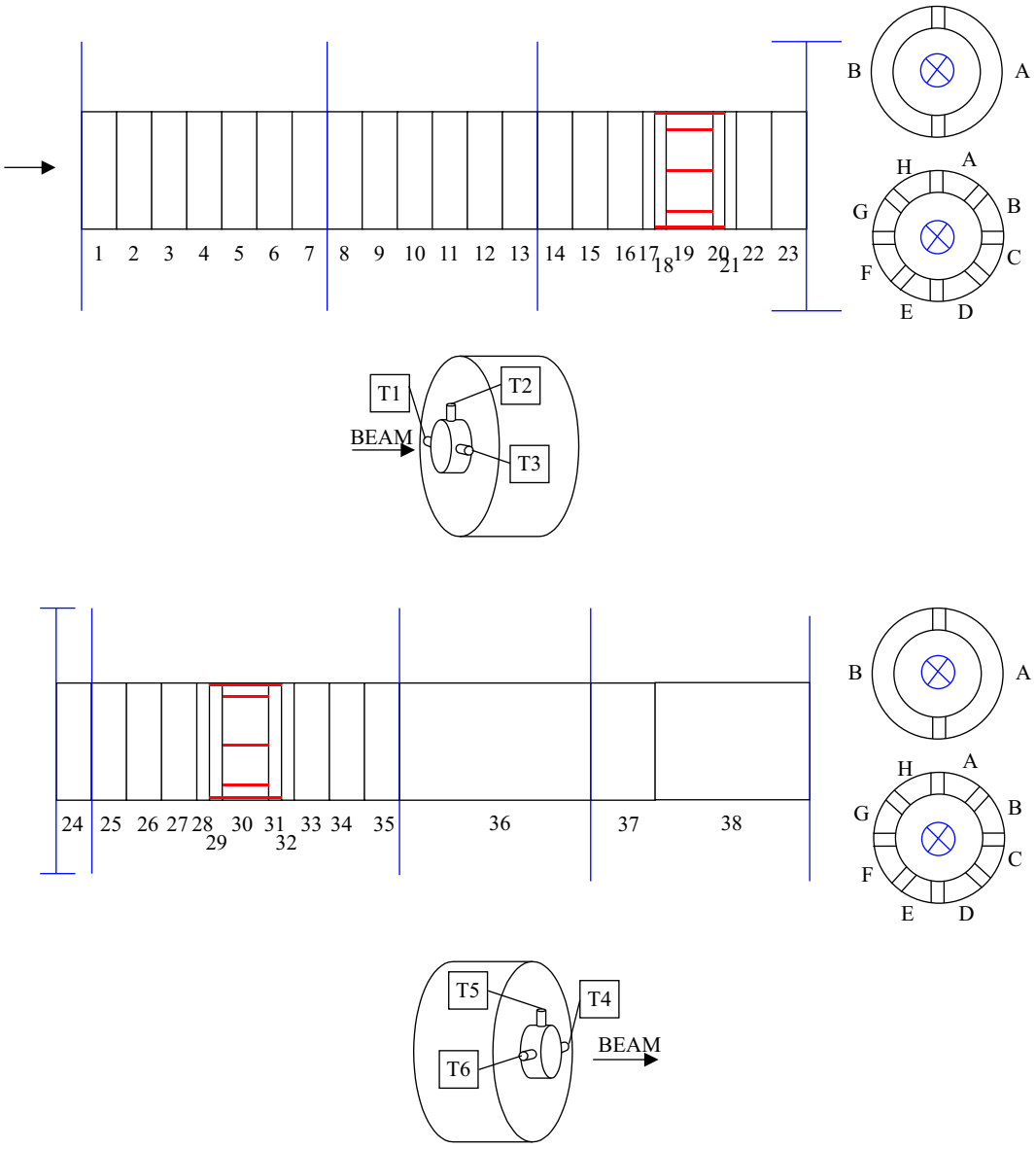

Figure B.1: Electrical connections between the trap electrodes and the plugs.

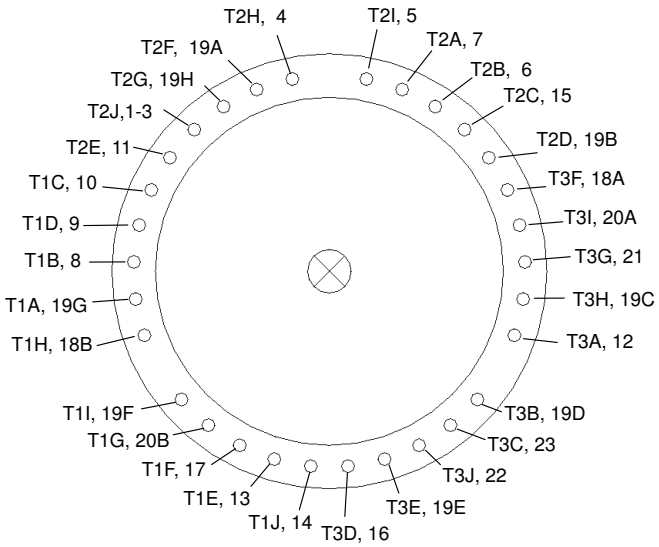

Figure B.2: Electrical connections between the trap electrodes and the pins at the injection side of the trap structure. The pins go into the sockets that are connected into the plugs.

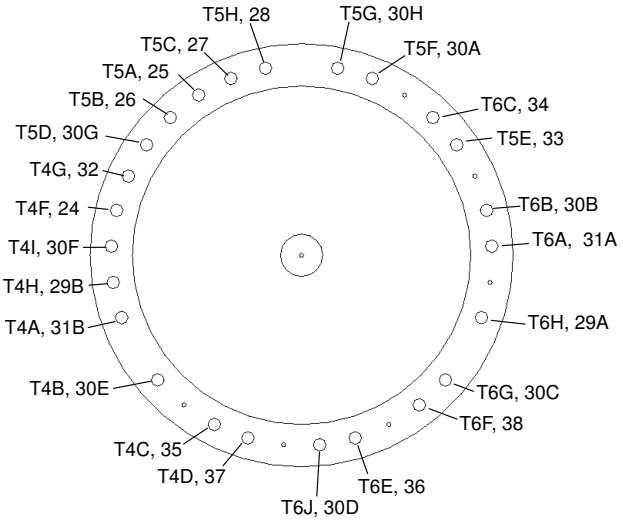

Figure B.3: Electrical connections between the trap electrodes and the pins at the ejection side of the trap structure. The pins go into the sockets that are connected into the plugs.

Electrode	Pin
X right	D
X left	I
Y down	A
Y up	B
Grid	J

Table B.8: Cabling of the xy-deflector and the grid in ground.

Bibliography

[Aud93] G. Audi, A.H. Wapstra, Nucl. Phys. A**565** (1993) 1

[Aud95] G. Audi, A.H. Wapstra, Nucl. Phys. A**595** (1995) 409

[Aud97] G. Audi, O. Bersilon, J. Blachot, A.H. Wapstra, Nucl. Phys. A **624** (1997) 1

[Aud01] G. Audi, Hyp. Int. **132** (2001) 7

[Aud03] G. Audi et al., NUBASE evaluation, http://csnwww.in2p3.fr/AMDC/, 2003.

[Aug94] G. Auger et al., Nucl. Instrum. Methods Phys. Res. A **350** (1994) 235

[Ärj81] J. Ärje, J. Äystö, J. Honkanen, K. Valli, Nucl. Instrum. Methods **186** (1981) 149

[Ärj85] J. Ärje, J. Äystö, H. Hyvönen, P. Taskinen, V. Koponen, J. Honkanen, A. Hautojärvi, K. Vierinen, Phys. Rev. Lett. **54** (1985) 99

[Ärj86] J. Ärje et. al., Nucl. Instrum. Meth. A **247** (1986) 431

[Äys88] J. Äystö et al. Nucl. Phys. A **480** (1988) 104

[Äys01] J. Äystö, Nucl. Phys. A **693** (2001) 477

[Bec97] D. Beck et al., Nucl. Instr. and Meth. B **126** (1997) 374

[Bla02] K. Blaum et al., Eur. Phys. J. A **15** (2002) 245

[Blo53] F. Bloch, Physica **19** (1953) 821

[Bol90] G. Bollen, R.B. More, G. Savard, H. Stolzenberg, J. Appl. Phys. **68** (1990) 4355

[Bol96] G. Bollen et al., Nucl. Instrum. Meth. A **368** (1996) 675

[Bol02] G. Bollen, Eur. Phys. J. A **15** (2002) 237

[Bra99] M. Bradley, J. V. Porto, S. Rainville, J. K. Thompson, D. E. Pritchard, Phys. Rev. Lett. **83** (1999) 4510

[Bro86] L.S. Brown and G. Gabrielse, Reviews of Modern Physics **58(1)** (1986) 233

[CAN] http://www.can-cia.de

[Car97] C. Carlberg, H. Borgenstrand, T. Johansson, R. Schuch, I. Bergström, G. Rouleau, J. Stein, U. Surkau, Phys. Scr. **T73** (1997) 347

[Daw76] P. H. Dawson (Ed.), Quadrupole Mass Spectrometry and Its Applications, Elsevier, Amsterdam (1976)

[Deh67] H.G. Dehmelt, Adv. in Mol. and At. Phys. **3** (1967) 53

[Deh69] H.G. Dehmelt, Adv. in Mol. and At. Phys. **5** (1969) 109

[Den98] P. Dendooven et al., Nucl. Instrum. Methods Phys. Res. A **408** (1998) 530

[Ell76] H.W. Ellis, R.Y. Pai, E.W. McDaniel, E.A. Mason, L.A. Viehland Atomic Data and Nuclear Data Tables **17** (1976) 177

[Ell78] H.W. Ellis, E.W. McDaniel, D.L. Albritton, L.A. Viehland, S.L. Lin, E.A. Mason, Atomic Data and Nuclear Data Tables **17** (1976) 177

[Fir96] R.B. Firestone and V.S. Shirley, Table of Isotopes, 8th ed., Wiley, New York, (1996)

[Fra87] B. Franzke, Nucl. Instr. and Meth. B **24/25** (1987) 18

[Fri02] T. Fritioff, H. Bluhme, R. Schuch, I Bergström and M. Björkage, Eur. Phys. J. A **15** (2002) 249

[Gra80] G. Gräff, H. Kalinowsky, and J. Traut, Z. Physik A, **297** (1980) 35

[Hab00] D. Habs et al., Hyp. Int. **129** (2000) 43

[Hak03] J. Hakala, Master thesis, (2003)

[Hau00] M. Hausmann et al., Nucl. Instr. and Meth. A **446** (2000) 569

[Her01] F. Herfurth et al. Nucl., Instr. and Meth. A **469** (2001) 254

[Her02] F. Herfurth et al., J. Phys. B (Submitted 2002)

[Ita95] W.M. Itano, J.C. Bergquist, J.J. Bollinger, D.J. Wineland, Phys. Scr. **T59** (1995) 106

[Jok91] A. Jokinen et al., Z. Phys. A **340** (1991) 21

[Jok96] A. Jokinen et al., Z. Phys. A **355** (1996) 227

[Jok97] A. Jokinen, P. Dendooven, J. Huikari, V.S. Kolhinen, A. Nieminen, K. Peräjärvi, K. Salomäki, J. Äystö, JYFL Annual Report (1997) 15

[Kel01] A. Kellerbauer, Private communication.

[Kel02] A. Kellerbauer, PhD. thesis, A Study of Accuracy of the Penning Trap Mass Spectrometer ISOLTRAP and Standard-Model Tests with Super Allowed Beta Decay. (2002)

[Klu93] S. Kluge et al., Jahresbericht, Kernchemie Mainz (1993) 37. Or from the internet http://csnwww.in2p3.fr/AMDC/web/experim.html

[Klö96] I. Klöck et al., JYFL Annual Report (1996) 30. Or from the internet http://csnwww.in2p3.fr/AMDC/web/experim.html

[Kob92] T. Kobayashi, Nucl. Phys. A **538** (1992) 343c

[Kol02] V.S. Kolhinen, T. Eronen, J. Hakala, A. Jokinen, S. Kopecky, S. Rinta-Antila, J. Szerypo, J. Äystö. 14th International Conference on Electromagnetic Isotope Separators and Techniques related to their Applications (EMIS-14), Victoria, B.C. Canada (2002), Nucl. Instr. and Meth. B **204** (2003) 502

[Kug00] E. Kugler, Hyp. Int. **129** (2000) 23

[Kön95] M. König, G. Bollen, H.-J. Kluge, T. Otto, J. Szerypo, International Journal of Mass Spectrometry and Ion Processes **142** (1995) 95

[Lép01] A. Lépine-Szily, Hyp. Int. **132** (2001) 35

[Lhe99] G. Lhersonneau, J.C. Wang, S. Hankonen, P. Dendooven, P. Jones, R. Julin, J. Äystö, Phys Rev. C **60** (1999) 014315

[Lit01] Y.A. Litvinov et al., Hyp. Int. **132** (2001) 283

[Lun98] D. Lunney et al., Proceedings of the International Conference on Exotic Nuclei and Atomic Masses ENAM98, Bellaire, MI, USA, 1998, edited by B.M. Sherril, D.J. Morrissey, C.N. Davids, AIP Conf. Proc. **455** (1998) 995

[Lun99] M.D. Lunney, R.B. Moore, Int. Jornal Mass Spectrom. **190/191** (1999) 153 **455** (1998) 995

[Mag99] Magnex Scientific Limited, System Manual for 7.0 Tesla 160 mm FTMS Ion Trap, (1999)

[Mar88] J.B. Marion, S.T. Thorton, Classical Dynamics of Particles & Systems Third Edition, Saunders College Publishing, Orlando (1988)

[McD73] E.W. McDaniel, E.W. Mason, The Mobility and Diffusion of Ions in Gases, Wiley, New York (1973)

[Moh91] F. M. Mohar et al., Phys. Rev. Lett. **66** (1991) 1571

[Moh99] P.J. Mohr and B.N. Taylor, J. Phys. Chem. Ref. Data **28** (1999) 1713

[Moo95] R.B. Moore, A.M. Ghalambor Dezfuli, P. Varfalvy, H. Zhao, Phys. Scr. **T59** (1995) 93

[Nie98] A. Nieminen, A. Jokinen, P. Dendooven, J. Huikari, V.S. Kolhinen, K. Peräjärvi, K. Salomäki, J. Äystö, JYFL Annual Report (1998) 16

[Nie01] A. Nieminen, J. Huikari, A. Jokinen, J. Äystö, P. Campbell, E.C.A. Cochrane, Nucl. Instrum. Methods Phys. Res. A **469** (2001) 244

[Nie02] A. Nieminen et al., Phys. Rev. Lett. **88** (2002) 094801-1

[Nie02b] A. Nieminen et al. 14th International Conference on Electromagnetic Isotope Separators and Techniques related to their Applications (EMIS-14), Victoria,B.C. Canada (2002), Nucl. Instr. and Meth. B **204** (2003) 563

[Oin01] M. Oinonen et al., Proposal to the ISOLDE and neutron time of flight committee, Nuclear binding around the rp-process waiting points ^{68}Se and ^{72}Kr, (2001)

[Pau53] W. Paul and H. Steinwedel, Z. Naturforschng. **8** A (1953) 448

[PPG] Becker&Hickl GmbH, Arbitrary Pulse Generator/PC Pattern Generator PPG-100 Operating Manual V1.2

[Rai97] H. Raimbault-Hartmann et al., Nucl. Instrum. Methods Phys. Res. B **126** (1997) 378

[H.Sav01] H. Savajols, Hyp. Int. **132** (2001) 245

[G.Sav91] G. Savard et al. Phys. Lett. A **158** (1991) 247

[Sch98] H. Schatz et. Al., Phys, Rep. **294** (1998) 167

[Tay94] B.N. Taylor, C.E. Kuyatt, NIST Technical Note 1297, 1994 edition, Guidlines for Evaluating and Expressing the Uncertainty of NIST measurement Results, United States Department of Commerce Technology Administration, National Institute of Standards and Technology

[WAGO] http://www.wago.com

[Wal81] R.K. Wallace, S.E. Woosley, Astrophys. J. Suppl. **45** (1981) 493

[Wor94] L. Van Wormer, J. Görres, C. Iliadis, M. Wieschier, F.-K. Thielemann, Astrophys. J. **432** (1994) 326